DOCTOR OF PHILOSOPHY

Finite-Size Scaling above the Upper Critical Dimension

Flores Sola, Emilio Jose

Award date:
2016

Awarding institution:
Coventry University

Coventry University
Université de Lorraine

Doctoral Thesis

Finite-Size Scaling above the Upper Critical Dimension

Author:
Emilio-José Flores-Sola

Supervisors:
Dr. Ralph Kenna
Dr. Bertrand Berche
Dr. Martin Weigel

A thesis submitted in fulfilment of the requirements for the degree of Doctor of Philosophy

in the

Statistical Physics Group
School of Computing, Electronics and Mathematics
Faculty of Engineering, Environment and Computing

October 3, 2016

Declaration of Authorship

I, Emilio-José Flores-Sola, declare that this thesis titled, 'Finite-Size Scaling above the Upper Critical Dimension' and the work presented in it are my own. I confirm that:

- This work was done wholly or mainly while in candidature for a research degree at this University.
- Where any part of this thesis has previously been submitted for a degree or any other qualification at this University or any other institution, this has been clearly stated.
- Where I have consulted the published work of others, this is always clearly attributed.
- Where I have quoted from the work of others, the source is always given. With the exception of such quotations, this thesis is entirely my own work.
- I have acknowledged all main sources of help.
- Where the thesis is based on work done by myself jointly with others, I have made clear exactly what was done by others and what I have contributed myself.

Signed: 

Date:

Resumé

Dans cette thèse on étudie les effets de taille finie au-dessus de la dimension critique supérieure d_c. Les effets de taille finie y ont longtemps été incomplètement compris, en particulier vis-à-vis de leur dépendance en fonction des conditions aux limites. La violation de la relation d'échelle dite d'hyperscaling a été l'un des aspects les plus évidents des difficultés rencontrées. Le désaccord avec le scaling usuel est dû au caractère de variable non pertinente dangereuse du terme de self-interaction dans la théorie en ϕ^4. Celle-ci était considérée comme dangereuse pour la densité d'énergie libre et les fonctions thermodynamiques associées, mais pas dans le secteur des corrélations. Récemment, un schéma nouveau de scaling a été proposé dans lequel la longueur de corrélation joue un rôle central et est également affectée par la variable non pertinente dangereuse. Ce nouveau schéma, appelé QFSS, est basé sur le fait que la longueur de corrélation exhibe au lieu du scaling usuel $\xi \sim L$ un comportement en puissance de la taille finie $\xi \sim L^{\wp}$. Ce pseudo-exposant critique $\wp$ est lié à la dimension critique supérieure et à la variable dangereuse. Au-dessous de d_c, cet exposant prend la valeur $\wp = 1$, mais au-dessus, il vaut $\wp = d/d_c$.

Le schéma QFSS est parvenu à réconcilier les exposants de champs moyen et le Finite-Size-Scaling tel que dérivé du Groupe de Renormalisation pour les modèles avec interactions à courte portée au-dessus de d_c en conditions aux limites périodiques. Si $\wp$ est un exposant universel, la validité de la théorie doit toutefois s'étendre également aux conditions de bords libres. Des tests initiaux dans de telles conditions ont mis en évidence de nouvelles difficultés : alors que le QFSS est valable au point pseudo-critique auquel les grandeurs thermodynamiques telles que la susceptibilité manifestent un pic à taille finie, au point critique on a pensé que c'était le FSS standard qui prévalait avec les exposants de champ moyen et $\xi \sim L$. On montre dans ce travail qu'il en va différemment de la situation au point critique et qu'à la place ce sont les exposants gaussiens qui s'appliquent en l'absence de variable non pertinente dangereuse. Pour mettre en évidence ce résultat, nous avons mené des simulations de modèles avec interactions à longue portée, qui peuvent être à volonté étudiés au-dessus de leur dimension critique supérieure. Nous avons aussi développé une étude des modes de Fourier qui permet de fournir des exemples de quantités non affectées par la présence de la variable non pertinente dangereuse.

Abstract

In this project finite-size size scaling above the upper critical dimension d_c is investigated. Finite-size scaling there has long been poorly understood, especially its dependency on boundary conditions. The violation of the hyperscaling relation above d_c has also been one of the most visible issues. The breakdown in standard scaling is due to the dangerous irrelevant variables presented in the self-interacting term in the ϕ^4 theory, which were considered dangerous to the free energy density and associated thermodynamic functions, but not to the correlation sector. Recently, a modified finite-size scaling scheme has been proposed, which considers that the correlation length actually plays a pivotal role and is affected by dangerous variables too. This new scheme, named QFSS, considers that the correlation length, instead of having standard scaling behaviour $\xi \sim L$, scales as $\xi \sim L^{\wp}$. This pseudocritical exponent is connected to the critical dimension and dangerous variables. Below d_c this exponent takes the value $\wp = 1$, but above the upper critical dimension it is $\wp = d/d_c$.

QFSS succeeded in reconciling the mean-field exponents and FSS derived from the renormalisation-group for the models with short-range interactions above d_c with periodic boundary conditions. If $\wp$ is an universal exponent, the validity of that theory should also hold for the free boundary conditions. Initial tests for such systems faced new problems. Whereas QFSS is valid at pseudocritical points where quantities such as the magnetic susceptibility experience a peak for finite systems, at critical points the standard FSS seemed to prevail, i.e., mean-field exponents with $\xi \sim L$. Here, we show that this last picture at critical point is not correct and instead the exponents that applied there actually arise from the Gaussian fixed-point FSS where the dangerous variables are suppressed. To achieve this aim, we study Ising models with long-range interaction, which can be tuned above d_c, with periodic and free boundary conditions. We also include a study of the Fourier modes which can be used as an example of scaling quantities without dangerous variables.

Acknowledgements

I would like to thanks all the people I met during all my PhD.

First of all, many thanks to my advisers Ralph Kenna, Bertrand Berche and Martin Weigel. I have really appreciated your patience with me, making this going easier, without your support this project would not have been possible. I thanks to Coventry University and Université de Lorraine together with its Doctoral college which funded this project. I am also glad to have met nice professors: Nikolaos Fytas, Thierry Platini, Malte Henkel, Nerses Ananikian and Christophe Chatelain.

I would also like to thanks to my PhD fellows from Coventry and Nancy, with whom I shared a lot of experiences, interesting talks and fun: Pádraig Mac Carron, Eren Metin Elçi, Kélig Aujogue, Lintao Zhang, Joseph Yose, Robin de Regt, Richard Looney, Lee Braiden, Ravinder Kumar, Anthony Rouquier, Dimitrios Voliotis, Sascha Wald, Marjana Krasnytska and Hugo Tschirhart.

I am wholly grateful to my parents Ana Sola and Francisco Flores, my siblings Nuria Flores, Fran Flores and Ana Flores who strongly supported me during these years. But I also say thanks their respective partners Fernan Maroto, Anabel Rodriguez and Erick Canales. Finally I want to thank my best friend and partner Silvia Casado, you made this worth-living.

Contents

Abbreviations

DIV	**D**angerous **I**rrelevant **V**ariable
FBCs	**F**ree **B**oundary **C**onditions
FK	**F**ortuin-**K**astelayn
FP	**F**ixed-**P**oint
FSS	**F**inite-**S**ize **S**caling
FT	**F**ukui-**T**odo
GFSS	**G**aussian **F**inite-**S**ize **S**caling
LRIM	**L**ong-**R**ange **I**sing **M**odel
MF	**M**ean-**F**ield
MFT	**M**ean-**F**ield **T**heory
PBCs	**P**eriodic **B**oundary **C**onditions
QFSS	**Q**-modified **F**inite-**S**ize **S**caling
RG	**R**enormalisation-**G**roup
SRIM	**S**hort-**R**ange **I**sing **M**odel
SW	**S**wendsen **W**ang

Dedicated to my family

Chapter 1

Introduction and outline

Phase transitions can be categorised in two types: first-order transition and continuous, depending on the behaviour of certain observables near to the transition point. At a first-order phase transition, quantities such as the internal energy, the first derivative of the free energy, experience a sudden change as a certain parameter (e.g., temperature) is tuned. This occurs, for example when a solid is heated up and melted to a liquid, or to a vapour as the system changes its internal structure at a molecular level. By contrast, at continuous transitions the internal energy is continuous across the transition. But its derivative, the specific heat, may experience a non-analyticity, such as a divergence, there. These are sometimes also referred to as first- and second-order phase transition, respectively.

The macroscopic critical behaviour of such many-body particles systems depends only on a limited number of properties. These include the dimensionality of the systems, any symmetries of its Hamiltonian and on the range of inter-molecular forces. Critical behaviour is independent of many other system properties including the geometry of the microscopic substrate (whether it is a square or triangular lattice) and the boundary conditions.

Systems which manifest such phase transitions contain huge (infinite) numbers of degrees of freedom, and have to be examined from the statistical physics point of view. Such complexity can be characterised through thermodynamic density functions. Within these types of transitions one finds that physical systems of a priori different natures can be described by the same scaling power-laws. In that case we say that they belong to the same universality class. For example although superfluity, superconductivity and ferromagnetism are very different physically, such systems can belong to the same universality class provided they have the same dimensionalities, symmetries and range of interactions.

After the invention of modern computers and their continuous development, computer simulations rapidly spread in science and technology as an alternative to experimental research as a means to verify (and falsify) theoretical work. Thanks to their great versatility, computer simulations have become an essential tool for research. Nowadays computational work is considered one of the pillars of research together with the experimental and theoretical work. Specially for condensed matter physics computer simulations are indispensable because of the enormous numbers of constituent particles comprising such systems. As a result, many new techniques have been developed and optimized. With such strong computational techniques, we can use stochastic techniques though Monte Carlo (MC) algorithms, which allow us to simulate many-body spin systems, and so reproduce its behaviour in order to study critical phenomena.

The motivation for this work is to achieve a better understanding of the critical phenomena that happens at phase transitions above the upper critical dimension where mean-field theories apply. Concretely we focus on ferromagnetic spin models which experience a continuous phase transition where quantities such as the correlation length diverge at the critical point. This project aims to investigate a new picture for the critical phenomena above the upper critical dimension, gathering together theory and simulation work. It is divided into chapters given by

the following structure.

In Chapter 2 we revisit the finite-size scaling (FSS) above the upper critical dimension d_c. There we shall show the breakdown of standard scaling behaviour is caused by dangerous irrelevant variables (DIVs) which arise from the self-interaction term in the ϕ^4 theory. In fact, in the regime above d_c, scaling should be compatible with predictions coming from mean-field theory (MFT). Standard renormalisation-group (RG) theory, which is strongly supported by many other studies and widely used successfully in many different models, is not directly able to achieve this without the introduction of DIVs. We will demonstrate that DIVs are essential to derive both the scaling laws for the infinite-volume system in the thermodynamic limit as well as the finite-size counterpart laws for systems of finite volume.

In Chapter 3 we introduce the numerical techniques used in this work and how they apply to Ising models with long-range interactions (LRIM). As an introduction to the MC simulations, we recall the Metropolis algorithm. This is followed with the implementation of different cluster algorithms, such as the multicluster Swendsen-Wang or the single-cluster variant named the Wolff algorithm, which is employed to simulated the 5D Ising model with nearest-neighbours interactions, named in this project as short-range Ising model (SRIM). Then, we proceed to describe a new variant of the algorithm suitable to simulate systems with long-range interactions. We also show how to implement the correct set up of periodic boundary condition (PBCs) for LRI models, through the Ewald sum method. Some aspects about the estimators, autocorrelation times, error treatment and reweighting method are shown too in this chapter.

In Chapter 4 we analyse FSS for the LRIM above d_c. We include the 5D SRIM which can be understood as a particular case of LRIM. Different boundaries conditions are analysed, namely periodic and free boundary conditions (written PBCs and FBCs, respectively). Quantities such as magnetisation, susceptibility and

correlation length, among others, are studied to determine their power-law scaling behaviours in finite systems. In order to understand deeply the consequences of DIVs we also focus on the study of the Fourier modes of the theory.

In Chapter 5 we study the zeros of the partition function. The zeros located in the complex plane for the external magnetic field are named Lee-Yang zeros, and the complex temperature plane are named Fisher zeros. The scaling of these zeros follow the corresponding FSS, above d_c these scaling are predicted to follow QFSS in line with chapter 4.

In Chapter 6, the project finishes with the study of LRIM at the critical dimension where multiplicative logarithmic corrections are expected to the leading power laws. There the logarithmic counterpart for the $\wp$ exponent claimed in chapter 4, appears as $\hat{\wp}$ leading the correlation length behaving as $\xi \sim L(\ln L)^{\hat{\wp}}$.

In Chapter 7, we discuss the conclusions.

Chapter 2

Revisiting the finite-size scaling above the upper critical dimension

2.1 Introduction

The renormalisation-group was invented over four decades ago [1, 2]. Since then, it stands as one of the pillars of modern physics. Given its fundamental importance, there should be no doubt about its correctness, completeness and validity. FSS is derived from RG considerations [3–5], despite in fact that it was heuristically introduced [6] before in terms of scaling hypothesis. Therefore, if the RG formalism is correct and fully understood, FSS should be too. However, for a long time, FSS had not been completely understood above the upper critical dimension d_c.

In particular, it had been supposed that some important features of MFT prevail above the upper critical dimension. However, these fail to deliver the correct scaling predictions. This results in a mismatch of the scaling predicted by MFT and the predictions by RG. The situation is especially puzzling in systems with open

boundary conditions. The breakdown of the mean-field scaling is connected to the violation of the hyperscaling relation, which in turn is attributed to the critical role of dangerous irrelevant variables in the renormalisation-group approach [7].

In an early attempt to repair FSS above d_c, Binder et *al.* introduced a new entity called the 'thermodynamic length' which scales as the system extent L above d_c and as the usual correlation length below d_c [8–10]. Although this new artefact worked, in the sense that it delivered the correct scaling behaviour for finite-size systems, it was phenomenological, rather than fundamental. Binder summarised the situation as "a rather disappointing state of affairs - although for the ϕ^4 theory in $d = 5$ dimensions all exponents are known, including those of the corrections to scaling, and in principle very complete analytical calculations are possible, the existing theories clearly are not so good".

Therefore a revisiting of the foundations of the theory was merited, in order to reconcile, not only in a phenomenological way, the FSS associated the RG with the MFT. This chapter follows the lines of the new theory and reports on the introduction of a new universal pseudocritical exponent $\varkappa$ ('koppa') which modifies the scaling of the correlation length as $\xi \sim L^{\varkappa}$. This new idea, proposed by Berche and Kenna [11], also modifies FSS to a new scheme called Q-finite-size scaling (QFSS). It plays an essential role in restoring the compatibility of the MFT and the RG.

The chapter is arranged as follows. In section 2, a brief introduction to second-order phase transitions is given. Section 3 recalls the scaling hypothesis and the main field theories. In section 4 a brief summary of the old scheme of FSS is given, together with a discussion of its strengths and weaknesses. The QFSS theory is introduced in section 5. To focus on the main, crucial points of the new scheme, we restrict our presentation to the ferromagnetic short-range interaction Ising models. The theory can easily be extended to other models. For example, to study critical

phenomena above the upper critical dimension in a physically realisable setting one can introduce the long-range interactions into the Ising model. These lead to a reduction in the critical dimensionality so that even 1D, 2D and 3D can fall above d_c. Such systems are experimental accessible, introducing a new level of importance to FSS theory in high dimensions. We present the full analysis of QFSS in Chapter 4.

2.2 Scaling at continuous phase transitions

Here we focus on ferromagnetic systems which manifest second-order or continuous phase transitions. The archetypal model for the study of such critical phenomena is the Ising model. Such phase transitions are characterized by a loss of spontaneous magnetisation at the critical point, while some other observables, such as magnetic susceptibility, heat capacity and correlation length, experience a divergence. This behaviour at the critical point occurs in the thermodynamic limit; in finite systems these singularities are modified to finite peaks, the positions of which are shifted away from the critical temperature.

2.2.1 Thermodynamic and correlation functions

In order to give a brief description in the simplest manner, we use a d-dimensional SRIM, concretely the nearest-neighbour Ising model as example. In this study we consider only simple structures for substrates on which the Ising spins reside. To this end, the spins s_i are located at the sites i, of a lattice so that every site is spaced a distance a from its $2d$ neighbours. That means a chain for 1D, a square lattice for 2D, a cubic lattice for 3D and hypercubic lattices for 4D and so on. The number of particles (Ising spins) is $N = L^d$ and the volume for such systems is $V = Na^d$. We henceforth set $a = 1$ to avoid having to track the constant when

it plays no role in our considerations. The partition function of a finite system is given by

$$Z_L = \sum_{\{s_i\}} e^{-\beta \mathcal{H}[s_i]}, \tag{2.1}$$

where the Hamiltonian is the total energy of a given configuration $\{s_i\}$ with $\beta = 1/k_B T$, where k_B is the Boltzmann constant. For the simplest Ising model,

$$\mathcal{H} = -J \sum_{\langle i,j \rangle} s_i s_j + \sum_i H_i s_i \tag{2.2}$$

where the sum $\langle i, j \rangle$ only extends to nearest neighbours, the coupling J is a constant (in other models it can depend on some special features and then it could be inside the sum), and H_i is the external magnetic field at site i. Then the Helmholtz free energy is related to the partition function through

$$F_L = -k_B T \ln Z_L. \tag{2.3}$$

The internal energy U_L is given by $U_L = F_L + TS_L$, where $S_L = -\partial F_L / \partial T$ is the entropy. Thus

$$U_L = F_L - T \frac{\partial F_L}{\partial T}. \tag{2.4}$$

In statistical mechanics the expectation value of the total energy is $\langle E \rangle = U_L$, so if the system does not have any external magnetic field $H_i = H = 0$,

$$\langle E \rangle = -\frac{\partial}{\partial \beta} \ln Z_L. \tag{2.5}$$

Intensive quantities are more useful to describe the thermodynamic systems, so one defines

$$f_L = \frac{F_L}{N}, \qquad \text{and} \qquad e_L = \frac{U_L}{N}, \tag{2.6}$$

respectively. Then we can derive the specific heat capacity from e_L:

$$c = \frac{\partial e_L}{\partial T} = \frac{k_B \beta^2}{N} \left(\langle E^2 \rangle - \langle E \rangle^2 \right) \tag{2.7}$$

This is a measure of the fluctuation in the configurational energy about the mean. Another important observable is the total magnetisation given by

$$M = \sum_i s_i. \tag{2.8}$$

The definitions for the magnetisation and the susceptibility are, respectively,

$$m_L = -\frac{\partial f_L}{\partial H} = \frac{\langle M \rangle}{N}, \tag{2.9}$$

$$\chi_L = \frac{\partial m_L}{\partial H} = \frac{\beta}{N} \left(\langle M^2 \rangle - \langle M \rangle^2 \right) \tag{2.10}$$

The correlation function $G(r)$ and the correlation length ξ_L are also crucial when describing critical phenomena. They are usually expressed in the thermodynamic limit, $L \to \infty$, as

$$G(r) \sim r^{-p} D \left[\frac{r}{\xi_\infty} \right] \tag{2.11}$$

Two regimes can be distinguished; when $r \gg \xi_\infty$ the function on the right-hand side takes the form $D\left[r/\xi_\infty\right] \sim \exp\left(-r/\xi_\infty\right)$. When $r \ll \xi_\infty$ the correlation decay becomes $G(r) \sim r^{-p}$ instead. In the spin model the correlation function is given in terms of connected and unconnected versions, and both definitions are respectively

$$G_c(r_i, r_j) = \langle s_i s_j \rangle - \langle s_i \rangle \langle s_j \rangle, \tag{2.12}$$

$$G(r_i, r_j) = \langle s_i s_j \rangle, \tag{2.13}$$

where r_i is the position of the ith spin s_i in the lattice site. The connected function can be obtained from the energy function as

$$G_c(r_i, r_j) = -\frac{1}{\beta N}\frac{\partial^2 f}{\partial H_j \partial H_i}. \tag{2.14}$$

2.2.2 Scaling and critical exponents

Physical systems which exhibit different phases of state have a transition between phases at the Curie or critical point. The critical point is not universal but scaling behaviour near to these transition points allows one to define the universality class that they belong to. In order to conveniently describe these features near to the critical point we define the reduced temperature as a dimensionless parameter which vanishes at the critical point. It is given by

$$t = \frac{T - T_c}{T_c}. \tag{2.15}$$

The other variable that controls the scaling of the observables at a phase transition is the reduced external magnetic field given by

$$h = \frac{H}{T}. \tag{2.16}$$

Near the transition point there is a set of observables, that yields crucial information about the system and the consequences of the phase transition. These include the internal energy; specific heat capacity; magnetisation with $h = 0$; magnetisation at the critical point, which depends on the external magnetic field, and the susceptibility. In an ideal case as the thermodynamic limit, when the size of the system is infinite (as indicated by the subscript), those observables behave in

terms of t and h

$$e_\infty(t,0) \sim |t|^{1-\alpha} \tag{2.17}$$

$$c_\infty(t,0) \sim |t|^{-\alpha} \tag{2.18}$$

$$m_\infty(t,0) \sim |t|^{\beta} \tag{2.19}$$

$$m_\infty(0,h) \sim |h|^{1/\delta} \tag{2.20}$$

$$\chi_\infty(t,0) \sim |t|^{-\gamma}. \tag{2.21}$$

These five quantities give us information about the energy and magnetic sectors and the parameters α, β, γ and δ are critical exponents. To probe the correlation sector too we introduce two more critical exponents:

$$\xi_\infty(t,0) \sim |t|^{-\nu}, \tag{2.22}$$

$$G_\infty(r) \sim r^{-(d-2+\eta)}. \tag{2.23}$$

2.2.3 Scaling relations

The six critical exponents defined here are related to each other in such a way that only two are independent. The scaling relations which link the critical exponents were discovered in the 1960s [7]. These famous expression are:

$$\nu d = 2 - \alpha, \tag{2.24}$$

$$2\beta + \gamma = 2 - \alpha, \tag{2.25}$$

$$\beta(\delta - 1) = \gamma, \tag{2.26}$$

$$\nu(2 - \eta) = \gamma. \tag{2.27}$$

The hyperscaling relation Eq.(2.24), developed by Widom, it is the only one that contains the dimension of the system. Originally proposed by Essam and Fisher,

Eq.(2.25) is also associated with Rushbrooke, who rigorously proved a related inequality. Eq.(2.26) put forward by Widom and proven by Griffiths, who gives it its name. The last relation, Eq.(2.27), was derived by Fisher through the dissipation and fluctuation theorem. Above the upper critical dimension, the Landau mean-field exponents obey all these relations apart from hyperscaling.

2.2.4 Fundamental theory of phase transitions

If one considers the complex variables for β and h, one finds for finite-size systems that the partition function vanishes at certain values. In the 1950's, Lee and Yang studied in detail the zeros for the Ising model in the complex-h plane. Published in [12, 13] under the inspiration of the fundamental theorem of algebra, it conformed a theory of complex zeros of the partition function may be called the *fundamental theory of phase transitions* [14]. They found that as the system approaches the thermodynamic limit, its zeros condense onto curves which may impinge onto the real axis. For $T > T_c$, the closest part respect to the real axis of these curves is denominated Lee-Yang edge h_{YL}. For second-order phase transitions it scales toward the critical point following this power law

$$h_{YL} \sim t^{\Delta}, \tag{2.28}$$

where Δ is the gap exponent. An analogous idea was then used by Fisher later on in [15] to perform the study for zeros in the complex-β plane, since then known as Fisher zeros. These zeros pinch the real axis at T_c in the thermodynamic limit.

2.2.5 Finite-size scaling hypothesis

The description above only applies for infinite volume systems. Finite volume systems cannot have phase transitions in the strict meaning of the term. The susceptibility that exhibits a divergence in the infinite-volume regime is transformed to a finite-sized peak. However, one can still study phase transitions by tracking and understanding such counterparts. The peak finite peak, for example, appears at a point which is shifted relative to the infinite-volume critical point. The position of this shifted peak point depends on the system size L and is called the pseudocritical point T_L. The FSS hypothesis resides in the relation between the scaling functions in the thermodynamic limit with their finite-size counterparts, where long-distance behaviour is controlled by the ratio of the two lengths of the system L and ξ_∞. Let $P(t,h)$ describe a generic observable scaling, setting $h=0$ for simplicity, the relation is given by

$$\frac{P_L(t_L)}{P_\infty(t)} = F_p\left[\frac{L}{\xi_\infty(t)}\right]\Bigg(\tag{2.29}$$

where $t_L = |T_L/T_c - 1|$ is the reduced pseudocritical temperature. In the thermodynamic limit its scaling is $P_\infty(t) \sim |t|^{-\rho}$. One fixes the scaling ratio $x = L/\xi_\infty(t)$. Then from Eq.(2.22) one finds that $|t| \sim x^{1/\nu}L^{-1/\nu}$. Introducing this relation into Eq.(2.29), thus

$$P_L(t_L) = P_\infty(x^{1/\nu}L^{-1/\nu})F_p(x) \sim L^{\rho/\nu}. \tag{2.30}$$

This scaling $P_L(t) \sim L^{\rho/\nu}$ actually not only describes the critical phenomena at the pseudocritical point, but also in a neighbourhood [16]. This region is called *scaling window* and it can also include the critical point, delivering then a similar scaling for both critical and pseudocritical points. In conclusion, inside the scaling window one is allowed to replace the ξ_∞ by system size L. Therefore the FSS of

the different observables are given by

$$c_L(t_L) \sim L^{\alpha/\nu}, \tag{2.31}$$

$$m_L(t_L) \sim L^{-\beta/\nu}, \tag{2.32}$$

$$\chi_L(t_L) \sim L^{\gamma/\nu}, \tag{2.33}$$

$$\xi_L(t_L) \sim L, \tag{2.34}$$

$$h_L^1(t_L) \sim L^{-\Delta/\nu}. \tag{2.35}$$

Where h_L^1 corresponds to the first Lee-Yang zero. As the system gets closer to the infinite volume, the t_L is driven to the critical point following a scaling power law which is characterised by the shift exponent λ

$$t_L \sim L^{-\lambda}. \tag{2.36}$$

The scaling window associated to P_L is described by a rounding exponent θ. The rounding may be defined in terms of the width between the half heights of the finite peak in the susceptibility,

$$\Delta T \sim L^{-\theta}. \tag{2.37}$$

These two exponents are predicted from standard FSS to take

$$\lambda = \frac{1}{\nu} \qquad \text{and} \qquad \theta = \frac{1}{\nu}, \tag{2.38}$$

which makes automatically $\lambda = \theta$. However, these relations are not always satisfied and may depend on boundary conditions. Specially above d_c, λ and θ do not manifest such standard form.

2.3 Widom's scaling and field theories

In order to describe critical phenomena for phase transitions, Widom, a pioneer of the scaling theories, proposed that the observables should be described by generalised homogeneous density functions. Another crucial step was the achievement of description of critical phenomena which produce critical exponents and their relations through simple theories, such as mean-field or Landau theory.

2.3.1 Widom's scaling ansatz

Widom's scaling ansatz was applied for the first time to the magnetisation [17],

$$m_\infty(t,h) = |t|^\beta \mathcal{M}_\pm \left(\frac{h}{|t|^\Delta}\right) \Bigg(\tag{2.39}$$

for the regime $t \to 0^\pm$ and $h \to 0$. If its argument is set to a constant and so $|t| \sim h^{1/\Delta}$, the magnetisation can be re-expressed as $m_\infty(t,h) \sim h^{\beta/\Delta} = h^{1/\delta}$ and so the gap exponent identified as $\Delta = \beta\delta$. Since the magnetisation must be derivable from the energy, Widom proposed that singular part of the free energy density is

$$f_\infty(t,h) = |t|^{2-\alpha} \mathcal{F}_\pm \left(\frac{h}{|t|^\Delta}\right) \Bigg(\tag{2.40}$$

with the assumption that free energy also scales as the inverse correlation volume

$$f_\infty(t,h) \sim \xi_\infty^{-d}. \tag{2.41}$$

To describe completely scaling behaviour of the system an analogous formalism is used for the correlation function

$$G_\infty(r,t,h) \sim \frac{1}{r^{d-2+\eta}} \mathcal{G}_\pm \left[\frac{r}{\xi}, \frac{h}{|t|^\Delta}\right] \Bigg(\tag{2.42}$$

With this set of thermodynamic functions, the scaling relations in the last section can easily be found [18]. The hyperscaling relation is obtained setting $h = 0$ in Eq.(2.40) and (2.41), and using $\xi_\infty \sim |t|^{-\nu}$, then $\nu d = 2 - \alpha$. The magnetisation is derived differentiating once Eq.(2.40) with respect to the h, comparing with Eq.(2.39), one gets $\Delta = \beta + \gamma$. The susceptibility, differentiating the energy twice. To derive the Fisher's relation one starts from the fluctuation-dissipation theorem

$$\chi_\infty(t) = \int_0^{\xi_\infty} d^d\mathbf{r}\; G_\infty(r, t, 0), \tag{2.43}$$

where the integral is bounded by the correlation length. Introducing firstly the correlation function by Eq.(2.42) and replacing secondly the argument by the ratio $x = r/\xi_\infty(t)$,

$$\chi_\infty(t) = \int_0^{\xi_\infty} dr\; r^{1-\eta}\mathcal{G}_\pm\left[\frac{r}{\xi}\right] = \xi_\infty^{2-\eta}\int_0^1 dx\; x^{1-\eta}\mathcal{G}_\pm[x]. \tag{2.44}$$

In this sense, as $\chi_\infty \sim \xi_\infty^{2-\eta}$, one only has to replace both observables by their scaling relation to identify $\gamma = \nu(2-\eta)$ [19].

2.3.2 Mean-field theory

As the name implies, in MFT an average field m_L replaces the various values of the magnetisation, making the model solvable as we shall now show. The Hamiltonian of the Ising model given by Eq.(2.2) is transformed by replacing $s_i \to m_L + \delta s_i$, where $m_L = \langle s_i \rangle$ and δs_i is the fluctuation term. The Hamiltonian is then

$$\mathcal{H} = J\sum_{\langle i,j\rangle}(m_L + \delta s_i)(m_L + \delta s_j) - H\sum_i s_i. \tag{2.45}$$

This Hamiltonian can be partitioned in two pieces, $\mathcal{H} = \mathcal{H}_{\rm MF} + \Delta\mathcal{H}$. The leading term up to first order corrections

$$\mathcal{H}_{\rm MF} = Jm_L^2 \sum_{\langle i,j\rangle} 1 - 2Jm_L \sum_{\langle i,j\rangle} s_i - H\sum_i s_i, \tag{2.46}$$

is kept and the second order term of fluctuations,

$$\Delta\mathcal{H} = -J\sum_{\langle i,j\rangle} \delta s_i \delta s_j, \tag{2.47}$$

is dropped. The number of interactions per particle in the nearest-neighbour version is given by the coordination number $q = 2d$. One can simplify $\mathcal{H}_{\rm MF}$ to

$$\mathcal{H}_{\rm MF} = \frac{q}{2} N J m_L^2 - (qJm_L + H)\sum_i s_i, \tag{2.48}$$

where we have used $\sum_{\langle i,j\rangle} 1 = qN/2$ and $\sum_{\langle i,j\rangle} s_i = (q/2)\sum_i s_i$. This mean-field Hamiltonian allows one to compute analytically the partition function since it looks like a single-body interaction, and one finds

$$Z_{\rm MF} = e^{-\frac{q}{2}\beta J m_L^2} \left(2\cosh[\beta H + q\beta J m_L]\right)^N. \tag{2.49}$$

Computing the energy from Eq.(2.3) one obtains

$$f_{\rm MF} = \frac{q}{2} J m_L^2 - k_B T \ln[2\cosh(\beta H + q\beta J m_L)], \tag{2.50}$$

and differentiating with respect to h, the widely known expression for the MF magnetisation is recovered,

$$m_L = \tanh[\beta H + q\beta J m_L]. \tag{2.51}$$

To check that this model has a phase transition, one only has to make a Taylor expansion of $\tanh^{-1}[m_L]$,

$$m_L + \frac{1}{3}m_L^3 + \ldots = \beta H + q\beta J m_L, \tag{2.52}$$

then set $H = 0$, and observe that the only solutions that are delivered, apart from $m_L = 0$, are

$$m_L = \pm\sqrt{3(q\beta J - 1)}. \tag{2.53}$$

There are only real solutions when $\beta \geq 1/Jq$. That means that MFT reproduces a phase transition for a non-zero temperature and the critical point is given by $\beta_c = 1/qJ$. So even when $H = 0$, the system presents a magnetisation for $T < T_c$ and zero-magnetisation for $T > T_c$.

The value of the critical exponents can be identified as follow: from the solution for the magnetisation in Eq.(2.53) one identifies $\beta = 1/2$; differentiating Eq.(2.52) with respect to H, one finds $\chi_L(1 - \beta/\beta_c) + m_L^2\chi_L + \ldots = \beta$ and consequently this leads to $\gamma = 1$; if one considers Eq.(2.52) at critical isotherm $\beta = \beta_c$, the magnetisation up $\mathcal{O}(m^3)$ takes the form $m_L^3 = 3\beta_c H$ and leading $\delta = 3$; finally differentiating twice Eq.(2.50) with respect to temperature leads to $\alpha = 0$.

Another way to approach the solution is just make an expansion of the energy, Eq.(2.50), so

$$f_{\mathrm{MF}} = -k_B T \ln 2 - Hm + \frac{k_B}{2}(T - T_c)m^2 + \frac{k_B T}{12}m^4 + \ldots. \tag{2.54}$$

When the m vanishes zero above the critical point, the energy of the systems is just $f_{\mathrm{MF}}(T > T_c) = -k_B T \ln 2$. Starting either from the energy or magnetic expansion, when deriving the other observables such heat capacity, susceptibility, etc., one finds same scaling expression and same mean-field exponent values.

2.3.2.1 Ginzburg criterion

In order to know how good was the mean-field approximation, one can analyse the term of the Hamiltonian that was neglected, $\Delta\mathcal{H}$ in Eq.(2.47). The fluctuation can be rewritten as $\delta s_i = s_i - m_L$, so the product of the fluctuations is just the correlation function, $\delta s_i \delta s_i = (s_i - m_L)(s_j - m_L) = G_L(r_i, r_j)$. One can use the fluctuation dissipation theorem Eq.(2.43) to compute the fluctuation term,

$$\Delta\mathcal{H} = -J \sum_{\langle i,j \rangle} G_L(r_i, r_j) = -\frac{qJ}{2\beta}\chi_L. \tag{2.55}$$

The Ginzburg criterion states that $\Delta\mathcal{H} \ll \mathcal{H}_{\text{MF}}$ so $\chi_L/\beta \ll L^d m_L^2$. In the thermodynamic limit where L is replaced by the ξ_∞, this is

$$\frac{\chi_\infty}{\beta} \ll \xi_\infty^d m_\infty^2. \tag{2.56}$$

This inequality brings another relation for the exponents, namely $\nu d > 2\beta + \gamma = 2 - \alpha$, which implies that the mean-field approximation is good enough everywhere above the upper critical dimension $d > d_c$, $d_c = 4$ for the Ising model.

2.3.3 Landau and Ginzburg-Landau-Wilson ϕ^4 theory

To construct a field theory to describe the phase transition and to be able to generate the symmetry breaking, Landau proposed to adapt Eq.(2.54). This is written in terms of the order parameter ϕ, responsible for generating the spontaneous symmetry breaking and it can be cut off to order ϕ^4 around the critical point. The energy expression now is replaced by a functional action, which has absorbed the β factor, so it is given by

$$f(t, h; \phi_0) = f_0(t, h) + \frac{r_0(t, h)}{2}\phi_0^2(t, h) + \frac{u(t, h)}{4}\phi_0^4(t, h) - h\phi_0(t, h). \tag{2.57}$$

The action is imposed to be invariant under a global symmetry-transformation of the order parameter $\phi_0 \to -\phi_0$. In order to minimize the action in terms of the order parameter one imposes

$$\frac{\delta f}{\delta \phi_0} = r_0(t,h)\phi_0(t,h) + u(t,h)\phi_0^3(t,h) - h = 0 \tag{2.58}$$

$$\frac{\delta^2 f}{\delta \phi_0^2} = r_0(t,h) + 3u(t,h)\phi_0^2(t,h) > 0. \tag{2.59}$$

Two main results can be found, firstly $\phi_0 = 0$ if $r_0 > 0$ and the secondly $\phi_0 = \pm\sqrt{-r_0(t)/u(t)}$ if $r_0 < 0$. The second result generates the symmetry breaking and so can be associated with the phase transition. Both solutions satisfy the minimum condition. For nonzero ϕ_0 solutions the terms r_0, which changes sign when crossing the critical point, and u can be expanded in a Taylor series in terms of t.

$$r_0(t) = r_{01}t + r_{02}t^2 + \ldots, \tag{2.60}$$

$$u(t) = u_0 + u_1 t + \ldots, \tag{2.61}$$

and so the first order expansion for the solution takes the form

$$\phi_0 = \pm\sqrt{\frac{r_{01}}{u_0}}|t|^{1/2} + \ldots. \tag{2.62}$$

One readily identifies the critical exponent $\beta = 1/2$. Using the thermodynamic relations one can easily find all the rest of the critical exponent which take the mean-field values.

A refined and general version of Landau theory, which also tracks the fluctuation of the fields is the Ginzburg-Landau-Wilson ϕ^4 theory. The Hamiltonian includes now a kinetic term and a general external magnetic field,

$$S[\phi] = \int d^d r \left(\frac{r_0}{2}\phi^2(\mathbf{r}) + \frac{1}{2}|\nabla\phi(\mathbf{r})|^2 + \frac{u}{4}\phi^4(\mathbf{r}) - h(\mathbf{r})\phi(\mathbf{r}) \right) \tag{2.63}$$

For the continuous systems the partition function is given by a path integral

$$Z[\mathcal{H}] = \int\!\!\!\int\!\!\!\int \mathcal{D}\phi \; e^{-S[\phi]}, \tag{2.64}$$

where $\mathcal{D}\phi$ denotes all possibles states. To handle the fluctuations we are interested explicitly in the external source $h(\mathbf{r})$. The free energy is given by $F[h] = -\ln Z[h]$ and so the magnetisation is nothing other than $m(\mathbf{r}) = \langle\phi(\mathbf{r})\rangle = -\delta F[h]/\delta h(\mathbf{r})$. Then the connected correlation function is given by

$$G(\mathbf{r},\mathbf{r}') = \frac{\delta^2 F[h]}{\delta h(\mathbf{r})\delta h(\mathbf{r}')} = \frac{\delta m(\mathbf{r})}{\delta h(\mathbf{r}')}. \tag{2.65}$$

On the other hand, if we consider the Gibbs free energy, given by the Legendre transform

$$\Gamma[m] = \int\!\!\!\int\!\!\!\int d^d r \; m(\mathbf{r})h(\mathbf{r}) + F[h], \tag{2.66}$$

one can find as $\delta\Gamma[m]/\delta m(\mathbf{r}) = h(\mathbf{r})$, so that

$$\frac{\delta^2\Gamma[h]}{\delta m(\mathbf{r})\delta m(\mathbf{r}')} = \frac{\delta h(\mathbf{r})}{\delta m(\mathbf{r}')} = G^{-1}(\mathbf{r},\mathbf{r}'). \tag{2.67}$$

Hence the fluctuation for $m(\mathbf{r})$ and $h(\mathbf{r})$ are reciprocally connected by the correlation function.

2.4 Dangerous irrelevant variables

We have seen that theories above the upper critical dimension give critical behaviour which is dimension independent. In fact, the discrete Hamiltonian for the d-dimensional SRIM in terms of spins s_i in Eq.(2.2) can be written as a field action via the Hubbard-Stratonovich transformation [7]. We consider, the action

$$S[\phi] = \int\!\!\!\int\!\!\!\int d^d x \left(f_0 + \frac{r_0}{2}\phi^2 + \frac{c}{2}|\nabla\phi|^2 + \frac{u}{4}\phi^4 - h\phi\right) \tag{2.68}$$

where the terms inside from left to right are the free energy f_0, the term related to the reduced temperature r_0, the kinetic term with coefficient c, the self interaction term in u, and the external magnetic field h.

In order to find the fixed-points and the FSS, Kadanoff implemented in the 1960's a methodology called "Block-Spin" that was the base for RG theory. This technique reduces the large number of degrees of freedom due the huge number of particles involved. To achieve such an aim, in consecutive steps, ones transforms a group of spins into an effective one, so one reduces the number of particles from N to N'. The idea is about of rescaling the Hamiltonian $\mathcal{H}_N(J,T) \to \mathcal{H'}_{N'}(J',T')$ and then following the fluxes of the variables to find the fixed points. The generalization of this method became Wilson's RG approach. The rescaling is given by a rescaling factor b that transforms L to L', where $L' = b^{-1}L$. One also rescales the Hamiltonian keeping the partition function fixed $Z'_L[\mathcal{H}'] = Z[\mathcal{H}]$. Hence the energy, for example, is found to scale as $f'_L[\mathcal{H}'] \to L^d f_L[\mathcal{H}]$.

One can obtain the scaling dimensions at the Gaussian fixed point derived by RG simply rescaling the Hamiltonian in Eq.(2.68) following from power counting. For example, we consider the rescaling for the term $d^d x'|\nabla'\phi'|^2 \to d^d x|\nabla\phi|^2$ with $x' = x/b$. This is visualised as

$$d^d x'|\nabla'\phi'|^2 = b^{-d+2} d^d x|\nabla\phi'|^2 = d^d x|\nabla\phi|^2, \tag{2.69}$$

finding that the order parameter scales as $\phi' = b^{d_\phi}\phi$ with $d_\phi = d/2 - 1$. Dimensional analysis for all the other terms delivers: for the free energy $f'_0 = b^d f_0$; the coefficient proportional the reduced temperature rescales following $r'_0 = b^{y_t} r_0$; the self interacting term follows $u' = b^{y_u} u$; and external source $h' = b^{y_h} h$. The eigenvalues are

$$y_t = 2, \qquad y_h = \frac{d+2}{2} \qquad y_u = 4 - d. \tag{2.70}$$

The ones that control the flow towards the fixed point are those $y_i > 0$. One clearly identifies $y_t > 0$ and $y_h > 0$ as relevant. The exponent y_u is irrelevant in the RG sense above the upper critical dimension $d = 4$. However, and as we shall see, it is also dangerous to set the associated variable u to zero. We first explore the case where u is zero.

2.4.1 Finite-size scaling for Gaussian model

Considering $y_u < 0$ as an irrelevant variable above the upper critical dimension for the fixed points, one may expect one can drop the ϕ^4 term in order to simplify the model. In this way the action Eq.(2.68) becomes the so-called Gaussian or free field theory model, given by

$$S[\phi] = \int\!\!\int\!\Bigg(d^d x \left(f_0 + \frac{r_0}{2}\phi^2 + \frac{c}{2}|\nabla\phi|^2 - h\phi \right) \Bigg(\tag{2.71}$$

which is governed by a Gaussian fixed point. Its homogeneous thermodynamic functions are found to be

$$f_L(t,h) = b^{-d} F_{L/b}(b^{y_t} t, b^{y_h} h), \tag{2.72}$$

$$\xi_L(t,h) = b\, \Xi_{L/b}(b^{y_t} t, b^{h} h), \tag{2.73}$$

$$g_L(t,h,\mathbf{x}) = b^{-d_\phi} \mathcal{G}_{L/b}(b^{-1}\mathbf{x}, b^{y_t} t, b^{y_h} h), \tag{2.74}$$

where they do not depend on u, and F, Ξ and $\mathcal{G}$ are universal functions. Using the thermodynamic relations for the magnetisation $m_L = -\partial f_L/\partial h$, for the heat capacity $c_L = \partial^2 f_L/\partial t^2$, etc., one obtains the critical exponents in terms of eigenvalues, these relations are given by

$$\alpha = \frac{2y_t - d}{y_t}, \qquad \beta = \frac{d - y_h}{y_t}, \qquad \delta = \frac{y_h}{d - y_h}, \tag{2.75}$$

$$\gamma = \frac{2y_h - d}{y_t}, \qquad \nu = \frac{1}{y_t}, \qquad \eta = d - 2y_h + 2. \tag{2.76}$$

At this point if one replaces the eigenvalues for those values found in Eq.(2.70), one obtains

$$\alpha^\dagger = 2 - \frac{d}{2}, \qquad \beta^\dagger = \frac{1}{4}(d-2), \qquad \gamma^\dagger = 1 \tag{2.77}$$

$$\delta^\dagger = \frac{d+2}{d-2}, \qquad \nu^\dagger = \frac{1}{2}, \quad \text{and} \qquad \eta^\dagger = 0, \tag{2.78}$$

where only $\gamma^\dagger = \gamma$, $\nu^\dagger = \nu$ and $\eta^\dagger = \eta$, i.e., coincide with the Landau or MF values. The rest do not match the MF values, and hence they do not describe correctly critical phenomena above d_c. For reasons discussed in Chapter 4, we have labelled them here with a † index to indicate that they come from the Gaussian model. That will allow us to distinguish them from the MF exponents. To complete the Gaussian model one can derive the scaling relations for magnetisation and susceptibility

$$m_L^\dagger(t,h) = b^{-d+y_h}\mathcal{M}_{L/b}^\dagger(b^{y_t}t, b^{y_h}h), \tag{2.79}$$

$$\chi_L^\dagger(t,h) = b^{-d+2y_h}\mathcal{X}_{L/b}^\dagger(b^{y_t}t, b^{y_h}h). \tag{2.80}$$

Setting $b = L$ and $h = 0$ the FSS functions for such observables are given by

$$m_L^\dagger(t) = L^{-d+y_h}\mathcal{M}_{L/b}^\dagger(b^{y_t}t) \sim L^{-(d-2)/2}, \tag{2.81}$$

$$\chi_L^\dagger(t) = L^{-d+y_h}\mathcal{X}_{L/b}^\dagger(b^{y_t}t) \sim L^2. \tag{2.82}$$

As expected these results are inappropriate above d_c, but in fact they will help us to understand the scaling picture for system with open boundaries, so for these reason we will call this scaling type as Gaussian finite-size scaling or GFSS, scaling derived from the Gaussian fixed-point exponents.

2.4.2 Finite-size scaling for ϕ^4 theory

As we have seen for the Gaussian model, in order to have a proper description of the phenomena u has to be taken into account even under its condition of irrelevant variable, that is why it is called dangerous irrelevant variable. Henceforth, one has to include the u dependence into the thermodynamic functions, so

$$f_L(t,h,u) = b^{-d} F_{L/b}(b^{y_t}t, b^{y_h}h, b^{y_u}u), \tag{2.83}$$

$$\xi_L(t,h,u) = b\, \Xi_{L/b}(b^{y_t}t, b^{y_h}h, b^{y_u}u), \tag{2.84}$$

$$g_L(t,h,u,\mathbf{x}) = b^{-d_\phi} \mathcal{G}_{L/b}(b^{-1}\mathbf{x}, b^{y_t}t, b^{y_h}h, b^{y_u}u). \tag{2.85}$$

These expressions for the regime below d_c present Wegner corrections due to the deviation of the fixed point, which is named Wilson-Fisher fixed point and the responsible of producing non-trivial critical behaviour [20]. To treat the DIV we follow the methodology suggest by Binder et *al*. [21], based on Fisher's formulation of DIVs. We assume $F_{L/b}(x_1,x_2,x_3) = x_3^{p_1} F_{L/b}(x_1 x_3^{p_2}, x_2 x_3^{p_3})$ considering small x_3. Applied to Eq.(2.83), it transforms as

$$f_L(t,h) = b^{-d^*} F_{L/b}(b^{y_t^*}t, b^{y_h^*}h), \tag{2.86}$$

where d^* is the effective dimension and y_i^*'s effective eigenvalues now related to the originals through

$$d^* = d - p_1 y_u, \tag{2.87}$$

$$y_t^* = y_t + p_2 y_u, \tag{2.88}$$

$$y_h^* = y_h + p_3 y_u. \tag{2.89}$$

We differentiate Eq.(2.86) to get the other thermodynamic functions, in order to obtain the critical exponents in terms of the effective ones. That delivers

$$\alpha = 2 - \frac{d^*}{y_t^*}, \qquad \beta = \frac{d^* - y_h^*}{y_t^*}, \tag{2.90}$$

$$\gamma = \frac{2y_h^* - d^*}{y_t^*}, \qquad \frac{1}{\delta} = \frac{d^*}{y_h^*} - 1. \tag{2.91}$$

To render these compatible with the MF values $\alpha = 0$, $\beta = 1/2$, $\gamma = 1$ and $\delta = 3$, we require that

$$y_t^* = \frac{d^*}{2} \qquad \text{and} \qquad y_h^* = \frac{3d^*}{4}. \tag{2.92}$$

The RG results for such systems delivers $d^* = d$ [21], three arguments are given in [21]. They have to be compared with the mean field exponent so $p_1 = 0$ $p_2 = -1/2$ and $p_3 = -1/4$. So the transform end up in the following relation [22–24]

$$y_t^* = y_t - \frac{y_u}{2} = \frac{d}{2}, \qquad y_h^* = y_h - \frac{y_u}{4} = \frac{3}{4}d. \tag{2.93}$$

A similar argument for the singular part of the correlation length gives

$$\xi_L(t,h) = b^{1+q_1 y_u}\Xi_{L/b}(b^{y_t+q_2 y_u}t, b^{y_h+q_3 y_u}h). \tag{2.94}$$

The correlation sector was thought to not be affected by DIVs, since ξ was thought to be always bounded by L and so one sets $q_1 = 0$ [25]. The arguments in Ξ should be coherent with those from the energy, then $q_2 = p_2$ and $q_3 = p_3$. After the transformation the thermodynamic functions are given by

$$f_L(t,h,) = b^{-d}F_{L/b}(b^{y_t^*}t, b^{y_h^*}h), \tag{2.95}$$

$$\xi_L(t,h) = b\ \Xi_{L/b}(b^{y_t^*}t, b^{y_h^*}h), \tag{2.96}$$

$$g_L(t,h,\mathbf{x}) = b^{-d_\phi}\mathcal{G}_{L/b}(b^{-1}\mathbf{x}, b^{y_t^*}t, b^{y_h^*}h). \tag{2.97}$$

We can now derive the thermodynamic functions for the magnetisation and susceptibility to see the effectiveness of this transformation,

$$m_L(t,h) = b^{-d+y_h^*}\mathcal{M}_{L/b}(b^{y_t^*}t, b^{y_h^*}h), \tag{2.98}$$

$$\chi_L(t,h) = b^{-d+2y_h^*}\mathcal{X}_{L/b}(b^{y_t^*}t, b^{y_h^*}h). \tag{2.99}$$

If one sets $b = L$ and $h = 0$

$$m_L(t) = L^{-d+y_h^*}\mathcal{M}_{L/b}(b^{y_t^*}t) \sim L^{-d/4}, \tag{2.100}$$

$$\chi_L(t) = L^{-d+y_h^*}\mathcal{X}_{L/b}(b^{y_t^*}t) \sim L^{d/2}. \tag{2.101}$$

These expression are the FSS predictions from RG theory. The shift exponent is also affected by DIVs, the pseudocritical point scales as $t_L \sim L^{-y_t^*} = L^{-d/2}$, leading a $\lambda = d/2$. This occurs since one expects a peak for the susceptibility corresponding to $\dfrac{\partial \chi_L}{\partial t}|_{t=t_L} = 0$, then $\mathcal{X}_{L/b}$ has to vanish there. The only possibility is that making its arguments to take constant value $b^{y_t^*}t_L = c$, then the relation for the shifting is straightforwardly extracted. The shift exponent then does not satisfy the standard prediction $\lambda = 1/\nu$.

Despite the fact that the transformation considered previously incorporated DIVs, the FSS derived from RG still suffers from inconsistencies and overall there is an important mismatch with the FSS hypothesis in the Landau or MF scheme as we shall see next.

2.4.2.1 Breakdown of renormalisation group and mean-field theory

The mismatch of the current picture both for RG as for the MFT is manifest in their FSS are not compatible each other, when in fact both scaling approaches

should describe the same critical phenomena. There are many studies that supported the RG predictions over those from MFT [24, 26]. However, one extraordinary result that could not be explained by the current picture of standard FSS or MFT was the scaling of the correlation length. Specially the widely studied 5D SRIM, was shown following a scaling $\xi_L \sim L^{5/4}$ [11]. Ising models with higher dimensionalities with PBCs also present such particular scaling anomaly with correlation lengths scaling in a power law higher than linear with the system size [5, 27–33]. In Ref. [11] was shown that this picture is also true for FBCs at pseudocritical point. Then both are part of an unsatisfactory theory. To illustrate this issue we derived the prediction for the scaling of the magnetisation and susceptibility as an example,

$$m_L(t) \sim |t|^{\beta}[L/\xi_L(t)]^{-\beta/\nu} \sim L^{-\beta/\nu} \sim L^{-1}, \tag{2.102}$$

$$\chi_L(t) \sim |t|^{-\gamma}[L/\xi_L(t)]^{\gamma/\nu} \sim L^{\gamma/\nu} \sim L^{2}. \tag{2.103}$$

As we pointed out before these expressions are incompatible with those from RG in Eq.(2.100) and (2.101). The shifts are also controversial, the FSS hypothesis allows us to replace ξ_L by L and in that sense one obtains $t_L \sim \xi_L^{-1/\nu} = L^{-1/\nu}$, leading $\lambda = 1/\nu$. A phenomenological solution was given by Binder to correct this mismatch with the introduction of the 'thermodynamic length' that is given in the last subsection.

2.4.2.2 Breakdown of hyperscaling

The hyperscaling relation became one of the main representative issues above d_c together with the mismatch of scaling predictions. To derive the hyperscaling relation one uses Eq.(2.41), and using Eq.(2.22) and then differentiate twice the

energy with respect to reduced temperature to get the heat capacity,

$$c_\infty = |t|^{d\nu-2}. \tag{2.104}$$

Considering then the scaling Eq.(2.18), immediately the hyperscaling relation, $\nu d = 2 - \alpha$, is obtained. This expression seems to hold systematically for every model below the critical dimension, and even at $d = d_c$, but above the upper critical dimension it breaks down. This is known as the violation of the hyperscaling relation. Mean field exponents seem to not satisfy this expression because of the dependence on d. In fact, one could guess that actually the expression should be $\nu d_c = 2 - \alpha$, but there was no a clean method to extract it, rather one could propose an inequality, $\nu d \geq 2 - \alpha$.

2.4.2.3 Fisher's scaling relation

The anomalies associated with the FSS do not only happen in the scaling of the observables or the violation of hyperscaling: Fisher's scaling relations also needs to be revisited. A negative value for the anomalous dimension for the 5D SRIM was reported by Baker and Golner [34] and also for the long-range models by Nagle and Bonner [35]. This conflicts with the prediction $\eta = 0$ from Landau theory. We consider, with external source $h = 0$, the fluctuation-dissipation theorem for finite-size system:

$$\chi_L(t) = \int_a^L dr\ r^{d-1} G_L(\mathbf{r}, t). \tag{2.105}$$

Here a is the lattice spacing. In principle, one can drop the lower limit of the integral assuming that the a-dependence only delivers corrections to the scaling. Introducing scaling relation for the correlation function from Eq.(2.42),

$$\chi_L(t) = \int_0^L dr\ r^{1-\eta} \mathcal{G}_\pm \left(\frac{r}{\xi_L}\right) \Bigg(\tag{2.106}$$

We can transform this integral by considering the ratio $x = r/\xi_L$, so that

$$\chi_L(t) = \xi_L^{2-\eta} \int_0^{L/\xi_L} dx\ x^{1-\eta} \mathcal{G}_{\pm}(x). \tag{2.107}$$

For $d < d_c$ one finds

$$\frac{\gamma}{\nu} = 2 - \eta, \tag{2.108}$$

which is the Fisher scaling relation. However for $d > d_c$, as $\chi_L \sim L^{d/2}$ and $\xi_L \sim L$, one finds instead

$$\eta = 2 - \frac{d}{2}. \tag{2.109}$$

Indeed this relation has not completely been understood. Luijten and Blöte in [36] called this $\tilde{\eta}$ to distinguish from η.

2.4.2.4 Thermodynamic length

In line with the belief that the correlation length is not affected by DIVs, Binder proposed the concept of *thermodynamic length* in [8, 9] to repair FSS above d_c. This new entity ℓ, whose name comes from the role it plays in thermodynamic functions, is supposed to scale as

$$\ell_\infty \sim |t|^{-1/y_t^*}. \tag{2.110}$$

Applying this new concept to repair the FSS for the observables above d_c

$$\frac{P_L(t)}{P_\infty(t)} = F_P\left(\frac{L}{\ell_\infty}\right) \tag{2.111}$$

For example the scaling for the magnetisation is clearly fixed

$$m_L = m_\infty(t) F_m\left(\frac{L}{\ell^{-2/d}}\right) = |t|^{\beta/\nu} F_m\left(\frac{L}{\ell^{-2/d}}\right) \sim L^{-d/4}. \tag{2.112}$$

However, and despite the fact that the thermodynamic length successes to reconcile the MF exponents with the RG, still just an phenomenological artefact, and it does not arise from microscopic considerations.

2.5 Q-finite-size scaling

Now that we have presented the main issues of the standard FSS, it is the right time to introduce modified or Q-finite-size scaling. DIVs seem to take a crucial part in the scaling above d_c, this allow us to consider to extend the usage of DIVs to the correlation sector, in contrast with the standard belief [37–40]. We may construct a natural description and development of QFSS if we suppose that the correlation sector also is affected by DIVs. Revisiting Eq.(2.94), we write

$$\xi_L(t,h) \quad = \quad b^{1+q_1 y_u}\Xi_{b/L}(b^{y_t+q_2 y_u}t, b^{y_h+q_3 y_u}h), \tag{2.113}$$

where these q_i are related with the p_i. Indeed $q_2 = p_2$ and $q_3 = p_3$, but concerning $p_1 = 0$, was also supposed $q_1 = 0$. Here, where the ansatz takes place, instead we suppose $q_1 \neq 0$. In fact, we supposed that $1 + q_1 y_u = d/d_c$, given a $q_1 = -1/4$. This new entity that will be denoted as,

$$\varkappa = \frac{d}{d_c}, \tag{2.114}$$

which is pronounced as 'koppa'. This is a new pseudocritical exponent, which governs the correlation length above the upper critical dimension. In this manner, we propose a new ansatz for the scaling of the correlation length,

$$\xi_L(t,h) \quad = \quad b^{\varkappa}\Xi_{b/L}(b^{y_t^*}t, b^{y_h^*}h). \tag{2.115}$$

The fact that we consider this exponent as a part of the correlation length will permit a reconciliation for the FSS hypothesis and from the FSS derived from RG, reuniting them with MF.

2.5.1 The pseudocritical exponent ϙ

All work described in this manuscript is based on the introduction of the DIVs in Eq.(2.113), a crucial point in the development of the QFSS theory. The peculiarity of this exponent ϙ, the reason because it is called pseudocritical, is that it is only manifested above d_c, in the MF regime. In fact

$$\text{ϙ} = \begin{cases} 1 & \text{if } d < d_c \\ \dfrac{d}{d_c} & \text{if } d \geq d_c. \end{cases} \tag{2.116}$$

A priori these two regimes of scaling can be seen as imposed, but in fact as a natural entity it also can be seen as the ratio between the thermal exponents,

$$\text{ϙ} = \frac{y_t^*}{y_t} = \frac{d}{d_c}. \tag{2.117}$$

Then when the system is below the d_c the DIV stops being dangerous, so $y_t^* \to y_t$ and it leads ϙ = 1. So one does not have to imposed anything further than the first consideration $\xi_L \sim L^{\text{ϙ}}$.

2.5.2 Mean field and hyperscaling reconciliation

The first results quickly start to show up. As $\xi_L \sim L^{\text{ϙ}}$, then $L \sim \xi^{1/\text{ϙ}}$, and consequently the singular part of the energy ($f_\infty \sim L^{-d}$ with $h = 0$) scales as the

inverse correlation critical volume

$$f_\infty(t) \sim \xi_\infty^{-d/\wp} = \xi_\infty^{-d_c}. \tag{2.118}$$

Differentiating the energy twice with respect to the temperature and using the relation $\xi_\infty \sim |t|^{-\nu}$, the heat capacity turns into $c_\infty \sim t^{d\nu/\wp - 2}$, immediately we get the QFSS hyperscaling relation

$$\frac{\nu d}{\wp} = 2 - \alpha, \tag{2.119}$$

that incorporates the $\wp$ exponent, and now it holds at any dimension above the upper critical dimension. Also as $\wp = d/d_c$ we have the alternative hyperscaling relation $\nu d_c = 2 - \alpha$ naturally. Furthermore the QFSS relations deliver a correct expression for the observables when considering $\xi_L(t) \sim L^\wp$. We show that the magnetisation and susceptibility now deliver RG scaling Eq.(2.100) and (2.101),

$$m_L(t) \sim |t|^\beta [L^\wp/\xi_L(t)]^{-\beta/\nu} \sim L^{-\wp\beta/\nu} \sim L^{-d/4}, \tag{2.120}$$

$$\chi_L(t) \sim |t|^{-\gamma} [L^\wp/\xi_L(t)]^{\gamma/\nu} \sim L^{\wp\gamma/\nu} \sim L^{d/2}. \tag{2.121}$$

Hence, in general the equation Eq.(2.30) is modified as follow

$$P_L(t_L) = P_\infty(x^{1/\nu} L^{-1/\nu}) F_p(x) \sim L^{-\wp\rho/\nu}. \tag{2.122}$$

with $x = L^\wp/\xi_L(t)$. The shift λ is also recovered from RG since $t \sim L^{-\lambda} = L^{-d/2}$, and $\lambda = \wp/\nu = d/2$.

2.5.3 A new Fisher scaling relation

Another piece of the puzzle that these new considerations can fix is the well known problem about the negative value of the anomalous dimension in 5D and the $\tilde{\eta}$

exponent ($\tilde{\eta} = 2-d/2 \neq \eta$). In order to clarify that issue, we revisit the fluctuation-dissipation theorem, above d_c but before we consider that the correlation length can also be written as

$$\xi_L^{d_c} = L^d. \tag{2.123}$$

Hence, following our earlier hypothesis, the correlation function should also be governed by DIV in the QFSS scheme. Under that consideration, it is given by

$$G_{\mathfrak{Q}}(0,r) \sim r^{-(d-2+\eta_{\mathfrak{Q}})} D_{\mathfrak{Q}}\left(\frac{r}{L}\right) \tag{2.124}$$

where $\eta_{\mathfrak{Q}}$ is a relative of $\mathfrak{Q}$. Then integrating over the space, the susceptibility is now given by

$$\chi_L(0) \sim \int_0^L r^{1-\eta_{\mathfrak{Q}}} D_{\mathfrak{Q}}\left(\frac{r}{L}\right) dr = L^{2-\eta_{\mathfrak{Q}}} \int_0^1 D_{\mathfrak{Q}}(y) y^{1-\eta_{\mathfrak{Q}}} dy \tag{2.125}$$

from new expression for the Fisher's relation can be extracted,

$$\eta_{\mathfrak{Q}} = 2 - \mathfrak{Q}\frac{\gamma}{\nu}. \tag{2.126}$$

This $\eta_{\mathfrak{Q}}$ is nothing other than $\tilde{\eta}$, since $\eta_{\mathfrak{Q}} = 2 - d/2$ for MF regime. In the QFSS picture it is extracted from a natural way. This anomalous dimension can also be related to η through

$$\eta_{\mathfrak{Q}} = 2 + \mathfrak{Q}(\eta - 2). \tag{2.127}$$

It automatically gives an explanation why the negative values for anomalous dimension appear above d_c shown in [34–36].

2.6 Conclusion

FSS, which was poorly understood above d_c for many years, can now be understood in a simple and natural way through QFSS. This picture relies on the fact that the correlation sector is also affected by DIVs, which give rise to the new exponent $\wp$ through the scaling for the correlation length $\xi_L \sim L^{\wp}$. This not only repairs the scaling behaviour for the others observables reconciling the RG and the MFT, but also it fixes the hyperscaling relation for any dimensionality above d_c in a modified relation $\nu d/\wp = 2 - \alpha$. It also resolved the nature of the $\tilde{\eta}$ and its negative values for 5D SRIM, giving to it a new Fisher relation $\eta_{\wp} = 2 - \wp\gamma/\nu$. These results were published in Ref.[11, 41–44] and form the background to this thesis.

Chapter 3

Numerical techniques for simulations

3.1 Introduction

The aim of this chapter is to give a description for the main numerical techniques that have been used for the research reported in this thesis. These numerical techniques not only include the algorithms that were used to simulate ferromagnetic systems, but also the Ewald summation method for slowly convergent sums that appear in the long-range interaction systems, the data processing together with the error analysis and the reweighting methods.

The main and most popular techniques widely used for classical particle systems are the Monte Carlo (MC) method and the molecular dynamics method, many other techniques are used for quantum systems, solids, etc. Each method has is own motivation and target. MC uses a stochastic approach, thus exploring all the configuration space of the systems. The molecular dynamics method is required to explore the time evolution of many-body systems. So these methods are complementary to each other. One wisely chooses the methodology more

suitable to study a specific system, some complex problems could even require both methods. In this thesis we focus on ferromagnetic systems above the upper critical dimension. The features of these systems depend on control parameters such as temperature, and one can measure their properties through observables such as the magnetisation. We are interested in generating different equilibrium configurations for these systems at specific temperatures to perform measurements of these observables through statistical averages. This is implemented by MC, which allows us to generate stochastic processes.

The ferromagnetic spin systems simulated in this project are the SRIM given by the Hamiltonian in Eq.(2.2) and the Ising model with long-range interactions given by

$$\mathcal{H} = -\sum_{i<j} J_{ij} s_i s_j + \sum_i H_i s_i, \quad \text{with} \quad J_{ij} = r_{ij}^{-(d+\sigma)}. \tag{3.1}$$

where r_{ij} is the distance between two spins. The details of this model will be discussed in chapter 4.

This chapter is structured as follows: in section 2 there is a summary of basic aspects of the MC method, and recent developments of cluster algorithms for long-range interacting systems; section 3 contains the explanation for how to set up properly the periodic boundary conditions for long-range systems; the methodology used for the data analysis is contained in section 4; finally in section 5 the discussion is reported.

3.2 Monte Carlo algorithms

In a many-body spin system, in terms of a continuum model with fields ϕ, the expectation value for an observable O is calculated through the path integral

$$\langle O \rangle = \frac{1}{Z} \int \mathcal{D}\phi \; O \; e^{-\beta \mathcal{H}[\phi]}, \tag{3.2}$$

where $\mathcal{D}\phi$ contains all the possible configurations and Z denotes the partition function. For discrete spin variables $\{s_i\}$, the last equation is replaced by

$$\langle O \rangle = \frac{1}{Z} \sum_{\{s\}} O(\{s\})\ e^{-\beta \mathcal{H}[s]}, \tag{3.3}$$

where now the sum runs over all the possible discrete states. Calculating Z exactly is usually not possible for many-body systems due to the difficulty of an exponentially growing number of states. Hence, the canonical probability of one state $\{s\}$, which is given by,

$$p_s = \frac{1}{Z} e^{-\beta E[s]}, \tag{3.4}$$

can not be calculated either. Thus, one aims to find a computational method that allows to sample the configuration space to perform correct average in a simple way. MC simulation is based on the Markov chains, a stochastic process which allows one to generate series of consecutive states in order to reproduce the behaviour of a many-body system [45]. The generation of a new state is randomly created only taking into account the previous state. One of the most widely MC simulation method specially for many-body spin system, but not only applicable in this field, is the algorithm developed by Metropolis et *al.* published in Ref. [46].

3.2.1 Estimators and autocorrelation times

As we are interested in the study of spin systems, the subsequent generated states, i.e., successive spin configurations are generated following the Boltzmann distribution. This conforms the importance sampling and it is fundamental in MC simulations, because it allows one to estimate the expectation value $\langle O \rangle$ in a simple way. This estimation is simply approximated given by the average over the Markov chain

$$\langle O \rangle \approx \bar{O} = \frac{1}{N} \sum_{n=1}^{N} O_n, \tag{3.5}$$

with N measurements. This expected value actually contains random statistical fluctuations around its theoretical value. The fluctuations decreases with increasing N. The associated variance is

$$\sigma_{\bar{O}}^2 = \langle \bar{O}^2 \rangle - \langle \bar{O} \rangle^2. \tag{3.6}$$

If one considers to measure the observables at every consecutive state, that probably leads an incorrectly estimation of the errors. This can be a consequence of the statistical dependence between two consecutive states and/or a lack of thermalisation. One needs then to take into account these details.

Thus, there are two main time scales associated with a MC simulation to examine, the thermalisation and the autocorrelation time. The first one refers to the numbers of MC sweeps that the system has to perform in order to reach equilibrium. That occurs when the energy oscillates around the expectation value following a Gaussian distribution. Once the system is thermalised one can safely proceed to sample and so the thermal average given by Eq.(3.5) will be a reliable approximation. Secondly, the autocorrelation time regards, once the systems is in a stationary state, how many sweeps one has to wait until a uncorrelated measurement can be sampled.

The definition of the correlation function, for a generic observable O sampled at the times $i < j$, is given by

$$A(i,j) = \langle O_i O_j \rangle - \langle O_i \rangle \langle O_j \rangle. \tag{3.7}$$

The sampling is considered to be performed in the equilibrium state. Hence, this implies that $\langle O_i \rangle = \langle O_j \rangle$ and moreover time translation invariance and so the correlation only depend on the 'distance' of two samples. The last expression can

then be normalised taking the form of

$$A(k) = \frac{\langle O_i O_{i+k}\rangle - \langle O_i\rangle^2}{\langle O_i^2\rangle - \langle O_i\rangle^2}, \tag{3.8}$$

where k is the separation between two measurements and $A(0) = 1$. The autocorrelation function is expected to decay exponentially as k grows. It approximately can be written as

$$A(k) \simeq A_0 e^{-k/\tau_{\text{exp}}} \qquad \text{with} \qquad \lim_{k\to\infty} A(k) = 0 \tag{3.9}$$

This decay is driven by the elapse of measurements or 'time' called *exponential* autocorrelation time τ_{exp}. Nevertheless, this picture is only true if $A(k)$ is purely exponential. Otherwise, the 'integrated' autocorrelation time τ_{int} is used [47] which is defined as

$$\tau_{\text{int}} = \frac{1}{2} + \sum_{k=1}^{N} A(k)\left(1 - \frac{k}{N}\right). \tag{3.10}$$

For enough measurements N, as $A(k)$ rapidly decays, it makes in the decaying regime $k \ll N$ and so the factor k/N can be neglected. Thus,

$$\tau_{\text{int}} \simeq \frac{1}{2} + \sum_{k=1}^{N} A(k). \tag{3.11}$$

Once τ_{int} is estimated, one should let the system update for $2\tau_{\text{int}}$, to make sure that two subsequent measurements will be approximately uncorrelated [47]. Sampling following this prescription one can easily estimate the number of effective samples N_{eff} given by a MC simulation with N sweeps, this is

$$N_{\text{eff}} = \frac{N}{2\tau_{\text{int}}} \leq N. \tag{3.12}$$

Therefore, the error associated with the statistical average in Eq.(3.5) depends on the number of effective samples,

$$\epsilon_{\bar{O}} = \sqrt{\sigma^2_{\bar{O}}} \sim \frac{1}{\sqrt{N_{\text{eff}}}}. \tag{3.13}$$

3.2.2 Metropolis algorithms

As an introduction to MC simulation we shall present the Metropolis algorithm. In order to illustrate the bases of the MC algorithms we start from Markov chains considerations. We restrict this presentation in many-body spin systems, but it can be extrapolated to a widely range of complex systems out of physics that presents critical phenomena. The phase space is the configuration space for spin systems $\{s_i\}$. The Markov chain is implemented considering that the system evolves from a state $\{s\}$ to successive state $\{s'\}$ through the transition operator $W(s'|s)$. In equilibrium the system must be time-invariant, so one demands that the probability between the transition of two states follows this relation

$$p_s W(s'|s) = p_{s'} W(s|s'). \tag{3.14}$$

This is known as detailed balance. The equilibrium probability distribution for the state s is given then by

$$p_{s'} = \sum_{\{s\}} p_s W(s'|s), \tag{3.15}$$

where $\sum_{\{s\}} W(s'|s) = 1$ must be satisfied. The transition matrix $W(s'|s)$ is determined by

$$W(s'|s) = R(s'|s)A(s'|s), \tag{3.16}$$

a composition between a proposal matrix $R(s'|s)$ which designates the next state with following a conditional probability, and an acceptance matrix $A(s'|s)$ which

decides if to accept the change. Here, we consider that successive states for our many-body spin system follow a random conditional probability and so $R(s'|s)$ is symmetric, and applying Eq.(3.14) one obtains that the acceptance ratio given by

$$\frac{A(s'|s)}{A(s|s')} = \frac{p_{s'}}{p_s} = e^{-\beta(E'-E)}. \tag{3.17}$$

Unfortunately this equation has multiple solutions. However, Metropolis et *al.* proposed the following solution

$$A(s'|s) = \begin{cases} e^{-\beta(E'-E)} & \text{if } E' > E, \\ 1 & \text{if } E' \leq E, \end{cases} \tag{3.18}$$

which can be summarised in a compact form

$$A(s'|s) = \min\left[e^{-\beta\Delta}, 1\right], \tag{3.19}$$

remind that $\Delta = E' - E$. The solution for such process conform the Metropolis algorithm and can be summarised as follows: accept the proposal to move from the state $s \to s'$ if the energy is minimised. Otherwise, accept with probability $A = e^{-\beta\Delta}$.

The validity of the Metropolis algorithm is proven, nevertheless it experiences a slowing down near to the critical point. The autocorrelation time can empirically be related to the correlation length [48] by

$$\tau \sim \xi^z, \tag{3.20}$$

where z is named dynamical exponent. Hence, and although the correlation length does not diverge for finite systems, it does experience a peak that can directly lead to a dramatical increment on τ. For the 2D SRIM or for the mean-field region this dynamical exponent takes $z \approx 2$, respectively in Ref. [4, 49].

3.2.3 Cluster algorithms

The motivation to find new algorithms to reduce the slowing down that the Metropolis suffers, lead to the implementation of a number of non-local new methods about thirty years later, by the late 80s. Then the first generation of cluster algorithms were developed based on the Fortuin-Kasteleyn representation, and this new method reduced drastically the slowing down by reducing the autocorrelation time, thus speeding up the collection of data near to transition points. In these cases the dynamical exponent was reduced from $z \approx 2$ to $z \approx 0.25$ for the 2D SRIM [50] and to $z = 0$ for the mean-field models [51, 52].

The multicluster algorithm was the first to come out, developed by Swendsen and Wang [53], based on the growing of several clusters in each MC sweep. Later on, a faster variant was proposed by Wolff [54], using a single-cluster algorithm version. Despite the fact that the slowing down near the transition point is dramatically reduced, the runtime of these algorithms still in order $\mathcal{O}(N_b)$. In the SRIM like the classic Ising model with nearest-neighbour interaction with N particles, this order of runtime is not very relevant, since $N_b = 2N$ the algorithm becomes $\mathcal{O}(N)$. However, for the long-range interaction models, the number of bonds is given by $N_b = N(N-1)/2$ instead. This makes such algorithms very costly, $\mathcal{O}(N^2)$ runtime, and consequently, computationally very expensive and quite inaccessible. Nevertheless, new branch of updates have been developed in the two last decades to overcome such runtime problems.

3.2.3.1 Swendsen-Wang algorithm

The multicluster algorithm, also called Swendsen-Wang (SW) algorithm, is based on the percolation bond representation for spin systems given by Fortuin and Kasteleyn [55, 56]. The Fortuin-Kasteleyn (FK) representation works on the direct product of spins $\{\sigma_\ell\}$ and graphs $\{g_\ell\}$ phase space, where l is the bond index,

instead of the conventional phase space of spins $\{s_i\}$ placed at site i. The discrete version of the partition function can be rewritten as

$$Z = \sum_{\{s_i\}} \prod_{i<j} e^{\beta J_{ij} s_i s_j} = \sum_{\{\sigma_\ell\}} \prod_{\ell=1}^{N_b} e^{\beta J_\ell \sigma_\ell}, \tag{3.21}$$

where $\sigma_\ell = s_i s_j$ and the coupling $J_\ell = J_{ij}$. Here, we have considered a general system where all bonds J_{ij} might be present, reflected in the $\prod_{i<j}$ term. The further considerations do not depend on the nature of the interaction and is easily adapted for systems with nearest-neighbour interactions. The partition function under the FK representation is given by the following transformation

$$\begin{aligned} Z &= \sum_{\{s_i\}} e^{\beta \sum_{i<j} J_{ij} s_i s_j} = \sum_{\{\sigma_i\}} \prod_{\ell} e^{\beta J_\ell} [(1-p_\ell) + p_\ell \delta_{\sigma_\ell,1}] && (3.22) \\ &= \sum_{\{\sigma_i\}} \sum_{g_\ell} \prod_{\ell} e^{\beta J_\ell} [(1-p_\ell)\delta_{g_\ell,0} + p_\ell \delta_{g_\ell,1}\delta_{\sigma_\ell,1}], && (3.23) \end{aligned}$$

where the terms have been written in terms of the probability to activate a bond $p_\ell = 1 - e^{-2\beta J_\ell}$ and the $\sum_{g_\ell}$ runs over all possible graph configurations. In a compact form, the partition function for FK representation can be written by

$$Z = \sum_{\{\sigma_\ell\}} \sum_{g_\ell} \omega(\sigma_\ell, g_\ell) \qquad \text{with} \qquad \omega(\sigma_\ell, g) = \prod_{\ell=1}^{N_b} \Delta(\sigma_\ell, g_\ell) V_\ell(g_\ell), \tag{3.24}$$

where two functions on the right side are

$$\Delta(\sigma_\ell, g_\ell) = \begin{cases} 0 & \text{if } \sigma_\ell = -1 \text{ and } g_\ell = 1, \\ 1 & \text{otherwise,} \end{cases} \quad \text{and} \quad V_\ell(g_\ell) = (e^{2\beta J_\ell} - 1)^{g_\ell}. \tag{3.25}$$

After a starting configuration of spins is set up, this algorithm works for one MC sweep following these steps:

1. Check all the bonds, one by one.

2. If $\sigma_\ell = 1$, activate the bond, i.e., $g_\ell = 1$ with probability $p_\ell = 1 - e^{-2\beta J_\ell}$.

3. Identify all clusters checking the activated bonds in step 2, but also considering single spin clusters.

4. Flip each cluster with probability 1/2.

The cluster flips considered in this algorithm allows to reduce the correlation between two consecutive sweeps. This is translated in a dramatical reduction of slowing down. Moreover, this algorithm also guarantees the detailed balance and ergodicity [53]. However, since we have to check all the bonds, this algorithm is still having a $\mathcal{O}(N_b)$ runtime. Furthermore, building the cluster hierarchy may cost another $\mathcal{O}(N_b)$ runtime process. For the SRIM models, that is actually not a problem, but for the LRIM it is.

As a complement for the MC algorithm, we discuss how the cluster identification in step 3 above is actually performed. The main algorithms to identify the cluster structure are given by breadth-first search (BFS) and depth-first search (DFS), as well as the commonly used Hoshen-Kopelman algorithm [57] which is, however, not explained here. BFS and DFS are similar methods. Let us say that we have for example a cluster graph as the one shown in Fig. 3.1. The BFS works as follows, starting from node 1, we follow all the possible diversions, prioritizing the lower labels, in each step and so on. That leads us to add the spins to the cluster in this order {1}, {26}, {3457}, {8} and the final hierarchy is also given in Fig. 3.1. The DFS works as follows, starting from one node it chooses one possible path in every diversion that it finds until a death path is found; then it steps back to last diversion and chooses another possible path that was not explored and so on until all elements of the cluster are visited. In this case presented in the last figure, it starts from the node 1 and follow the path 23654, once it returns to the last diversion, and continues the new path, in this case 78. The hierarchy is plotted in Fig. 3.1 too.

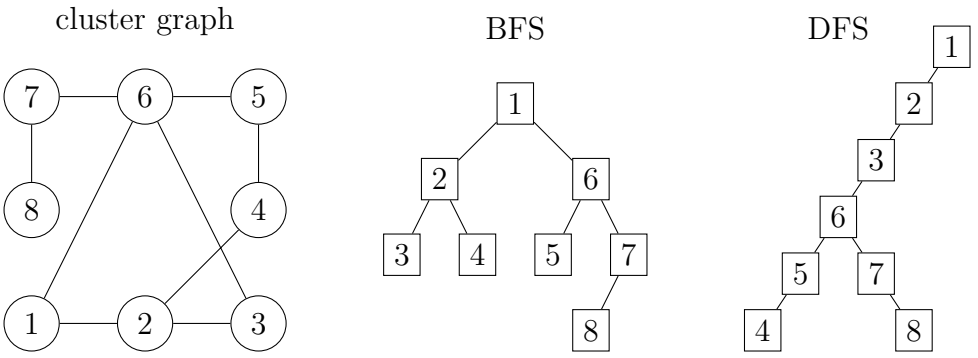

Figure 3.1: The left image shows an example of cluster graph. The middle image represents a tree structure of the last graph given by BFS, and the right image shows a tree constructed using DFS.

3.2.3.2 Wolff algorithm

For the single-cluster variant, or Wolff algorithm, one expects an improvement of runtime since longer cluster are flipped on average, but it still scales with $\mathcal{O}(N_b)$, so similar to the SW. The MC Wolff sweep is given by these steps:

1. Choose randomly one spin s_i.

2. Check all its interacting neighbours s_j's and with probability $p = 1 - e^{-2\beta J_{ij}}$ add them to the cluster stack if $s_i = s_j$.

3. If new spins were added to the stack, repeat step 2 with those spins. Continue this loop until all the spins in the stack check its neighbours.

4. Flip the cluster.

To make sure the first spin of the stack is not added again, at the moment that it is chosen, flip it and just save the last value to compare the rest of the elements of the lattice [58].

3.2.4 Algorithms for long-range interactions

As we have seen, the Wolff and the SW algorithm are problematic for the LRIM, since they perform sweeps in a very costly runtime of $\mathcal{O}(N^2)$ operations. The advantage of the cluster algorithms is given by the reduction of critical slowing down caused by the divergence of the correlation length. For these reasons an improved algorithms are needed in order to reduced their runtime.

The first efficient update, made for the Wolff version, came from Luijten and Blöte [59]. The full configuration update can be performed in $\mathcal{O}(N \log N)$. This tremendous speed-up is achieved because this algorithm, instead of checking all the $N-1$ neighbours of a given spin when growing the cluster, directly samples from the *cumulative* distribution of activating bonds. In this manner, it is decided at which distance the next spin will be successfully added. This fast Wolff version allows one to explore the nature of systems with long-range interactions. Some recent studies using this method are from Parisi et *al*. [60] and Picco [61].

The second update, that was the main algorithm used in this thesis, is the multicluster update recently published by Fukui and Todo [62]. This new update is also based on the FK representation and achieves a $\mathcal{O}(N)$ runtime per MC sweep, improving the speed-up of the Wolff version. To conclude with the MC algorithms we shall also present, a single cluster variant of this last algorithm.

3.2.4.1 Luijten-Blöte update: $\mathcal{O}(N \log N)$

Luijten and Blöte, in 1995, published a very fast method based on the Wolff algorithm but using cumulative distribution. The main idea is to compute a *cumulative bond probability* to estimate which neighbours will be chosen as candidates to be added to the single cluster. In that manner, once the spin s_i is randomly chosen we can calculate who will be the next candidate s_j, jumping $j-i$ spins. We consider

the simplest case of a one-dimensional (1D) model with PBCs to simplify the idea of the algorithm. The probability to be added to the cluster for two particles, with same spin value, is then given by

$$p_i = 1 - e^{-2\beta J_{r_i}}, \tag{3.26}$$

here r_i denotes the distance between both spins and the coupling is consider to take the form of a power-law decay $J_i = r_i^{-(d+\sigma)}$. The probability to chose the first spin in the nth position after jumping $n-1$ spins is

$$P(n) = p_n \prod_{m=1}^{n-1} (1 - p_m). \tag{3.27}$$

The *cumulative bond probability* is then just

$$C(j) = \sum_{n=1}^{j} P(n). \tag{3.28}$$

In order to choose how many spins will be jumped, a uniform random number $x \in [0, 1)$ is thrown. So if $C(j-1) \leq x < C(j)$, then $j-1$ spins will be jumped. For the distance of the successive candidates k, the probability of jumping other $k-j-2$ spins is,

$$P_j(k) = p_k \prod_{m=j+1}^{k-1} (1 - p_m). \tag{3.29}$$

The *cumulative bond probability* is then given by

$$C_j(k) = \sum_{n=j+1}^{k} P_j(n). \tag{3.30}$$

For the 1D model, last expression can be computed, and takes a simple form of

$$C_j(k) = 1 - \exp\left[-2\beta \sum_{n=j+1}^{k} J_n\right] \tag{3.31}$$

For this simple case, even $C_j(k)$ functions for two different distance can be related to each other in terms of Eq.(3.28). Thus

$$C(k) = C(j) + [1 - C(j)]\, C_j(k). \tag{3.32}$$

In this way, to pick next candidate only a slightly modification in the random number has to be done. That is just shift the range of the random number x to $x' \in [C(j), 1)$, the transformation is given by $x' = C(j) + [1 - C(j)]x$. To use this method one has to create a lookup table containing all the possible *cumulative bond probabilities*. Since the $C(k)$ depend on β, it is required to set up a lookup table for each different temperature. The MC sweep for this algorithm follows these steps:

1. Chose randomly a spin.

2. Generate random number and choose a spin following the cumulative distribution, if it has the same spin orientation add it to the cluster. Compute then who will be the next to be checked. Continue until to the maximum distance allowed is achieved

3. Check next spin that was added to the cluster, repeat 2 until no more spins are added to the cluster and everyone is already checked.

2. Flip the cluster.

For models with $d > 1$ one can not longer apply the look up table method, but in Ref. [58] a simple solution was proposed. Despite the fact that we do not use such algorithm in this work and we shall not go further into details, we can illustrate the idea to compare with the method proposed later in this manuscript.

To overcome this problem, Luijten and Blöte proposed a continue *cumulative bond probabilities* replacing the complex sum for $d > 1$ in Eq.(3.31) by a d-dimensional

integral in order to be able to give a close expression for the sum. They replaced the coupling in Eq.(3.1) by an easily closed but similar decaying expression arguing that it should only affect the non-universal quantities such as the critical points, but should leave the critical exponents invariant. They then proposed an effective continuous coupling given by an integral, that for the 2D model takes the form

$$\hat{J}_{ij} = \int_{r_x-\frac{1}{2}}^{x+\frac{1}{2}} dx \int_{r_y-\frac{1}{2}}^{y+\frac{1}{2}} dy \; (x^2+y^2)^{-\frac{d+\sigma}{2}}, \tag{3.33}$$

where r_x and r_y are the distance between two particles in the axis x and y respectively. This construction does not affect the behaviour of the scaling and so the FSS derived from RG. This expression is easily generalizable to a d-dimensional model.

3.2.4.2 Fukui-Todo update: $\mathcal{O}(N)$

The simulations for the present project were implemented using on $\mathcal{O}(N)$ cluster MC method specially developed in Ref. [62] for spin systems with long-range interactions, we shall name it the Fukui-Todo (FT) update. Cluster identification is performed by a special variant of tree-based union/find $O(\log N)$ algorithm. This MC method chooses a concrete number of events to activate bonds according to a Poisson distribution. This FT update also requires a lookup table, but in his case it will be independent of β. In this manner only one lookup table is required in the beginning of the simulation. Such lookup table is created with the Walker's method of alias [63], that samples from a discrete distribution of probabilities is detailed in appendix A. The method is based on the FK representation, but replaces the binary bond variables, corresponding to active and deactivate states, by arbitrary positive integers according to a Poisson distribution. The argument

starts considering the Poisson distribution itself,

$$f(k,\lambda) = \frac{e^{-\lambda}\lambda^k}{k!}, \tag{3.34}$$

where k denotes an integer and λ, the mean. As the sum for all probabilities is one, and $f(0,\lambda) = e^{-\lambda}$, hence the sum for all positive k's is exactly

$$\sum_{k=1}^{\infty} f(k,\lambda) = 1 - e^{-\lambda}. \tag{3.35}$$

This expression can clearly be associated with the probability to add a bond, $p_\ell = 1 - e^{-2\beta J_\ell}$ given by the SW algorithm, so in this case one can set $\lambda = \lambda_\ell = 2\beta J_\ell$. The activation of the bonds is made, if $\sigma_\ell = 1$, throwing a random integer number for each bond from the Poisson distribution. This is an extended FK representation, where the binary graph space $\{g_\ell\}$ is transformed into a integer Poisson numbers space $\{k_\ell\}$. At this point, it seems that one does not have any gain, but actually the Poisson distribution have the following property: the product of different Poisson distributions with mean λ_i conform a new Poisson distribution with mean $\lambda = \sum_i \lambda_i$, i.e., given by the sum of the previous means. Hence, only one Poisson distribution is necessary to create statistically uncorrelated events instead of using each distribution separately. Thus, one can gather all the cumulative probabilities summing all λ_ℓ's in a single Poisson distribution with mean

$$\lambda_{\text{tot}} = \sum_\ell \lambda_\ell = 2\beta \sum_\ell J_\ell = 2\beta J_{\text{tot}}. \tag{3.36}$$

The essence of this extended FK representation is shown through the following, the probability to assign a k_ℓ to a each bond is given by

$$\prod_{\ell=1}^{N_b} f(k_\ell,\lambda_\ell) = \frac{e^{-\lambda_{\text{tot}}}}{k_1!k_2!\ldots k_{N_b}!} \prod_{\ell=1}^{N_b} \lambda_\ell^{k_\ell}. \tag{3.37}$$

This probability is transformed to be given by only one Poisson number $k_{\text{tot}} = \sum_\ell k_\ell$, introducing from Eq.(3.34) $f(k_{\text{tot}}, \lambda_{\text{tot}})$,

$$\prod_{\ell=1}^{N_b} f(k_\ell, \lambda_\ell) = f(k_{\text{tot}}, \lambda_{\text{tot}}) \frac{k_{\text{tot}}!}{k_1! k_2! \dots k_{N_b}!} \prod_{\ell=1}^{N_b} \left(\frac{\lambda_\ell}{\lambda_{\text{tot}}}\right)^{k_\ell}. \tag{3.38}$$

The k_ℓ events are distributed following a weighting given by the ratio $\lambda_\ell/\lambda_{\text{tot}} = J_\ell/J_{\text{tot}}$. This result, allow us to make a β independent lookup table using Walker's method of alias for the distribution J_ℓ/J_{tot} which can be constructed in $\mathcal{O}(N)$ runtime. For such FK representation the partition function is described in terms of σ_ℓ and k_ℓ as follow

$$Z = \sum_{\{\sigma_\ell\}} \sum_{k} \prod_{\ell=1}^{N_b} \Delta(\sigma_\ell, k_\ell) V_\ell(k_\ell) = \sum_{\{\sigma_\ell\}} \prod_{\ell=1}^{N_b} \sum_{k_\ell=0}^{\infty} \Delta(\sigma_\ell, k_\ell) V_\ell(k_\ell), \tag{3.39}$$

where

$$\Delta(\sigma_\ell, k_\ell) = \begin{cases} 0 & \text{if } \sigma_\ell = -1 \text{ and } k_\ell \geq 1, \\ 1 & \text{otherwise,} \end{cases} \quad \text{and} \quad V_\ell(k_\ell) = e^{-\beta J_\ell} \frac{(2\beta J_\ell)^{k_\ell}}{k_\ell!}. \tag{3.40}$$

A sweep of the FT algorithm can hence be summarised as follows:

1. A random non-negative integer k is generated by Poisson distribution with mean λ_{tot}.

2. Perform the following loop k times.

   (a) In general case:

      i. Choose a bond ℓ with probability proportional to J_ℓ/J_{tot} by using Walker's method of alias with an order of inputs $N_b \sim N^2$.

      ii. If that bond was not chosen yet and both spin are in the same direction, then activate bond ℓ. Otherwise do nothing.

   (b) If it is allowed to use symmetries, as translational invariance:

i. First choose a site i with uniform random number from the interval $[1, N]$, then choose another site j with probability $J_{ij}/\sum_{j'\neq i} J_{ij'}$. In that case it is even possible to reduce the Walker's method of alias approximately to N inputs that critically reduces the storage.

3. Flip each cluster with probability 1/2.

Both FT and Luijten-Böte algorithms do not provide any expression to compute the exact value of the energy per MC sweep in the same order of performance $\mathcal{O}(N)$. Nevertheless, this FT update can estimate the thermal average energy with no extra time after all MC sweeps. In the FK representation every activation of the bond is related to the energy. If one differentiate the partition function in order to have an energy-like expression,

$$\langle E\rangle_{\mathrm{MC}} = -\frac{\partial}{\partial\beta}\ln \sum_c\sum_k W(c,k) \tag{3.41}$$

$$= \frac{\sum_c\sum_k\sum_\ell (J_\ell - k_\ell/\beta)W(c,k)}{\sum_c\sum_k W(c,k)} \tag{3.42}$$

$$= J_{\mathrm{tot}} - \frac{1}{\beta}\langle K\rangle_{\mathrm{MC}}, \tag{3.43}$$

where $J_{\mathrm{tot}} = \sum_\ell J_\ell$ and $K = \sum_\ell k_\ell$. Furthermore, the heat capacity can also be computed without any extra effort. The relation with the energy is given by $c = -(\beta^2/N)\partial E/\partial\beta$. Hence, in terms of thermal averages the heat capacity is

$$\langle c\rangle_{\mathrm{MC}} = -\frac{\beta^2}{N}\left[\frac{1}{\beta^2}\langle K\rangle_{\mathrm{MC}} - \left\langle\left(J_{\mathrm{tot}} - \frac{1}{\beta}K\right)^2\right\rangle_{\mathrm{MC}} - \left\langle J_{\mathrm{tot}} - \frac{K}{\beta}\right\rangle_{\mathrm{MC}}\right] \tag{3.44}$$

$$= \frac{1}{N}\left(\langle K^2\rangle_{\mathrm{MC}} - \langle K\rangle^2_{\mathrm{MC}} - \langle K\rangle_{\mathrm{MC}}\right). \tag{3.45}$$

One can observe that in this FK representation the capacity is not just the variance of the energy, rather it comes up with an extra linear term $\langle K\rangle_{\mathrm{MC}}$.

To complete the algorithm will introduced an efficient tree-based union/find technique, which included the pass-compression, used for systems with long-range

interactions. This given by Newman and Ziff [64] and it has a performance of $\mathcal{O}(\log N)$. The idea to develop such technique resides in the manner that the spins and the clusters are labelled. Firstly one considers each spin as a single-cluster which is labelled by 1, the initial size of the cluster, so each spin is initially its own root. When a bond is activated, binding two spins, one searches the root of both spins following an ascending path towards the root. Then, following the inverse path one points each spin through such path to the root. One can face different situations for the bonds: if one finds that both spins, referred to the bond, have the same root one does nothing; otherwise, if the root sites are different one checks the cluster size stored in both the roots, and then one adds the smaller cluster to the larger one. In case that the sizes of corresponding clusters are the same, one can randomly attach one to the other. When attaching the cluster trees one updates the survivor cluster summing the both cluster sizes given by the roots.

3.2.4.3 Fukui-Todo single-cluster update: $\mathcal{O}(N)$

Here, we present what should be an even faster cluster algorithm, based on the same idea as the FT update and working in the same extended FK representation, but in this case applied for the single-cluster version. Two aspects are making this cluster update more suitable and faster for the LRIM with PBCs. Firstly, it is more efficient since the autocorrelation time is reduced, and consequently the slowing down. This will be discussed further in the data analysis section 3.4. Secondly, since it is a single cluster, a search algorithm for the identification of the cluster is unnecessary. In the scheme we construct this single-cluster version as follows. Instead of using a single Poisson distribution with mean λ_{tot}, we associate a Poisson distribution of events per spin with mean $\lambda_m = \lambda_{\text{tot}}/N = 2\beta J_{\text{tot}}/N = 2\beta J_m$ where λ_m and J_m correspond to the average. We start picking one random spin, and then applying the Wolff algorithm, in that sense we focus only in the construction of one of all possible clusters that could be generated during the FT sweep. This

actually delivers an underestimation of the associated events per spin, as it only takes into account the probability of adding bond from the spins inside to the cluster to those outside, and ignoring the probability to be added one of the inside by those from outside. To correct this problem we consider the graph in Fig. 3.2, where a simple cluster structure is given, divided into three clusters given by violet and blue colours. The probability that one activated bond is added to the cluster is $p_m = 1 - e^{-2\beta J_m}$, but this probability is from the spin that is already in the cluster toward the one that is outside. This is shown through the orange arrow from spin A to B or C. Hence, we also consider the probability from the spin outside to add a spin of the cluster shown with the orange arrows from B or C towards A. One then considers that probability for such technique has to be modified as $p_m = 1 - e^{-4\beta J_m}$, and then the Poisson distribution has to be generated with a mean

$$\lambda_m = 4\beta J_m \tag{3.46}$$

The red arrows in Fig. 3.2 that link the spin A and D show the similar situation but with spins that already belong to the cluster. The consideration of modifying the mean λ_m does not alter the situation here because repeating the events for the bonds already added is irrelevant for the extended FK representation.

The Wolff version as we mentioned has some advantages as the reduction of the autocorrelation time, but unfortunately, the lack of translational invariance with FBCs makes this algorithm inappropriate for such boundaries. The energy can not easily be computed as in the FT multicluster update due to the modification of the events per spin and consequently it needs further study. Its steps are summarised following:

1. Choose randomly one spin s_i.

2. Throw a k_i random integer numbers from a Poisson distribution with mean $\lambda_m = 4\beta J_{\text{tot}}/N$.

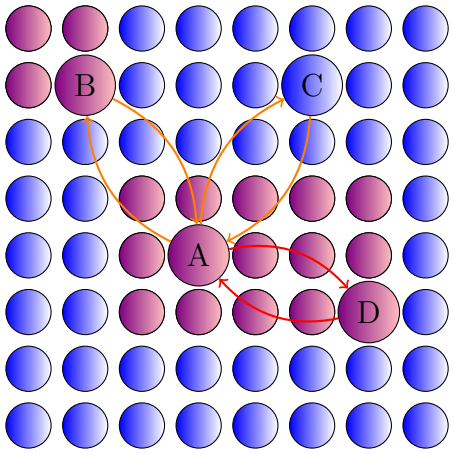

Figure 3.2: A simplified sketch of typical cluster distribution is shown. There are represented three cluster given by violet and blue colours, which represent the different spin orientation. The orange and red arrows represent the duplicity of the interaction between spins inside (A and D) or outside of the cluster (B and C) respectively.

3. Try k_i times to recruit elements for the cluster, and add them if they have same orientation.

4. Repeat step 3 with all the new members of the cluster until everyone is checked

5. Flip the cluster

3.2.5 Introducing an external magnetic field

In this subsection we present the generalisation of the cluster algorithm for systems in an external magnetic field, it can be found in Ref. [65]. In this project we only consider systems with constant external magnetic field. The inclusion of such field for the Metropolis update is straightforward, but in the long-range interactions scheme it is more difficult, specially in terms of runtime efficiency. Here we show how to perform the modification of the SW and Wolff algorithm within the FT update. One can naively think to modify the probability to activate a bond following $p_{ij} = (1 - e^{-2\beta J_{ij} + h s_i})$, but unfortunately this fails. For the cluster algorithms we can not just apply this probability of activation because then the

detailed balance will not be satisfied, that can be seen once the cluster is flipped and then the external field term is changed. Instead, the Hamiltonian is written as the sum of two parts as $\mathcal{H} = E + F$ where $E = -\sum_{i,j} J_{ij} s_i s_j$ and $F = h \sum_i s_i$, and the canonical probability for one state $\{s_i\}$ is written as

$$p_s = \frac{1}{Z} e^{-\beta(E+F)}, \tag{3.47}$$

Then, the acceptance ratio is constructed using the transition matrix $W(s'|s)$,

$$\frac{W(s'|s)}{W(s|s')} = \frac{p_s}{p_s} = e^{-\beta\Delta_E - \beta\Delta_F}. \tag{3.48}$$

Here $\Delta_E = E' - E$ and $\Delta_F = F' - F$. In that sense, $W(s'|s)$ can be factorised in the product of the corresponding internal energy, related to E, and energy given by the inclusion of the external magnetic field F,

$$W(s'|s) = W_E(s'|s) W_F(s'|s) \tag{3.49}$$

and then the acceptance ratio can be split in two process

$$\frac{A_E(s'|s)}{A_E(s|s')} = e^{-\beta\Delta_E} \qquad \text{and} \qquad \frac{A_F(s'|s)}{A_F(s|s')} = e^{-\beta\Delta_F}. \tag{3.50}$$

This gives us the advantage to split the MC sweep in two steps. This is that one can still using cluster algorithms, in terms of bond activation and cluster identification, for the internal energy E avoiding so the slowing down. However, the F term energy has to be implemented as Metropolis algorithm reducing the efficiency of the runtime. Despite the fact that detailed balance is satisfied, as one can not control the cluster size, one can not control the rejection ratio. That makes this algorithm very inefficient if one introduces a strong external magnetic field. The modified algorithm sweep follow the next steps

1. Follow the sweep steps for the SW or Wolff algorithm, updated with the FT variant if we are working with long-range systems, but stop before flipping the clusters.

2. Select each cluster according to the field energy with $p_F = e^{-\beta\Delta_F}$, where Δ_F correspond to the change of the energy for each cluster. Those selected are flipped with probability 1/2.

Regarding the step 2, the energy associated with the external field is very simple, one just has to multiply the magnetic field h by the size of the respective cluster.

3.3 Periodic boundaries for long-range interactions

Although setting up PBCs for SRIM can be done in a simple way, we can imagine a circle for 1D system or a a torus for a 2D model, for the LRIM this consideration is not enough to approach the thermodynamic limit. In such circumstances the FSS derived from that might not correspond to the ideal case. Indeed, for LRIM one demands that the interaction has to be extended to an infinite distance. The proper implementation for PBCs in systems with such long interactions is carried out with the introduction of extra lattices, called replicas. We shall show the difference between considering replicas or not for PBCs.

If one does not consider replicas, i.e., a naive approach of PBCs setup is straightforward. One simply uses the shortest possible distance within the lattice. For the 1D systems this result in

$$r_{ij} = \min(|i-j|, L-|i-j|). \tag{3.51}$$

For $d > 1$ it is easily generalizable. This set up is problematic since the long-range interactions are restricted by a finite system. Considering systems with extent L we only allow the interactions to go distances of up to $L/2$, so the interaction is strongly dependent on the system size. For slowly decaying interactions, corresponding to values of $\sigma < 2$, this consideration might lead to a model far away from the thermodynamic limit. In that sense, these considerations make this naive approach PBCs very close to the FBCs case. There, the interactions only go to a maximum distance of L. In Fig. 3.3 one can observe that the pseudocritical points occur far away from the critical point for the naive approach with PBCs as well as with FBCs. In the lower panel, we show that they follow same FSS at T_c. When one use replicas on the other hand, the system is driven near to the thermodynamic limit and experiences an expected FSS at T_c.

In Fig. 3.4 we show FSS at the critical point for susceptibility and magnetisation for some few system sizes. One sees that if one increases the number of replicas n, the system gradually crosses over from FBCs to the PBCs scaling. The number of replicas considered go from $n = 10^2$ to 10^{40}. We can observe that from 10^{20} replicas the QFSS is recovered. It might then give us an estimate the required system size that one should consider to have QFSS for FBCs at T_c, that is presumably unachievable to simulate nowadays.

Now we will show how to set up PBCs for systems with such interactions introducing an infinite number of replicas. This technique is based on computing an effective coupling that is extended to infinite range. When introducing the replicas, the raw interaction coupling J_{ij} in Eq.(3.1), is transformed to

$$\mathcal{J}_{ij} = \sum_{\mathbf{n}=-\infty}^{\infty}{}' |\mathbf{r}_i - \mathbf{r}_j + \mathbf{n}L|^{-(d+\sigma)}, \tag{3.52}$$

where $\mathbf{n}$ is the d-dimensional vector label for the $\mathbf{n}$th lattice replica considered. For $\sigma < d/2$ last expression for the effective coupling is a very slowly convergence

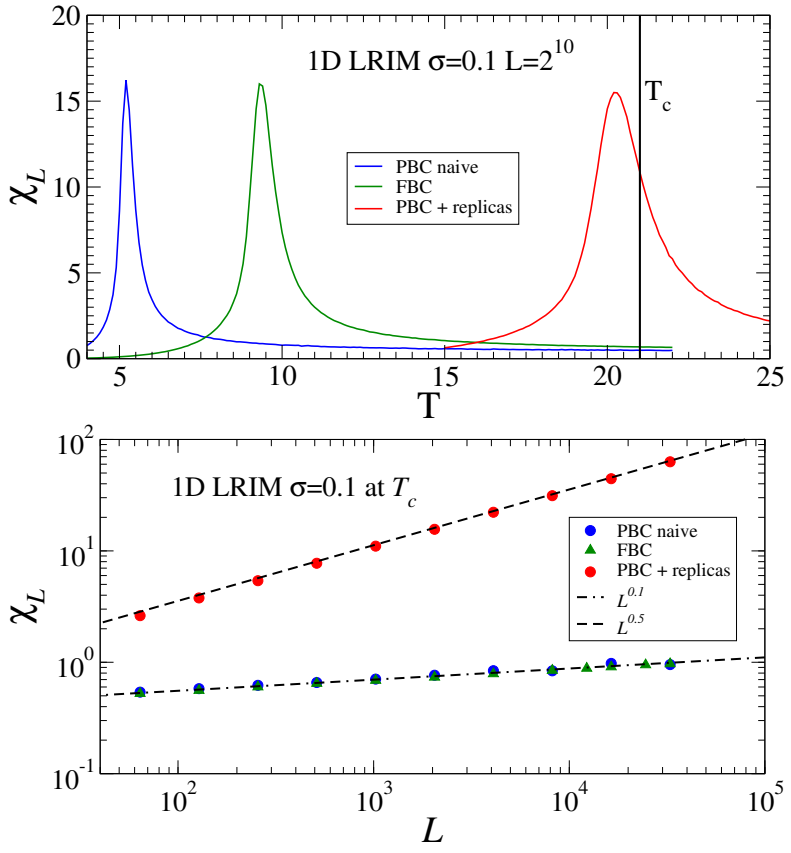

Figure 3.3: The top panel shows the susceptibility as a function of temperature, for a system with $L = 2^{10}$ spins with three types of boundary conditions. The bottom panel shows FSS of the susceptibility at T_c. The naive approach with PBCs gives a similar behaviour that FBCs. FSS for the system with PBCs with replicas, 'PBCs + replicas', follows the expected scaling above d_c which is $\chi_L \sim L^{d/2}$.

sum. Then, in general it can not be computed or properly approximated using a cut off.

The only case that the effective coupling $\mathcal{J}_{ij}$ can analytically be summed in an exact way is in 1D. This involves the Hurwitz zeta function [66]

$$\zeta(s,q) := \sum_{k=0}^{\infty} (q+k)^{-s}. \tag{3.53}$$

A closed expression for the 1D effective coupling is hence given by

$$\mathcal{J}_{ij} = \frac{1}{L^{1+\sigma}} \left(\zeta\left[1+\sigma, \frac{r_{ij}}{L}\right] + \zeta\left[1+\sigma, 1-\frac{r_{ij}}{L}\right] \right), \tag{3.54}$$

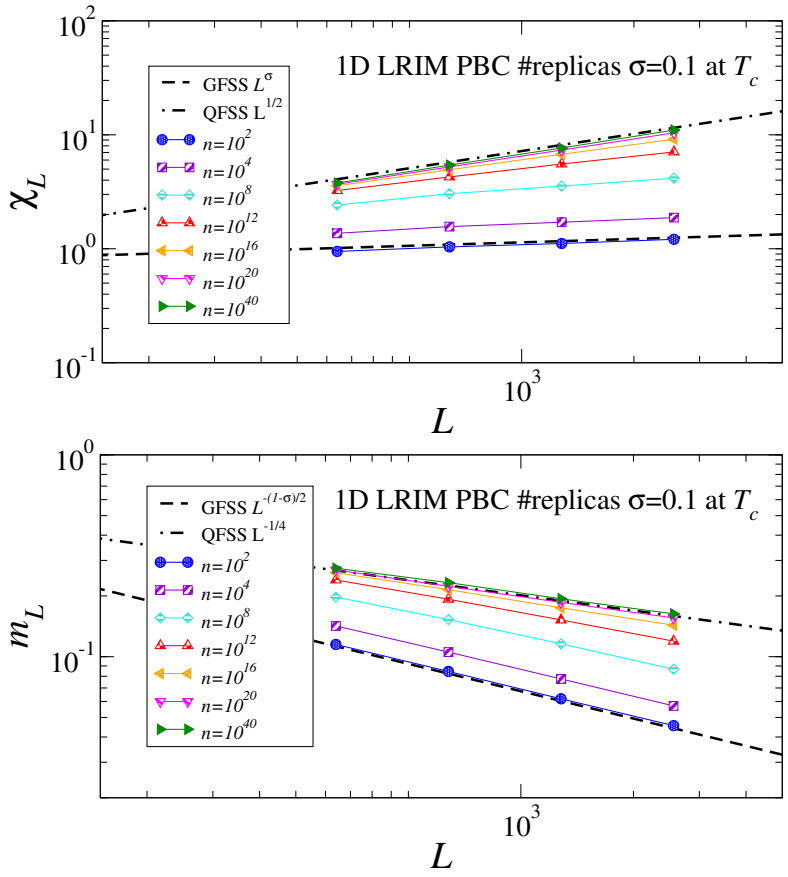

Figure 3.4: FSS of magnetization and susceptibility in terms of number of replicas. For low number of replicas a GFSS is obtained, but as the number of replicas increases QFSS is approached.

where we have been included the condition of minimal distance from Eq.(3.51). Unfortunately for $d > 1$ is not possible to achieve such a closed expression, and hence requires the introduction of a complex summation method with is discussed below.

In this project, as we are also interested in the d-dimensional systems with PBCs and their comparison with the corresponding FBCs systems, we use a summation technique in order to compute Eq.(3.52). The complete description of method, the Ewald summation, is given in appendix B. Applying the Ewald method the

effective coupling is transformed into a sum of three parts,

$$\mathcal{J}_{ij}(\mathbf{r},\mathbf{k}) = \frac{1}{\Gamma[\frac{d+\sigma}{2}]}\Bigg(\sum_n \frac{\Gamma\left[\frac{d+\sigma}{2}, \alpha^2|r+nL|^2\right]}{|r+nL|^{d+\sigma}} + \frac{\pi^{\frac{d}{2}}}{2^\sigma L^d}\sum_{k\in\mathcal{R}} e^{i\mathbf{k}\cdot\mathbf{r}} k^\sigma \Gamma\left[-\frac{\sigma}{2}, \frac{k^2}{4\alpha^2}\right] + \frac{2}{\sigma}\frac{\pi^{\frac{d}{2}}}{L^d}\alpha^\sigma\Bigg), \tag{3.55}$$

Where $\Gamma[a,b]$ is the incomplete gamma function. The first sum resides the real space, the second term lies on the reciprocal space. The sum is completed with a third independent term. Hence, the sum has been converted in a fast convergence sum. The Ewald method performs the transformation using an incomplete gamma function which when the sum is split in two parts, brings an auxiliary parameter α, which has to maximise $\mathcal{J}_{ij}(\mathbf{r},\mathbf{k})$. This α parameter takes different value for every different distance, so one must compute it for all possibles distances. Regarding the cutoffs that appear in the last equation, they are reduced to a couple of tens, and specially the sum in the reciprocal space can completely be neglected.

3.4 Data analysis

An accurate and reliable data analysis is essential to give strong support to our theories, so here we present the data analysis techniques carried out for this work. We describe the main issues about the data correlation and error estimation and the tools for a correct set up of the simulations and data collection. We follow, as a guide, the notes of Janke in [47] and then we will introduce the reweighting method developed by Ferrenberg and Swendsen [67].

3.4.1 Thermalisation and autocorrelation times

The thermalisation process of a given spin system depends on the starting spin configuration. In Fig. 3.5 we illustrate the thermalisation process for a 5D SRIM

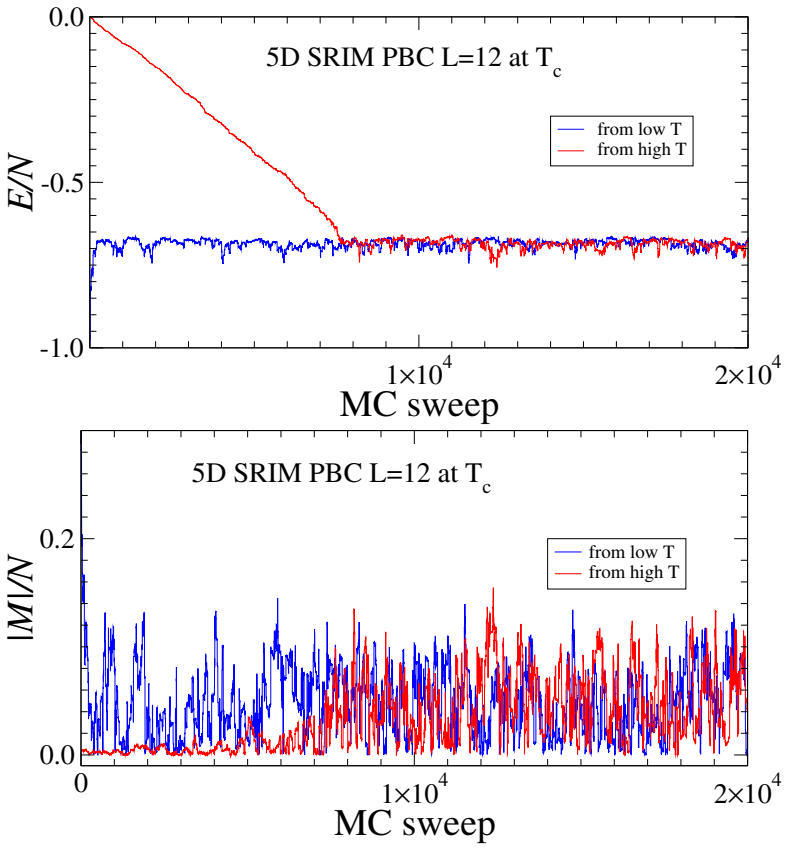

Figure 3.5: Thermalisation process of the 5D SRIM, simulated using the Wolff algorithm, is shown. The upper and lower images show the equilibration of the energy and magnetisation respectively. Both plots show the repercussion of choosing different starting spin configuration, where the blue and red lines refer to low and high temperatures respectively.

simulated using the Wolff algorithm. There, we plot the energy and the magnetisation in terms of MC sweeps. If the starting spin configuration has been chosen completely at random ± 1, the system will start from high temperatures, $T > T_c$. In such case, the quantity of sweeps needed to equilibrate the system is a bit less than the total number of spins. The thermalisation process can actually be sped up if one starts the system at low temperatures $T < T_c$, i.e., from a completely ordered spin configurations starting.

The LRIM presents bigger fluctuations than SRIM in the energy and also in the magnetisation. A very few sweeps seem to be needed to achieve a stationary state. In every MC sweep, due to the nature of the long range interaction each particle can access immediately each other member of the system, achieving thermalisation

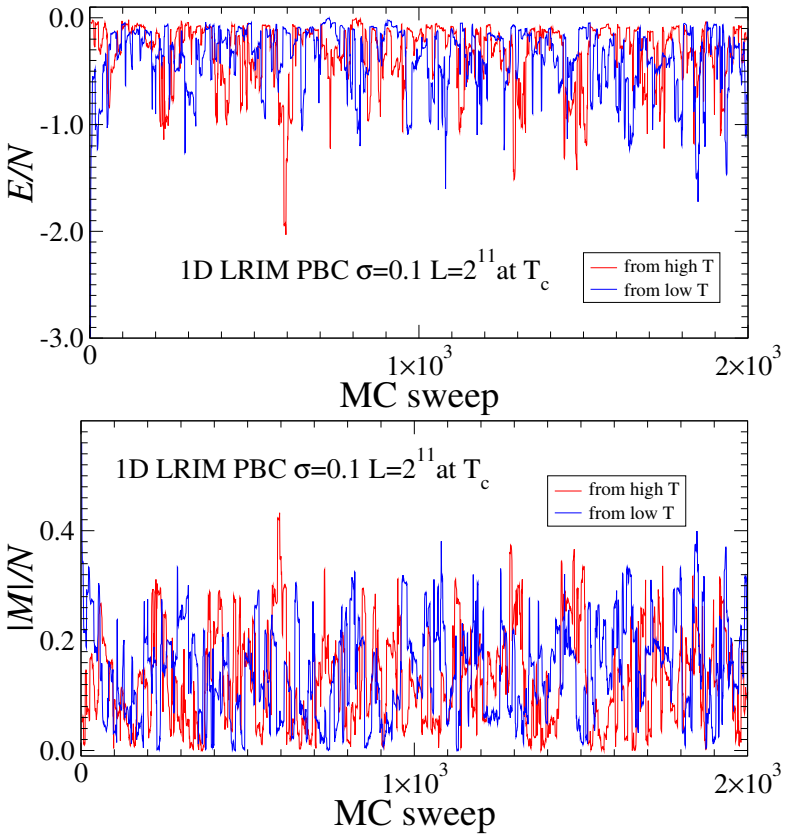

Figure 3.6: Thermalisation process of the 1D LRIM, simulated using the FT algorithm, is shown. The upper and lower images show the equilibration of the energy and magnetisation respectively. Both observables show that the equilibration time is barely perceptible. Indeed there it is, but the nature of the long-range interactions plus the cluster update method allow the system to experience a very fast equilibration. The blue and red lines refer to different starting spin configuration given by low and high temperatures respectively.

very quickly. It is visible from the plot in Fig. 3.6, it is indeed practically impossible to distinguish a distinct thermalisation phase.

Another important feature of simulations is the cluster dynamics since the dynamical exponent z drives τ through the correlation length. So, we have also investigated the FSS for τ_{int} for three kinds of cluster algorithm updates for 1D LRIM with PBCs for two values of $\sigma = 0.1, 0.2$ above d_c. These three updates are Luijten-Böte (LB), Fukui-Todo (FT) and FT single-cluster or Wolff version (FW). The dynamical exponents were analysed for the Potts model by Baillie and Coddington in [50]. Persky et *al.* in [52] looked to the complete graph model,

i.e., the MF region, and they found $z = 1$ for the SW algorithm and $z = 0$ for the Wolff algorithm. In this project we have analysed the τ for the LB, FT and FW algorithm at T_c. The results plotted in Fig. 3.7 show that $z \approx 0.2$ for the FT variant, and corresponding values are $z \approx 0$ for LB and FW variants. They seem to be independent of the strength of the interaction given by σ in the MF regime.

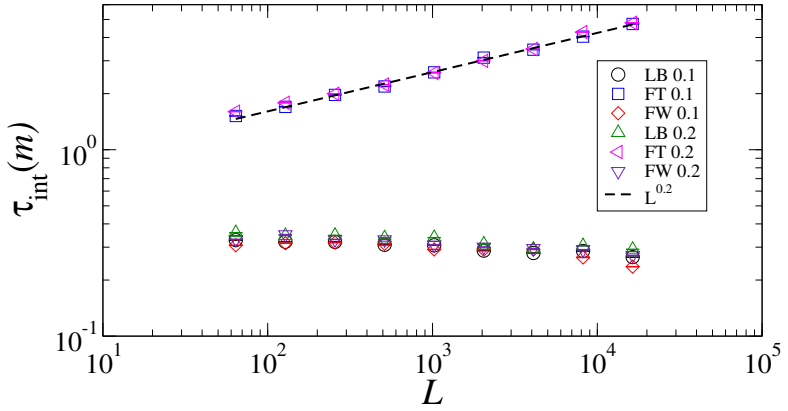

Figure 3.7: The scaling of the integrated autocorrelation time is plotted of the 1D LRIM with PBCs for two σ values, 0.1 and 0.2. For the three cluster updates: The Wolff versions have a dynamical exponent close to zero, however the SW Fukui-Todo shows $z \approx 0.2$.

Finally, in order to see the difference among the runtime given by different algorithm, we plot in Fig. 3.8 the performance of the Metropolis (MT), Wolff (WO), Luijten-Böte, Fukui-Todo and FT Wolff version for 1D LRIM with PBCs with $\sigma = 0.1$. One can observe the performance in terms of time per sweep and spin versus the system extent. We can observe the three regimes of runtime $\mathcal{O}(L^2)$, $\mathcal{O}(L \ln L)$ and $\mathcal{O}(L)$ respectively in MT, LB and FT. Specially we can notice the fast behaviour of the FW.

3.4.2 Error analysis

Despite the fact that sampling data is performed according to an accurate estimation of autocorrelation time, some minor correlations are always presented in the measurements. The binning analysis is simple but is not very accurate to estimate the errors, specially for such observables that are not a linear combination

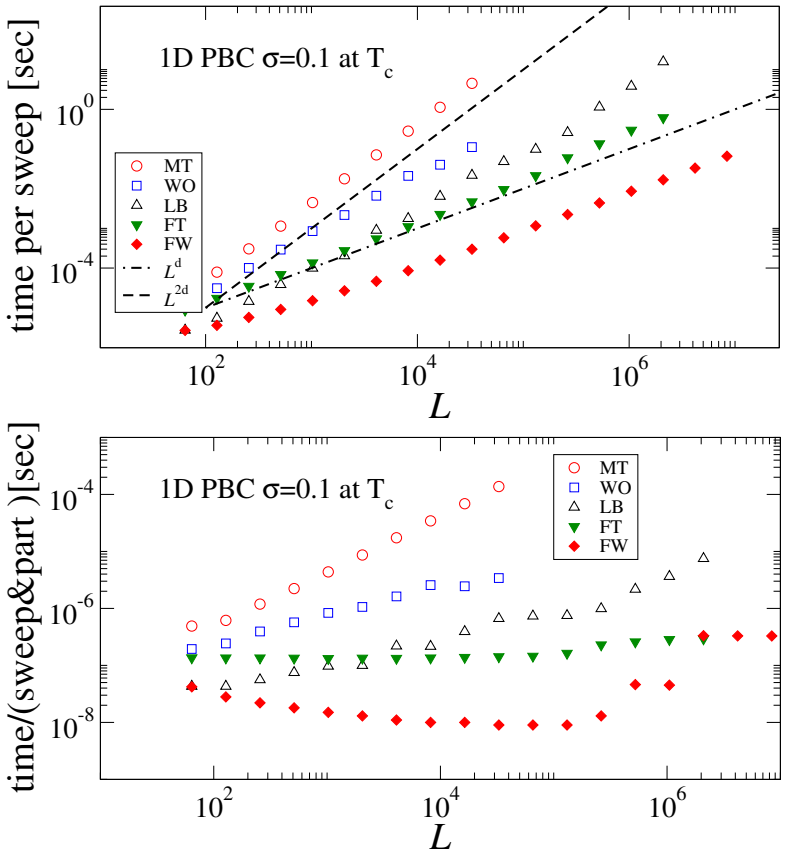

Figure 3.8: These two figures show the runtime for different algorithms. In the top image the time per sweep is plotted versus the system size, and in lower image contains the time per sweep and particle.

of directly measured quantities. Thus, the error analysis carried out in this work is based on the jackknife analysis, a refined method based on the binning analysis. The jackknife analysis is capable of taking into account the possible correlations that could remain between two samples.

3.4.2.1 Binning analysis

The binning analysis consists in dividing all the N measurements into small blocks N_B of length k. One makes the average according to

$$O_{B,n} = \frac{1}{k}\sum_{i=1}^{k} O_{(n-1)k+i}, \qquad \text{with} \qquad n = 1, \ldots, N_B. \tag{3.56}$$

To make sure the data within the blocks are uncorrelated one has to require $k \gg \tau$. The error for the binning analysis is given by

$$\epsilon_B^2 = \frac{1}{N_B(N_B-1)} \sum_{n=1}^{N_B} (O_{B,n} - \bar{O}_B)^2 \tag{3.57}$$

3.4.2.2 Jackknife analysis

The jackknife method uses the binning analysis, but considering a larger number of samples k for the blocks N_B. Those blocks are used to compute the jackknife blocks $O_{j,n}$ which contain $N-k$ measurements,

$$O_{j,n} = \frac{N\bar{O} - kO_{B,n}}{N-k}. \tag{3.58}$$

One considers larger N_b blocks to reduce the error in the binning blocks, this together with the jackknife blocks overestimates its error, and so it has to be corrected by $(N_B-1)^2$ factor. The error is finally given by

$$\epsilon_J^2 = \frac{N_B-1}{N_B} \sum_{n=1}^{N_B} \left(O_{J,n} - \bar{O}_j\right)^2. \tag{3.59}$$

3.4.3 Reweighting method

In order to save computational resources and time, the reweighting method is a very useful tool to reuse the amount of information saved inside the measurements in a MC simulation. This technique uses the properties of the canonical ensemble that allows us to extrapolate numerical results at a new temperature near to the previous temperature simulated. This method is specially useful to find the finite-size transition points.

In the canonical ensemble, the probability to stay in a certain state $\{s\}$ with energy E at β is given by $p_\beta \sim e^{-\beta E}$. Following that consideration, one can find that the

probability of a state at the same E at another inverse temperature β' is given by

$$p_{\beta'} = Ae^{-(\beta'-\beta)E}p_\beta, \tag{3.60}$$

where A is a constant given by both inverse temperatures. In that sense, we can compute the partition function as

$$Z_{\beta'} = \int ds\ p_{\beta'} = \int ds Ae^{-(\beta'-\beta)E}p_\beta = AZ_\beta\langle e^{-(\beta'-\beta)E}\rangle_\beta. \tag{3.61}$$

The value for the constant A is obtained as

$$A = \frac{Z_{\beta'}}{Z_\beta}\frac{1}{\langle e^{-(\beta'-\beta)E}\rangle_\beta}. \tag{3.62}$$

as a result, the expectation value for an observable at another temperature β' is given by,

$$\langle O\rangle_{\beta'} = \frac{1}{Z_{\beta'}}\int ds\ O(s)\ p_{\beta'} = \frac{\langle Oe^{-(\beta'-\beta)E}\rangle_\beta}{\langle e^{-(\beta'-\beta)E}\rangle_\beta}. \tag{3.63}$$

Despite the fact that the above equation considers any β' and that this expression go along all the configuration space, one can not apply such expression to MC simulations. This is because one can not generate all possible states in a reasonable computational time. For example for our case, there are 2^N possible states. Rather we use the MC measurement space

$$\langle O\rangle_{\beta'} = \frac{\sum_i O_i e^{-(\beta'-\beta)E_i}}{\sum_i e^{-(\beta'-\beta)E_i}}, \tag{3.64}$$

where i is the state sampled in the MC simulation. However, it has a limitation due to the computational method, and it is impossible to access all possible states, consequently it reduces the extrapolation function Eq.(3.64) to be only suitable in inverse temperatures β' close to β, where the spin configuration are similar.

To compute the associated error one can use the jackknife method, keeping in mind

that the error will increase as we move away from the computed temperature. One can use this method to find effectively the pseudocritical point recursively together with MC simulations. We can conclude that reweighting method is ideal and handy to save simulation effort, but weak comparing with proper simulated results.

3.4.3.1 Histogram reweighting method

To use a smaller storage requirement and to low the time spent in the reweighting method, one can use histograms based on energy levels instead. If this energy levels still requiring a considerable amount of storage, one can divide the energy in certain numbers of bins, despite the fact that it will deliver binning errors. In that case the formula follows

$$\langle O \rangle_{\beta'} = \frac{\sum_E O(E) h_{\beta'}(E) e^{-(\beta'-\beta)E}}{\sum_E h_{\beta'}(E) e^{-(\beta'-\beta)E}}, \tag{3.65}$$

where $h_{\beta'}(E)$ is the density of states for a given energy. One also is interested in including external magnetic field, then one rather has to consider magnetisation dependence for the density states $h_{\beta'}(E, M)$.

3.4.3.2 Reweighting method for Fukui-Todo update

For the FT update one is not possible to perform a direct measurement of the energy in a MC steps if we want to keep the computational effort per update of order $O(N)$. However, the energy is actually given in terms of bond activation g_ℓ and positive Poisson integers given by k_ℓ for the extended FK representation that is used by the FT algorithm. Then, we can luckily write down a reweighting equation specially for such technique. From its partition function, written in Eq.(3.39) and

(3.40), one extracts that the canonical probability is

$$p_\beta = \sum_k \prod_{\ell=1}^{N_b} \Delta(\sigma_\ell, k_\ell) V_\ell(k_\ell) = \sum_k \prod_{\ell=1}^{N_b} \Delta(\sigma_\ell, k_\ell) e^{-\beta J_\ell} \frac{(2\beta J_\ell)^{k_\ell}}{k_\ell!}. \tag{3.66}$$

Then, the probability of a state at another inverse temperature β' at the same energy, for such representation is simplified to

$$p_{\beta'} = A e^{-(\beta'-\beta)J_{\text{tot}}} \left(\frac{\beta'}{\beta}\right)^{k_\ell} p_\beta, \tag{3.67}$$

where now the term $e^{-(\beta'-\beta)J_{\text{tot}}}$ does not depend on the configuration and can be absorbed by the constant. Following the same argument as before we arrive at the reweighting formula

$$\langle O \rangle_{\beta'} = \frac{\sum_i O_i (\beta'/\beta)^{K_i}}{\sum_i (\beta'/\beta)^{K_i}}, \tag{3.68}$$

where $K_i = \sum_\ell k_\ell^i$, i.e., sum for all active bonds for a given MC sweep and i refers to such a sweep. If we want to extrapolate the energy we only have to set $O_i = K_i$, and then to apply the formula $E = J_{\text{tot}} - \langle K \rangle / \beta'$ given in Eq.(3.41). In Fig. 3.9 we can observe how is the performance of this reweighting method compared with the standard one. We can notice that because of similarity of the spin configuration for high energies the energies fit further for high energies.

3.5 Conclusion

In this chapter we have shown the methods and techniques that were applied in order to produce reliable data through the simulations that this work contains. We have also given the details of a very important update for the cluster algorithm for systems with long-range interactions showing that the speed of computation can be lowered even more from the algorithm developed by Luijten $O(N \ln N)$ to $O(N)$ thanks to the update proposed by Fukui and Todo. Furthermore we have

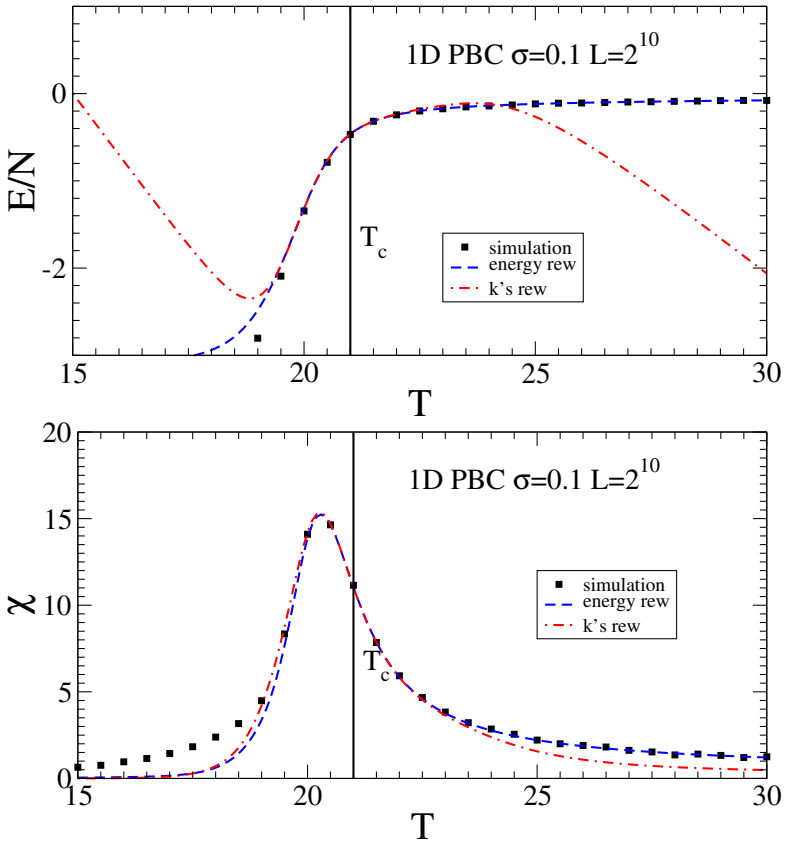

Figure 3.9: The reweighting method result is shown in this plot. We chose the T_c point to perform one run and extrapolate the rest. The black squares represent the results from simulation, and the blue line the reweighting method for using the energy rew., and the red line using the k's rew. from modified FK representation.

proposed a single-cluster variant for the FT algorithm. As well we have shown how to perform a proper summation for slow-convergence sums, applying the Ewald sum method, to allow us to compare in a proper way the system with FBCs and PBCs. Finally we also gave a reweighting method tailored to the FT update and showed that for a very close temperature using the active bond number K is as accurate as using the energy per sweep as was shown in Fig. 3.9.

Chapter 4

Analysis of Q-finite-size scaling for Ising models

4.1 Introduction

In Chapter 2 we revisited critical phenomena above the upper critical dimension, comparing the FSS derived by the RG and by MFT. We have seen that incorporating DIVs into the correlation sector is crucial to develop a new scheme, namely QFSS, and so reconcile the RG and MF. The aim of this chapter is then to check our scheme in ferromagnetic systems above d_c. To achieve our objective we have simulated the LRIM for several dimensionalities and studied the well-known 5D SRIM, which has been the focus of a long-lasting debate about the nature of FSS above d_c. These two kinds of ferromagnetic systems belong to the same universality class and so they should experience similar scaling behaviours. Indeed, the universality class can also include other type of systems such as fluids [68].

Our contribution [43] sparked a recent debate about the nature of non-zero Fourier modes [44, 69]. It was believed that the non-zero modes, which should not contain DIVs, must follow the Landau MF theory with standard FSS and $\xi \sim L$. We show

that this picture is still incompatible with both numerical simulations and with RG theory. Instead, when the DIVs are suppressed what one expects is Gaussian-fixed point exponents. The FSS associated with those exponent is named here as Gaussian FSS (GFSS). The confusion arose because some exponents take same values e.g. $\gamma^{\dagger} = \gamma$. We shall illustrate the actual picture for non-zero modes, the GFSS as a complement of QFSS, and its limitations. So in that sense we replace the standard FSS and it breakdowns by the combination of QFSS and GFSS.

The d-dimensional LRIM, with $N = L^d$, considered in this project are described by the Hamiltonian,

$$\mathcal{H} = -\sum_{\substack{i,j=1 \\ i \neq j}} J_{ij} s_i s_j + \sum_i H_i s_i, \quad \text{with} \quad J_{ij} = \frac{J}{|\mathbf{r}_i - \mathbf{r}_j|^{d+\sigma}}. \tag{4.1}$$

The coupling J_{ij} is an algebraically decaying function; it depends on the distance between two spins located at lattice positions i and j. The system has to satisfy the non-divergence of the energy, so that it is required that $\sigma > 0$. In the ferromagnetic case, here considered, the spins can only take values ± 1 and the coupling $J > 0$. The term H_i is the external magnetic field. The first sum in Eq.(4.1) runs over all the possible interactions, or bonds of the system of which there are $N_b = N(N-1)/2$.

The richness of the physics of this kind of LRIM gives us an important tool for the study of critical phenomena for continuous phase transitions, and specially in the regime above d_c. The strength of the interaction can be regulated through the σ parameter, and if one properly tunes the strength, one can drive the system to different scenarios where different approximations are taken to describe the system.

The discrete Hamiltonian for the LRIM in Eq.(4.1), expressed as ϕ^4 theory, is given by corresponding Ginzburg-Landau-Wilson action

$$S[\phi] = \int d^d x \left(f_0 + \frac{r_0}{2}\phi^2 + \frac{c}{2}|\nabla\phi|^2 + \frac{u}{4}\phi^4 - h\phi + c_\sigma \int d^d x' \frac{\phi\ \phi'}{|\mathbf{x}-\mathbf{x}'|^{d+\sigma}} \right) \quad (4.2)$$

Here, $\phi = \phi(\mathbf{x})$ is the order parameter and the last term contains the long-range interactions with $\phi' = \phi(\mathbf{x}')$. The factors c and c_σ are constants. The Hamiltonian for the 5D Ising model with nearest-neighbour interactions is easily recovered setting $c_\sigma = 0$. The physics of the long-range interactions model was firstly studied by Fisher, Ma and Nickel in [70]. They applied a treatment of RG theory finding that the critical dimension depends on the control parameter, $d_c = 2\sigma$. In other words, for a dimension d, there is a critical $\sigma_U = d/2$. That allowed them to find the fixed points, identifying three different regimes that are mapped in Fig. 4.1:

▶ for $0 < \sigma < \sigma_U = d/2$, the system is above d_c. One finds a stable Gaussian fixed-point, where critical phenomena are described by MFT. The MF critical exponents are found to be

$$\alpha = 0, \qquad \beta = \frac{1}{2}, \qquad \gamma = 1, \quad (4.3)$$

$$\delta = 3, \qquad \nu = \frac{1}{\sigma}, \qquad \eta = 2 - \sigma. \quad (4.4)$$

Besides one can add the complementary QFSS exponents

$$\wp = \frac{d}{2\sigma}, \qquad \lambda = \frac{\wp}{\nu}, \qquad \eta_\wp = 2 - \frac{d}{2}, \quad (4.5)$$

▶ for $d/2 < \sigma < \sigma_L = 2$ the critical exponents depend on σ, so non-MF exponents are expected.

▶ for $\sigma > 2$, the interaction decay is so strong that the system behaves as the SRIM.

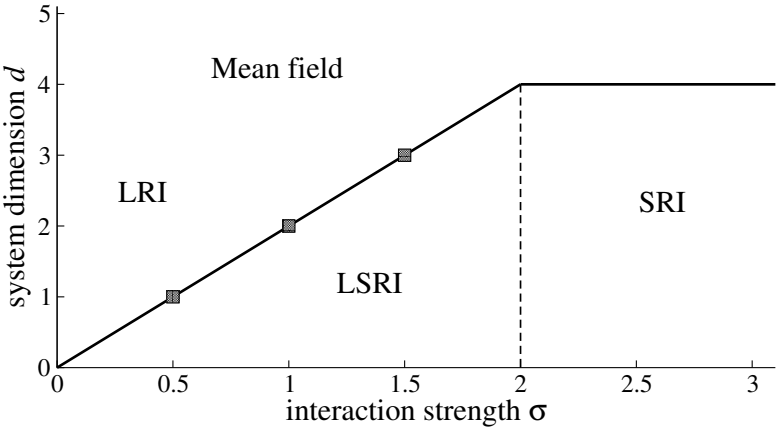

Figure 4.1: Map representing the different regions of the LRIM. The black line splits the regions in the mean-field and non-mean-field behaviour. In the long-range interactions regime MFT takes over. The long-short-interaction (LSRI) regime requires a perturbative expansion to the MFT due to the non-triviality of the fixed point there. For $\sigma > 2$ the short-range interaction (SRI) is recovered. Finally the squares denote the critical dimension regime which manifests logarithmic corrections.

Despite the fact that in this work we do not consider the regime below d_c and so we do not discuss the scaling details there, it is worth briefly mentioning some important issues about the various regimes discussed above. A long-lasting debate for the description of critical phenomena at the lower critical σ_L has been continued lately. The question is where, in fact, is the precise value at which one recovers the SRI behaviour. This was recently discussed and summarised by Parisi et *al.* in [60]. It is claimed that the lower critical range is rather $\sigma_L = 2 - \eta_{\rm SR}$ [71, 72], where the corresponding d-dimensional SRI universality class is the correlation function exponent $\eta_{\rm SR}$. In particular, for $d = 1$ this implies $\sigma_L = 1$, in agreement with exact results for this specific case [73]. Recent discussion have focused on the location of, and behaviour at, the lower critical σ_L [60, 61, 74, 75].

In line with the regimes given by the LRIM, this can actually be seen as a general formalism that also includes the SRIM. To recover scaling behaviour for the SRI systems one only has to replace σ by $\sigma_L = 2$ in the critical exponents. In this way $d_c = 2\sigma_L = 4$ and the MF exponents are easily recovered for the SRIM above d_c. The algebraically decaying interaction for long-range interactions systems allow

us to consider them above d_c, i.e., in the MF regime. We focus then on the study of the 5D SRIM, and the 1D, 2D and 3D LRIMs for such regimes. To give a complete investigation we have studied systems with both periodic and free boundary conditions (FBCs and PBCs). In this manner, we can investigate the universality of the pseudocritical exponent ϙ and the fundamental role of the correlation length as influenced by DIVs.

This project involves computational work, so we have performed simulations of the 1D, 2D and 3D LRIMs using the Fukui-Todo Swendsen-Wang algorithm. For systems with PBCs we have simulated systems sizes from approximately $N = 128$ to 262144, using the effective summed coupling in Eq.(3.55) extracted from the Ewald method. Simulating systems with FBCs requires more memory due to the lack of symmetries for the speed-up long-range interactions algorithms presented in chapter 3. Hence, we have simulated smaller system sizes with FBCs, approximately from $N = 128$ to 32768. The σ values considered here are $\sigma = 0.1$ and 0.2 for one, and two dimensional cases and $\sigma = 0.1$ and 0.3 for the three dimensional case, very deep in the mean-field region $\sigma < d/2$. We have also simulated the 5D model with nearest-neighbour interactions, which corresponds to the SRIM, with PBCs and FBCs. The simulations were carried out using the Wolff cluster algorithm, considering system sizes from $L = 20$ up to 48 for both kinds of boundaries applied. Equilibrium times and measurement frequencies were set according to an analysis of integrated autocorrelation times and the jackknife method to take into account the correlation in the data following the description of data analysis in Chapter 3. The resulting set up, was around 10^5 Monte Carlo steps for thermalisation, followed by 3×10^5 measurements. In order to find the critical point, we use the scaling through the pseudocritical temperatures which are defined when χ_L has its maxima,

$$T_L = \arg_T \max \chi_L(T). \tag{4.6}$$

In the simulation scheme the susceptibility is computed by $\chi_L = \langle m_L^2 \rangle - \langle |m_L| \rangle^2$,

where $|m_L| = |\sum_i s_i|/N$ since $\langle m_L \rangle \approx 0$. We have run several times each simulation for each system size, using the reweighting methods to identify the peak of χ_L.

This chapter is mainly divided into two major parts. Firstly, in section 2 we analyse the LRIM and 5D SRIM with PBCs and secondly with FBCs in section 3. Section 4 contains the scaling analysis when an external magnetic field is included to the model. Finally section 5 contains the conclusion.

4.2 Periodic boundary conditions

We start our analysis with PBC systems. In order to give a complete description we present the forms of the thermodynamic homogeneous functions from the RG equations. If one imposes PBCs, one can easily transform the Hamiltonian in Eq.(4.2) to its Fourier counterpart. This takes the form

$$S[\phi] = \frac{1}{2}\sum_{\mathbf{k}} \left(r_0 + c\mathbf{k}^2 + c_\sigma \mathbf{k}^\sigma\right) \phi_{\mathbf{k}}^2 + \frac{u}{4L^d} \sum_{\mathbf{k}_1,\mathbf{k}_2,\mathbf{k}_3} \phi_{\mathbf{k}_1}\phi_{\mathbf{k}_2}\phi_{\mathbf{k}_3}\phi_{\mathbf{k}_4} + hL^{d/2}\phi_0, \quad (4.7)$$

where $\mathbf{k}_4 = -\mathbf{k}_1 - \mathbf{k}_2 - \mathbf{k}_3$. Choosing the rescaling factor as b, if we rescale all the terms inside the Hamiltonian above, one can notice that the term which leads the behaviour in the LRIM is now the $|\mathbf{k}|^\sigma$ over the kinetic term $|\mathbf{k}|^2$. In that sense, rescaling the momentum $|\mathbf{k}|' = b|\mathbf{k}|$ and apply it to the long-range interactions term $|\mathbf{k}|^\sigma$ give us a rescaling relation for the field that is $\phi'_{\mathbf{k}'} = b^{-\sigma/2}\phi_{\mathbf{k}}$. Then, the other terms rescale as $c' = b^{\sigma-2}c$ for the kinetic term, as $r'_0 = b^\sigma r_0$ for the reduced temperature term, as $h' = b^{(d+\sigma)/2}h$ for the external magnetic source, and $u' = b^{2\sigma-d}u$ for the self interaction term. The eigenvalues associated with their rescaling are

$$y_t = \sigma, \qquad y_u = 2\sigma - d, \qquad y_h = \frac{d+\sigma}{2}. \quad (4.8)$$

As we have seen in Chapter 2 for the SRIM, y_u is still behaving as dangerous irrelevant variable for the LRIM above d_c when $\sigma < d/2$.

4.2.1 The zero mode ϕ_0

The Fourier modes are the components fields $\phi_{\mathbf{k}}$ of the action in the reciprocal space in Eq.(4.7). For systems with PBCs the zero mode ϕ_0 has a very important role since it is straightforwardly related to the DIV sector above d_c [42]. The action in the Fourier space can also be rewritten as

$$\begin{aligned} S[\phi] \;\simeq\; & \frac{1}{2}\quad r_0 + \frac{3u}{2L^d}\sum_{\mathbf{k}\neq 0}|\phi_{\mathbf{k}}|^2\Bigg)\Bigg(\phi_0^2 + \frac{u}{4L^d}\phi_0^4 \\ & + \frac{1}{2}\sum_{\mathbf{k}\neq 0}(r_0 + c|\mathbf{k}|^2) + c_\sigma|\mathbf{k}|^\sigma)|\phi_{\mathbf{k}}|^2 - hL^{d/2}\phi_0, \end{aligned} \tag{4.9}$$

where the ϕ_0 mode has been formally separated out. In this form, one can notice the nature of the particular scaling that is characterized by DIVs through the connection with the zero mode. Keeping aside the external-field term, ϕ_0 and u always appear together. To show the special behaviour for the zero mode, one can compute its expected value $\langle\phi_0^2\rangle$, noticing that $\langle\phi_0\rangle = 0$ by symmetry. Noticing the partition function Z given in Eq.(2.64), the square expectation value is computed through

$$\langle\phi_k^2\rangle = Z^{-1}\int\Bigg(\mathcal{D}\phi_k\;\phi_k^2\exp\Big(-S[\phi_k]\Big)\cdot\Bigg(\tag{4.10}$$

Setting $k = 0$ in for the average and neglecting other terms with $k \neq 0$, the zero mode takes the form

$$\langle\phi_0^2\rangle = \frac{r_0 L^d}{2u}\left(\frac{K_{\frac{3}{4}}\left[\frac{L^d r_0^2}{8u}\right]}{K_{\frac{1}{4}}\left[\frac{L^d r_0^2}{8u}\right]} - 1\right)\Bigg(\tag{4.11}$$

where $K_{3/4}$ and $K_{1/4}$ are the modified Bessel functions. One can then state that the leading scaling behaviour is given by

$$\langle \phi_0^2 \rangle \sim \frac{r_0 L^d}{2u} \sim L^{d/2}. \tag{4.12}$$

There, we have replaced r_0 by t, then used the scaling power law for the correlation length $\xi \sim t^{-\nu}$ and we have finally introduced the QFSS ansatz $\xi \sim L^{\text{ϙ}}$.

However, if one considers that $u \to 0$, the last ϕ^4 action transforms into the Gaussian action, simpler model, given by

$$S[\phi] = \frac{1}{2} \sum_k (r_0 + c|\mathbf{k}|^2) + c_\sigma |\mathbf{k}|^\sigma) \phi_k^2. \tag{4.13}$$

Either computing Eq.(4.10) for this Gaussian model or taking the limit for Eq.(4.11) when $u \to 0$, one gets this scaling behaviour for the zero mode

$$\langle \phi_0^2 \rangle^\dagger = \lim_{u \to 0} \langle \phi_0^2 \rangle = \frac{1}{r_0} \sim L^\sigma. \tag{4.14}$$

We applied the same relations than we used to obtain Eq.(4.12), but in this case the scaling for the correlation length follows $\xi \sim L$. DIVs always need to be taken into account in order to describe properly the critical phenomena above d_c, nevertheless we will see some regimes where u is suppressed as the at the critical point for systems with FBCs, or in the scaling of the non-zero modes.

4.2.2 RG equations and free energy density

If one applies the RG theory, one gets the direction of the fluxes and so the fixed points for the model as shown in Ref.[4, 70] by Fisher, Ma and Nickel. Here, we use as a guide the work done by Luijten and Blöte in [36, 58]. The RG method for the LRIM with PBCs leads the following system of first-order differential equations

for the r_0 and u variables, with $l = \ln b$,

$$\frac{dr_0}{dl} = \sigma r_0 + 3au(c - r_0), \tag{4.15}$$

$$\frac{du}{dl} = \epsilon u - 9au^2. \tag{4.16}$$

Here we denote $\epsilon = 2\sigma - d$, and a and c are constants. Above d_c, one then applies $\epsilon < 0$. The solution for the second equation is

$$u(l) = \frac{\bar{u}e^{\epsilon l}}{1 + 9a\bar{u}\epsilon^{-1}\left(e^{\epsilon l} - 1\right)}, \tag{4.17}$$

where $\bar{u} = u(l = 0)$. The solution for the other equation, in terms of leading order $u(l)$ and in a compact form, is

$$\begin{aligned} r_0(l) &= e^{\sigma l}\left(\bar{r}_0 + \frac{3ac\bar{u}}{d-\sigma}\right)\left(\frac{u(l)}{e^{\epsilon l}\bar{u}}\right)^{\frac{1}{3}} - \frac{3acu(l)}{d-\sigma}, \\ &= e^{\sigma l}\left(\bar{r}_0 + \tilde{a}\bar{u}\right)\left(\frac{u(l)}{e^{\epsilon l}\bar{u}}\right)^{\frac{1}{3}} + \tilde{a}u(l) \end{aligned} \tag{4.18}$$

with $\bar{r}_0 = r_0(l = 0)$ and $\tilde{a} = -3ac/(d-\sigma)$. These two functions $u(l)$ and $r_0(l)$ control the flow towards the fixed point. Above d_c these variables flow to a Gaussian fixed point which is stable. The RG exponents $y_t = \sigma$ and $y_u = \epsilon = 2\sigma - d$ are immediately identified in Eq.(4.17) and Eq.(4.18). The scaling of the free energy of the system is constructed through the variables $r_0(l)$ and $u(l)$ and its derivatives. Hence, the free energy density function, up to leading order, is given by

$$f_L(t, h, u) = b^{-d}\tilde{f}_{L/b}\left(b^{y_t}[t + \tilde{a}ub^{y_u - y_t}], b^{y_h}h, b^{y_u}u\right) + \tilde{g}_L. \tag{4.19}$$

The functions $\tilde{f}_{L/b}$ and $\tilde{g}_L$ respectively are the singular and analytical part of the free energy. For temperatures below the critical point the free energy becomes singular at $u = 0$, leading to the breakdown of FSS. To overcome this problem one has to rescale the singular part of the free energy in terms of DIVs [58] to take

them into account. One considers this approximation

$$\tilde{f}_{L/b}(t,h,u) \simeq \ln \int_{-\infty}^{\infty} d\phi \ \exp\left[r_0\phi^2 - u\phi^4 + h\phi\right] \tag{4.20}$$

Then one rescales the field absorbing DIVs, $\phi'^4 = u\phi^4$. The free energy is now given by

$$F_{L/b}(t',h') \simeq \ln \int_{-\infty}^{\infty} d\phi' \ \exp\left[r_0'\phi'^2 - \phi'^4 + h'\phi'\right] \tag{4.21}$$

Where the reduced temperature term and the external magnetic field have respectively been rescaled as $t' = tu^{-1/2}$ and $h' = hu^{-1/4}$. In this manner, the singular part of the energy takes the full dependence of DIVs in a implicit manner. Hence,

$$F_{L/b}(t',h') + g_0 = \tilde{f}_{L/b}(t,h,u) + \tilde{g}_L, \tag{4.22}$$

where g_0 does not contain any further relevant information about the scaling or DIVs, and so it can be omitted [4, 76]. Then the free energy density is given by the rescaled version, with the information implicitly in t and h,

$$f_L(t,h) = b^{-d} F_{L/b}\left(b^{y_t^*} u^{-1/2}[t + \tilde{a}ub^{y_u - y_t}], b^{y_h^*} u^{-1/4} h\right) \tag{4.23}$$

with the rescaled exponents $y_t^* = d/2$ and $y_h^* = 3d/4$. Indeed, this energy function is similar to Eq.(2.95), but is a more complete version due to the consideration of first-order corrections.

4.2.3 Shifting, rounding and heat capacity scaling

The first results, presented here, are those from the energy sector involving the shift and rounding exponents and the scaling for heat capacity. The scaling relation for the pseudocritical temperature, approaching the critical point, is extracted by the first argument of density energy function in Eq.(4.23). The subsequent

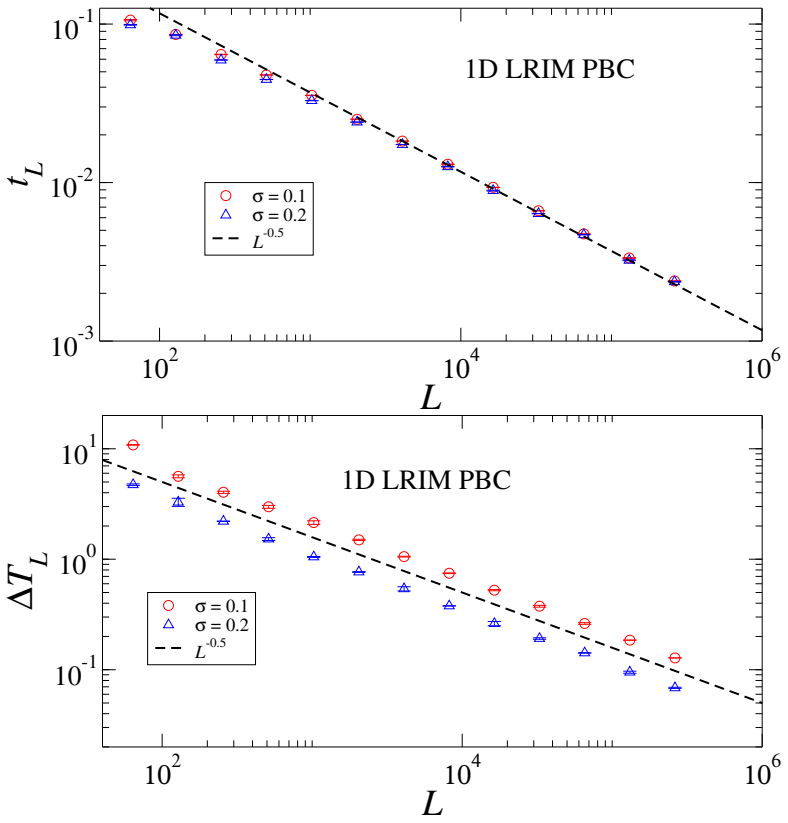

Figure 4.2: FSS for the shift and rounding exponents above d_c for the 1D LRIM with PBCs for two σ values 0.1 and 0.2. Top figure shows that the pseudocritical points scale as $t_L \sim L^{-1/2}$ following the dashed line. The bottom figure shows the scaling for the rounding, following $\Delta T_L \sim L^{-1/2}$ denoted by the dashed line. QFSS predictions match perfectly such scaling behaviours.

derivatives from the free energy, as the heat capacity or the susceptibility depend on the same arguments too. Hence, the universal function for the susceptibility $\mathcal{X}_{L/b}(b^{y_t^*}u^{-1/2}[t+\tilde{a}ub^{y_u-y_t}], b^{y_h^*}u^{-1/4}h)$, has to satisfy $\dfrac{\partial}{\partial t}\mathcal{X}_{L/b}=0$ at T_L where the peak is manifested. The solution is that the first argument takes a constant value z. Then $b^{y_t^*}u^{-1/2}[t+\tilde{a}ub^{y_u-y_t}]=c$ with $b=L$. Hence, for the LRIM above d_c the scaling up to the first-order is given by an expression as

$$t_L = c_0 L^{-\lambda}\left(1-c_1 L^{-\omega}\right)\Bigg(\tag{4.24}$$

where $\lambda = y_t^* = d/2$ is the shift exponent and $\omega = -y_t^* - y_u + y_t = d/2 - \sigma$ is the shift first-order correction usually called the Wegner exponent.

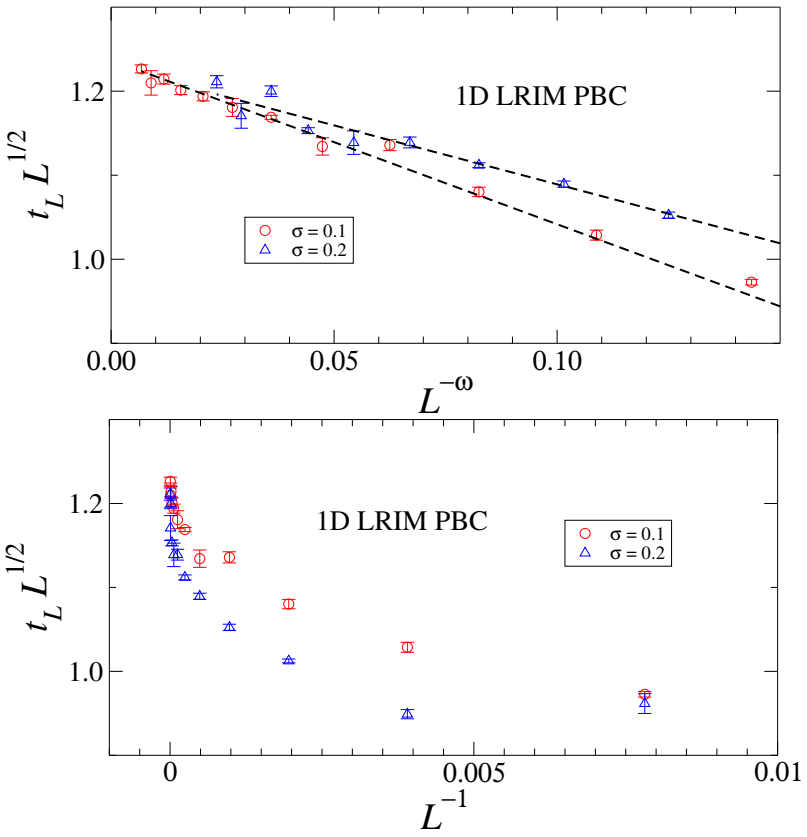

Figure 4.3: FSS first-order correction for the shift in 1D LRIM with PBCs for two σ values. In the top image the t_L has been normalised by the predicted scaling $t_L \sim L^{-1/2}$, and the y-axis have also been rescaled by its corresponding $\omega = 0.4$ and 0.3 for $\sigma = 0.1$ and 0.2 respectively. The points follow the straight lines denoted by dashed lines. The image below shows the first correction to scaling with another kind of scaling correction $\omega = 1$. This correspond to the typical scaling correction $t_L \sim L^{-d/2}(1 + AL^{-1} + \mathcal{O}(L^{-2}))$, in order to emphasise the validity of the theoretic corrections in the top image.

After the T_L points for different system sizes are found, we proceed to find the critical point T_c, recalling $t_L = T_L/T_c - 1$. We have fitted these points to the scaling expression

$$T_L = T_c - z_0 L^{-\lambda} \left(1 - z_1 L^{-\omega}\right) \left(\tag{4.25}$$

but firstly neglecting the corrections corresponding to z_1 and $\omega = 0$ (the constant z_0 is already multiplied by T_c). Using T_c, z_0 and λ as free parameters, we have checked that the results are in the proper range of values. Then we have imposed λ to its theoretic value and we have estimated T_c. Then we have imposed T_c

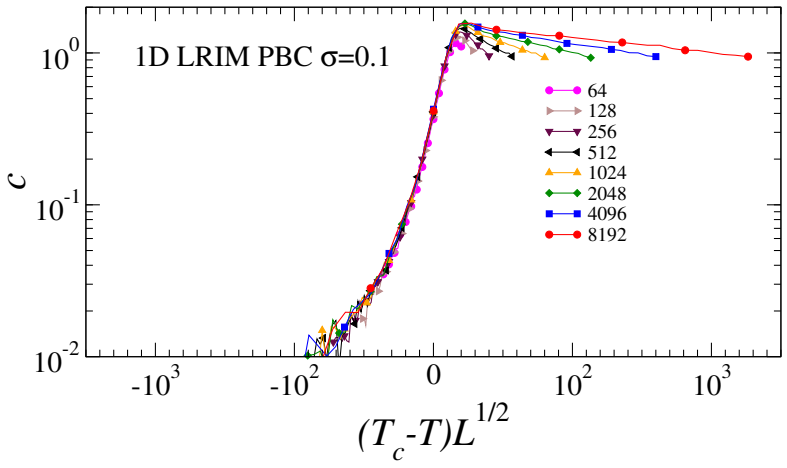

Figure 4.4: Normalised scaling for the heat capacity in 1D LRIM with PBCs for $\sigma = 0.1$. The image are in favour of the MF value $\alpha = 0$ with QFSS prediction for $\lambda = d/2$, as the lines collapse although first order correction seems to be quite important.

and estimated λ. As well, in every fit we have removed the small system sizes to avoid an excess of corrections, until the fit satisfied a minimum fit quality given by the χ^2 test. We have fitted the rounding only to the leading scaling $\Delta T_L \sim L^{-\theta} = L^{-d/2}$. Those results are contained in Table 4.1 and they can be seen in Fig. 4.2. We have also estimated the first-order corrections fitting Eq.(4.24) following the similar procedure as before but with more parameters. The results containing the corrections are gathered in Table 4.2. In Fig. 4.3 we can observe that the corrections are correctly described by the theoretic prediction from Eq.(4.24).

Table 4.1: Results corresponding to the temperature sector for LRIM. For different dimension d and σ values. We have estimated the critical points and the exponents for shift λ and the rounding θ.

d	σ	T_c	$\lambda = d/2$	$\theta = d/2$
1	0.1	21.0013(3)	0.499(1)	0.503(5)
	0.2	10.8421(2)	0.501(1)	0.488(9)
2	0.1	65.3381(6)	0.993(5)	1.001(8)
	0.2	33.8384(5)	0.993(4)	0.995(6)
3	0.1	129.415(1)	1.493(6)	1.484(9)
	0.3	45.5543(6)	1.487(7)	1.491(8)
5	2.0	8.77847(1)	2.437(8)	2.481(7)

Table 4.2: Results corresponding to the temperature sector for LRIM. Different dimension d and σ values where analysed. We have estimated T_c and the exponents for shift λ and its first-order correction ω.

d	σ	T_c	$\lambda = d/2$	$\omega = d/2 - \sigma$
1	0.1	21.0000(3)	0.500(2)	0.41(3)
	0.2	10.8419(5)	0.503(4)	0.32(4)
2	0.1	65.3376(9)	0.998(3)	0.86(9)
	0.2	33.8397(5)	1.000(3)	0.82(9)
3	0.1	129.431(2)	1.500(5)	1.51(20)
	0.3	45.5541(8)	1.500(6)	1.20(20)
5	2.0	8.77846(2)	2.502(1)	0.491(1)

To conclude the energy sector analysis, we investigate the heat capacity too. For the 1D LRIM with $\sigma = 0.1$ in PBCs we can observe in Fig. 4.4 how the lines collapse under a scaling using QFSS predictions. Up to leading order, the heat capacity scale approaching a constant behaviour since $\alpha = 0$,

$$c_L(t) \sim z_0 L^{\mathfrak{Y}\alpha/\nu} = z_0. \tag{4.26}$$

4.2.4 Magnetization and susceptibility

The magnetisation and susceptibility are respectively given in terms of energy density Eq.(4.23) with $b = L$ by

$$m_L(t) = -\frac{\partial f_L}{\partial h} = L^{d-y_h^*}\mathcal{M}\left(L^{y_t^*}u^{-1/2}\tilde{t}, L^{y_h^*}u^{-1/4}h\right), \tag{4.27}$$

$$\chi_L(t) = \frac{\partial^2 f_L}{\partial h^2} = L^{d-2y_h^*}\mathcal{X}\left(L^{y_t^*}u^{-1/2}\tilde{t}, L^{y_h^*}u^{-1/4}h\right), \tag{4.28}$$

where $\tilde{t} = t + \tilde{a}uL^{y_u - y_t}$. Expanding both universal functions $\mathcal{M}$ and $\mathcal{X}$ up to first-order corrections and expressing the scaling dimensions in terms of critical exponents, they take the form

$$m_L(t) = z_0 L^{-\mathfrak{Y}\beta/\nu}(1 + z_1 L^{-\omega}), \tag{4.29}$$

$$\chi_L(t) = \tilde{z}_0 L^{\mathfrak{Y}\gamma/\nu}(1 + \tilde{z}_1 L^{-\omega}). \tag{4.30}$$

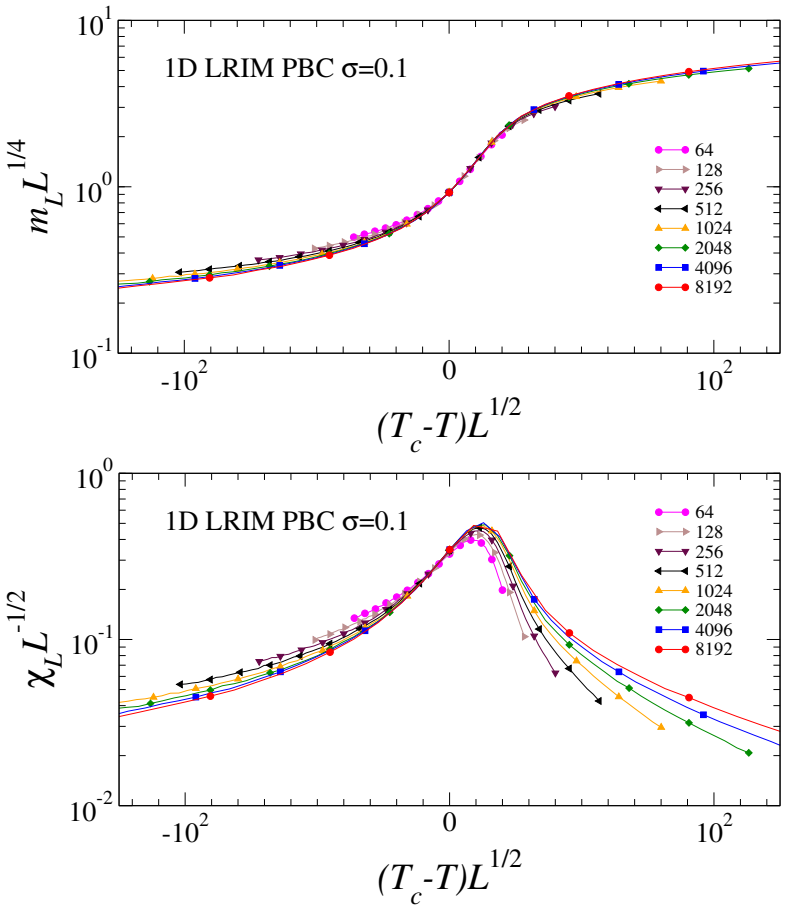

Figure 4.5: Normalised scaling for magnetisation and susceptibility for the 1D LRIM with PBCs. In both images the two observables have been normalised following QFSS, the lines visibly collapse for m_L, and for chi_L this collapse is not so clear because the corrections are stronger there.

The validity of QFSS can be seen in the normalised plots for the m_L and χ_L in Fig. 4.5. The complete results for PBCs are gathered in Table 4.3. For this case we have only estimated the corrections for the 1D model. These corrections are extracted for the m_L at T_L points, where the corrections are stronger than at T_c. We have found $\omega(\sigma = 0.1) = 0.43(4)$ and $\omega(0.2) = 0.36(4)$. For χ_L at T_L, these corrections are $\omega(\sigma = 0.1) = 0.41(3)$ and $\omega(0.2) = 0.36(6)$. These results are plotted in Fig. 4.6 and 4.7, where the validity of the theoretical corrections are visible. The scaling for the magnetization of the 5D SRIM with PBCs was already verified in favour of QFSS [77–79].

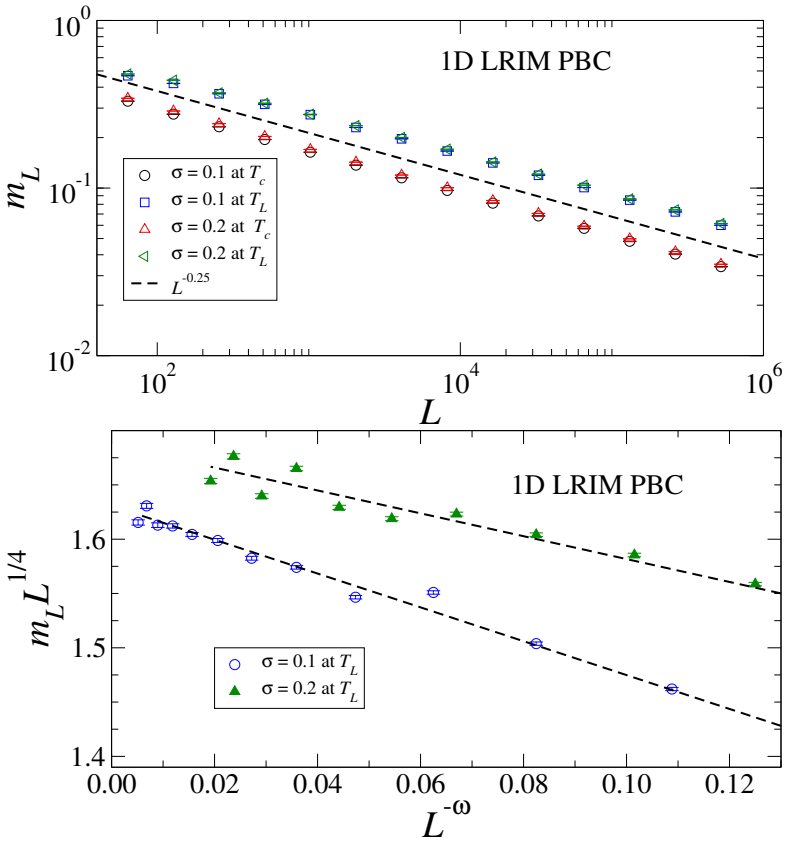

Figure 4.6: FSS for magnetisation for the 1D LRIM with PBCs. In the top image the magnetisation clearly scales as $m_L \sim L^{-1/4}$ following the dashed line. The bottom image shows the normalised magnetisation versus the expected scaling for the first-order corrections. Through this rescaling one expects a linear behaviour which is manifestly visible for the dashed lines. The respectively ω values for $\sigma = 0.1$ and 0.2 are $\omega = 0.4$ and 0.3.

4.2.5 Correlation function and correlation length

The most relevant new features of QFSS are related to the correlation sector, due to the crucial role that the correlation length plays and the anomalies with the correlation function scaling with η_ϱ. A modified Ornstein-Zernicke form of the propagator [80],

$$\hat{G}(k) \sim \frac{1}{m^2 + k^2 + k^\sigma}, \tag{4.31}$$

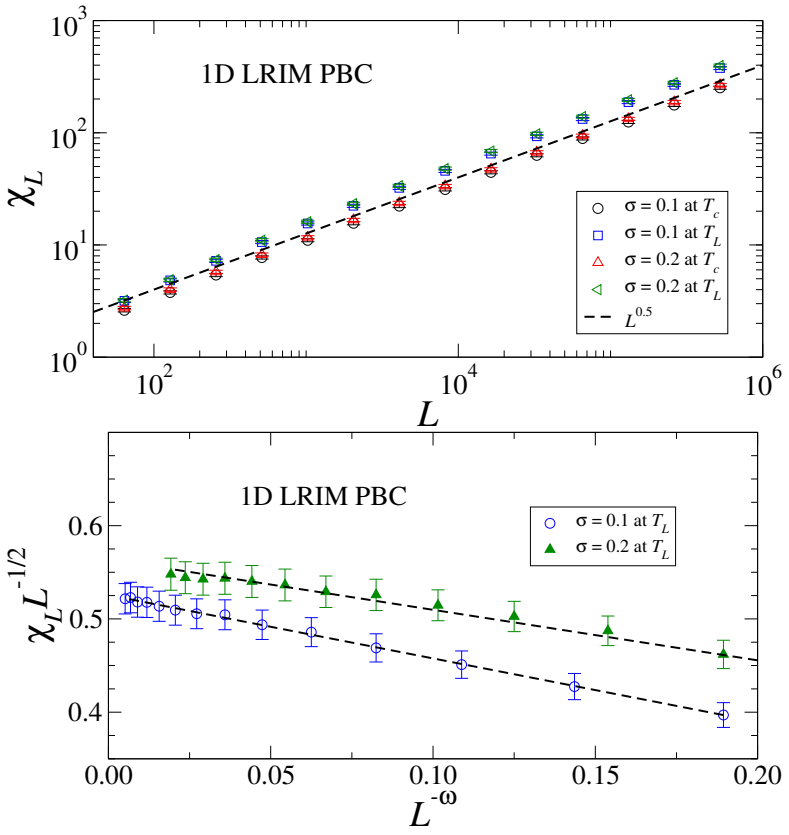

Figure 4.7: FSS for susceptibility for the 1D LRIM with PBCs. In the top image the susceptibility clearly scales as $\chi_L \sim L^{1/2}$ following the dashed line. The bottom image shows the normalised susceptibility versus the expected scaling for the first-order corrections. Through this rescaling one expects a linear behaviour which is manifestly visible for the dashed lines. The respectively ω values for $\sigma = 0.1$ and 0.2 are $\omega = 0.4$ and 0.3.

where for $\sigma < 2$ shows that the k^σ is the dominant long wavelength contribution. Hence, the correlation length can be estimated from [81]

$$\xi_L(t,h) = \frac{1}{2\sin(k_{\min}/2)} \left[\frac{\tilde{G}(0)}{\tilde{G}(k_{\min})} - 1 \right]^{\frac{1}{\sigma}}. \tag{4.32}$$

Here, $k_{\min} = 2\pi/L$ is chosen to be the smallest wave vector for the periodic lattice. The scaling of the correlation length ξ for the LRIM, can be derived from the last expression with $\tilde{G}(0) = \langle \phi_0 \rangle \sim L^{d/2}$, one finds

$$\xi_L(t,h) \sim L \left[\frac{G_0 L^{d/2}}{G_{\min} L^\sigma} - 1 \right]^{\frac{1}{\sigma}} \sim \left(L^{d/2} - L^\sigma \right)^{1/\sigma} \sim L^{d/2\sigma}. \tag{4.33}$$

Table 4.3: This table gathers some of the simulation results with PBCs for the scaling exponents and compare them with QFSS predictions. The observables analysed are $m_L \sim L^{-\wp\beta/\nu}$, $\chi_L \sim L^{\wp\gamma/\nu}$, $\xi_L \sim L^{\wp}$ and $G_L(L/2) \sim L^{-(d-2+\eta_\wp)}$.

d	σ	T	$\wp\beta/\nu = d/4$	$\wp\gamma/\nu = d/2$	$\wp = d/d_c$	$d-2+\eta_\wp = d/2$
1	0.1	T_c	0.248(1)	0.503(2)	5.03(2)	0.498(3)
		T_L	0.248(1)	0.504(2)	4.96(3)	0.496(1)
	0.2	T_c	0.249(1)	0.504(2)	2.49(2)	0.490(2)
		T_L	0.246(1)	0.508(2)	2.50(2)	0.491(4)
2	0.1	T_c	0.502(1)	1.000(5)	9.96(3)	0.997(8)
		T_L	0.496(1)	1.007(5)	9.95(4)	0.984(8)
	0.2	T_c	0.496(1)	1.004(5)	5.04(4)	0.984(8)
		T_L	0.492(1)	1.008(5)	4.99(4)	0.978(9)
3	0.1	T_c	0.749(2)	1.512(8)	15.07(5)	1.484(12)
		T_L	0.743(3)	1.513(9)	15.04(6)	1.489(11)
	0.3	T_c	0.752(4)	1.504(7)	4.98(5)	1.495(9)
		T_L	0.744(4)	1.511(9)	4.96(4)	1.486(12)
5	2.0	T_c	1.25(1)	2.49(3)	1.25(1)	2.49(2)
		T_L	1.22(1)	2.43(8)	1.23(1)	2.46(3)

For universal functions one expects a crossing point near to the critical point. In the upper plot in Fig. 4.8, one can observe that if the universal function $\Xi_L \sim \xi_L/L^{\wp}$, up to minor corrections, is plotted as a function of temperature, a crossing point near T_c is shown. In the lower picture one observes the QFSS for the correlation function at $x = L/2$ is collapsed. In Fig. 4.9 we have also plotted ξ_L and $G(L/2)$ in terms of system size. One can observe in both plots strongly support QFSS, specially for the correlation length where the slope show straightforward the value of $\wp$ for two values of σ, $\wp = 5$ and $\wp = 2.5$ respectively for $\sigma = 0.1$ and 0.2.

The scaling behaviour for the correlation function was also an open debate, but the predictions by QFSS prevails with $G(L/2)^{-d/2}$, with $d-2+\eta \neq d/2$ and indeed $d-2+\eta_\wp = d/2$ [11, 43]. The decaying of $G(x)$, in terms of lattice position x is still unclear, hence it is also investigated here. We have plotted in Fig. 4.10 the unconnected and the connected correlation function, G and G_c respectively, for 1D LRIM with PBCs $\sigma = 0.1$ for $L = 2^{20}$. One can argue that the behaviour

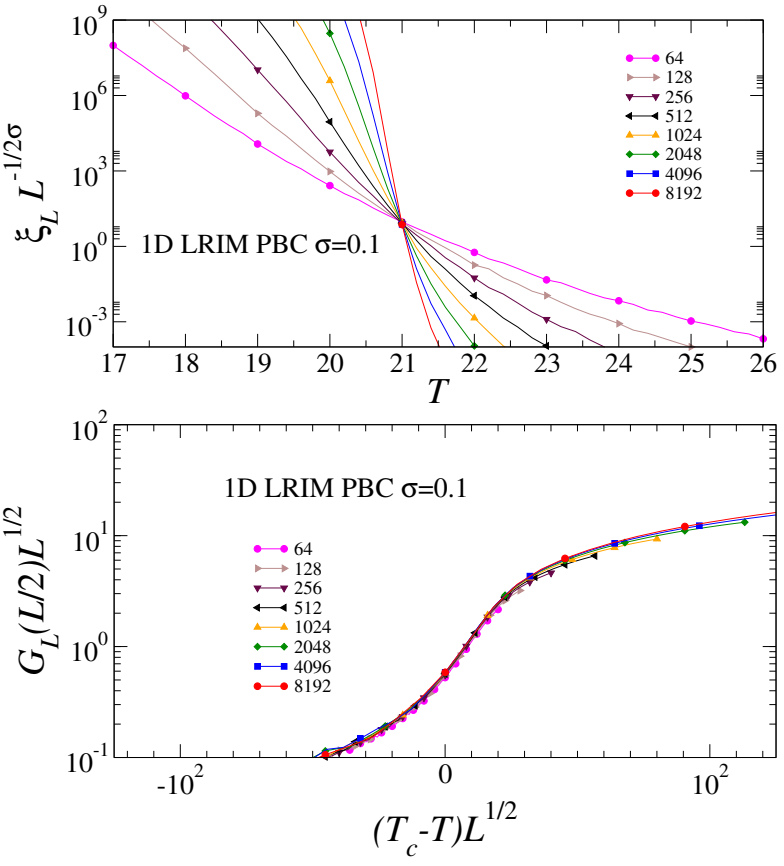

Figure 4.8: Normalised scaling for the correlation length and correlation function for the 1D LRIM with PBCs. In the both images these two observables have been normalised following QFSS. For the correlation length a plot of the universal function $\Xi_L \sim \xi_L L^{-\text{ϙ}}$ clearly exhibit a crossing point at $T_c \approx 21$, the corresponding critical temperature for $\sigma = 0.1$. Under this rescaling the correlation function collapses into a single curve.

associated with QFSS appears in G due to the zero mode, otherwise for G_c which the zero mode is suppressed should not contain such QFSS behaviour. One actually can observe a crossover between the QFSS and the FSS for both $G(x)$. It seems that for short distances FSS is leading the behaviour but in a middle region QFSS appears to prevail there.

4.2.6 Non-zero modes

For systems with PBCs the other Fourier modes, apart from the zero mode, $\phi_{\mathbf{k}\neq\mathbf{0}}$ are not projected to the real magnetisation and a priori less interesting, but these

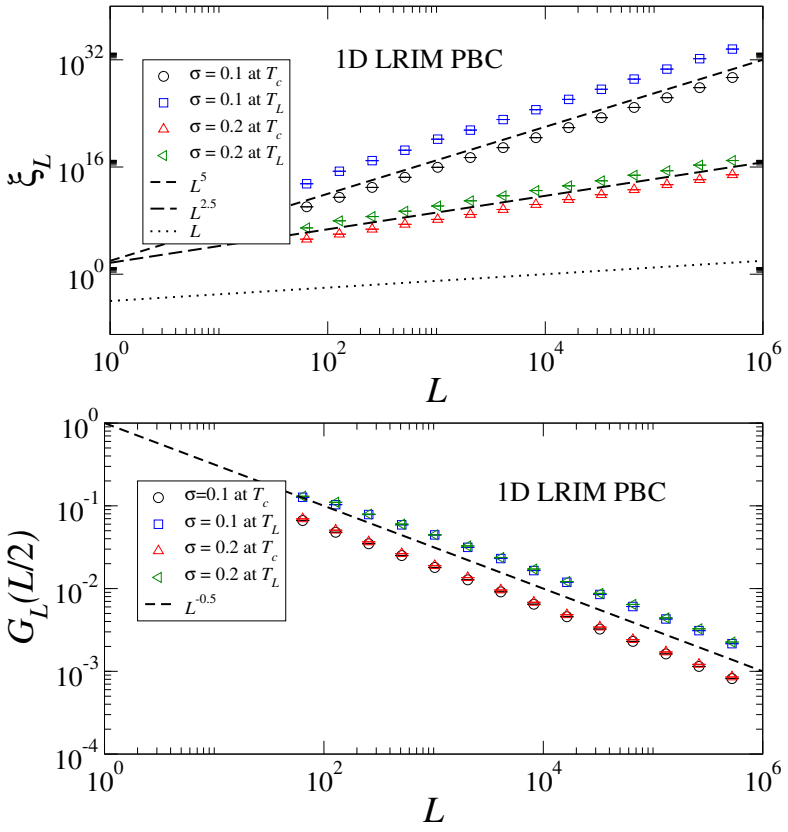

Figure 4.9: FSS for the correlation sector for the 1D LRIM. In the upper image the correlation length clearly scales as $\xi_L \sim L^{\wp}$ with $\wp = 5$ for the system with $\sigma = 0.1$ denoted by the short dashed line and $\wp = 2.5$ for $\sigma = 0.2$, denoted the long dashed line. The lower image shows the correlation function scaling as $G_L(L/2) \sim L^{-1/2}$ for the dashed line. Both are manifestly in favour of QFSS.

modes can actually become a tool to test the theory, if one wants to see the consequences of DIVs being suppressed. To simplify the notation we label the modes regarding if they are influenced or not by DIVs. In this manner, the Q-modes will be those modes that follow QFSS and so are affected, the modes following GFSS will be labelled as G-modes. For PBCs the magnetisation modes are given by

$$m_{\mathbf{k}} = \langle \phi_{\mathbf{k}} \rangle = \left\langle \int \left(d^d x \ \phi(\mathbf{x}) \psi_{\mathbf{k}}(\mathbf{x}) \right\rangle \right(\tag{4.34}$$

where $\psi_{\mathbf{k}}(x) = e^{i\mathbf{k}\cdot\mathbf{x}}$ is standing wave in the periodic case, but it depends on the nature of the boundaries. The brackets indicate the thermal average with the Boltzmann weight corresponding to the action. The equilibrium magnetisation is

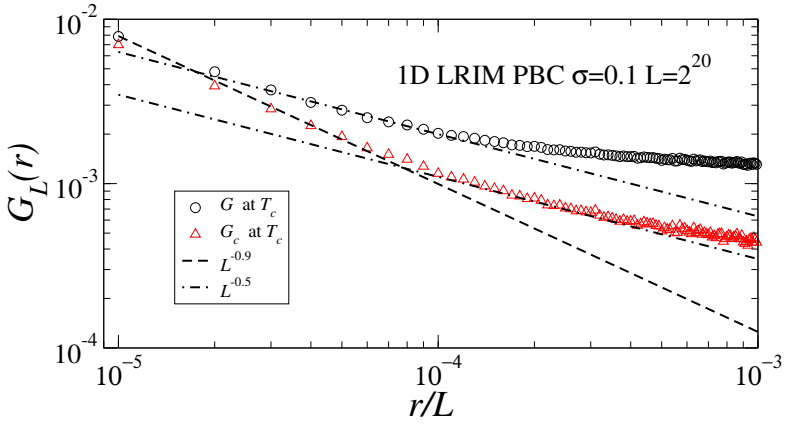

Figure 4.10: Correlation function in terms of distance for the 1D LRIM with PBCs. The dashed lines shows the QFSS and the Landau FSS respectively by $L^{-0.5}$ and $L^{-0.9}$, one can observe a crossover between both of them. For short distances Landau FSS seems to dominate, but for intermediate distances QFSS seems to take over.

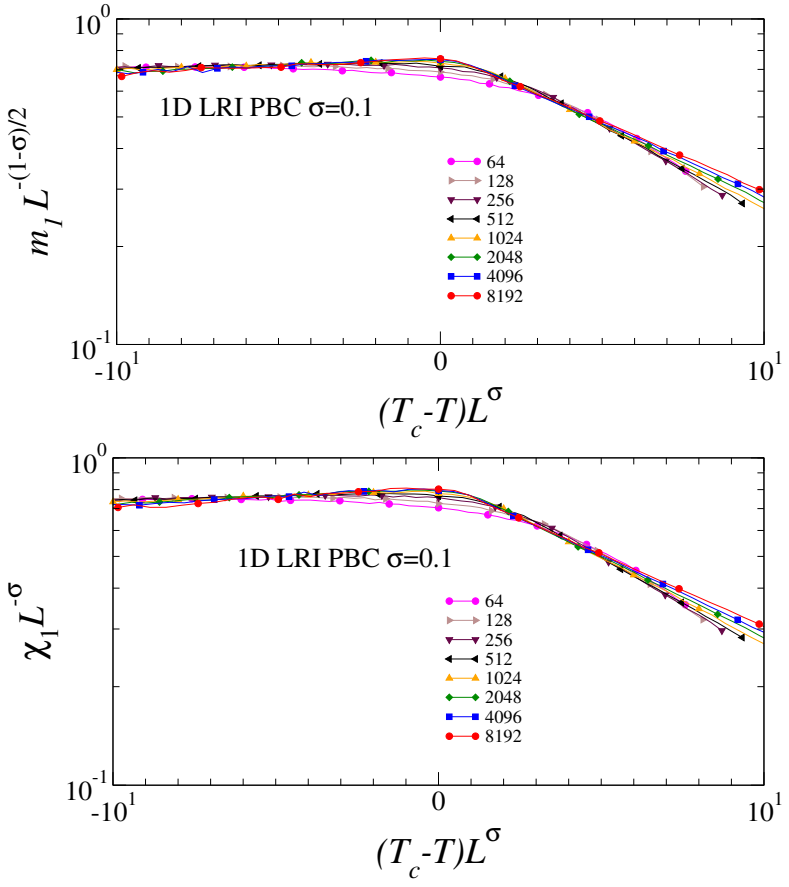

Figure 4.11: Normalised scaling of the first modes for magnetisation and susceptibility for 1D LRIM with PBCs. In both image these two observables have been normalised following GFSS, the lines visibly collapse.

then

$$m = \left\langle \int \left(d^d x \sum_{\mathbf{k}} \phi_{\mathbf{k}} \psi_{\mathbf{k}}(\mathbf{x}) \right\rangle \right(\tag{4.35}$$

The Q-modes acquire nonvanishing expectation values and have projections onto the equilibrium magnetisation as discussed by Rudnick, Gaspari and Privman in [82] and lately by Wittmann and Young in [69]. Going to the detail now, one has to be careful when measuring the magnetisation modes during the simulation. Firstly, one considers the transformation of the spins

$$\tilde{S}_{\mathbf{k}} = \sum_{\mathbf{n}=0}^{L-1} \left(e^{i\mathbf{k}\cdot\mathbf{n}} S_{\mathbf{n}}, \right. \tag{4.36}$$

where $\mathbf{n}$ is the position of the spin over the lattice and $\mathbf{k} = 2\pi/L\hat{\mathbf{k}}$ with $\hat{\mathbf{k}} = 0, \ldots, L-1$. Its inverse transformation is

$$S_{\mathbf{n}} = \frac{1}{L^d} \sum_{\mathbf{k}=0}^{L-1} e^{-i\mathbf{k}\cdot\mathbf{n}} \tilde{S}_{\mathbf{k}}. \tag{4.37}$$

The magnetisation mode is,

$$m_{\mathbf{k}} = \frac{1}{L^d} \langle \tilde{S}_{\mathbf{k}} \rangle. \tag{4.38}$$

The nature of the mode can easily be observed. The only contribution to the real magnetisation is given by the $\tilde{S}_0$ mode, all the rest do not contribute. Exactly the same happens to the susceptibility modes, which are defined as

$$\chi_{\mathbf{k}} = L^d \langle |m_{\mathbf{k}}|^2 \rangle, \tag{4.39}$$

where the brackets are the thermal average. This $\chi_{\mathbf{k}}$ modes are related with the correlation functions in the following manner: the connected one can be written as $G_c(s_i, s_j) = \langle s_i s_j \rangle - m^2$, and then its Fourier transform is

$$\tilde{G}_c(\mathbf{k}) = L^{-d} \langle |\tilde{S}'_{\mathbf{k}}|^2 \rangle \tag{4.40}$$

with $S_i' = S_i - m$. The transform of the unconnected one is given by

$$\tilde{G}(\mathbf{k}) = L^{-d}\langle|\tilde{S}_{\mathbf{k}}|^2\rangle. \tag{4.41}$$

These two functions $\tilde{G}_c(\mathbf{k})$ and $\tilde{G}(\mathbf{k})$, in Fourier space, are exactly the same if $\mathbf{k} \neq 0$. The difference resides in the zero mode, that makes $\tilde{G}_c(0) \neq \tilde{G}(0)$. In fact $\tilde{G}_c(\mathbf{k}) = 0$ and $\tilde{G}(\mathbf{k}) = L^d\langle m^2\rangle$. Hence

$$\tilde{G}(\mathbf{k}) = \chi_{\mathbf{k}}. \tag{4.42}$$

Going back to the magnetisation, Eq.(4.34) is not a good definition for MC simulation since its thermal average vanishes, $\langle m\rangle = 0$. Instead, one has artificially broken the symmetry and to consider $\langle|m|\rangle$, and

$$|m_{\mathbf{k}}| = L^{-d}\langle|\tilde{S}_{\mathbf{k}}|\rangle = L^{-d}\langle|\sum_{\mathbf{x}}\mu(\mathbf{x})\psi_{\mathbf{k}}(\mathbf{x})|\rangle, \tag{4.43}$$

where $\mu(\mathbf{x})$ is the local oriented spin per site, so the average magnetisation per spin along the lattice size position, and it is defined by

$$\mu(\mathbf{x}) = \langle S_{\mathbf{x}}(\text{sign}[M] + \delta_{M,0})\rangle, \tag{4.44}$$

where $M = \sum_{\mathbf{x}} S_{\mathbf{x}}$. The magnetisation then is easily recovered as $m = L^{-d}\sum_{\mathbf{x}}\mu_{\mathbf{x}}$. This $\mu(\mathbf{x})$ variable it is not very useful for PBCs because in such conditions the average per spin just take the average of the system and so $\mu(\mathbf{x}) = \langle|m|\rangle$. However for FBCs it will be very useful to see the profile distribution.

Having clarified how to manage the various Fourier modes $m_{\mathbf{k}}$ and $\chi_{\mathbf{k}}$ in the computational scheme, we next give the FSS for each observable. The standard picture for G-modes, where MF prevails above d_c even though DIVs are suppressed, is incorrect. In particular, Wittmann and Young in [69] claimed that the susceptibility exponent, γ, maintains the mean field value $\gamma = 1$. We claim here that the picture

is incomplete. Indeed when no DIVs are involved one expects a Gaussian fixed-point, delivering a Gaussian exponent. Analysing the susceptibility is not enough since $\gamma^\dagger = 1$ has the same value as mean field. Hence, in order to validate our claim we look at the magnetisation since $\beta \neq \beta^\dagger$. In fact, the prediction for such observables for the G-modes with Gaussian fixed point exponent are found to be for the LRIM.

Hence one can state that the Q and G modes follow different thermodynamic functions. To distinguish these two behaviours for the moments, one can refer with † superscript the thermodynamic functions corresponding to the Gaussian model which include the behaviour of $\mathbf{k} \in G$. So

$$f_L(t,h,u) = b^{-d} F_{L/b}\left(b^{y_t^*}t, b^{y_h^*}h\right), \tag{4.45}$$

$$f_L^\dagger(t,h,u) = b^{-d} F_{L/b}^\dagger\left(b^{y_t}t, b^{y_h}h\right). \tag{4.46}$$

For the magnetisation and susceptibility, the G-modes scale respectively

$$m_L^\dagger(t) = -\frac{\partial f_L^\dagger}{\partial h} = L^{-d+y_h}\mathcal{M}^\dagger\left(b^{y_t}t, b^{y_h}h\right) \sim L^{-(d-\sigma)/2}, \tag{4.47}$$

$$\chi_L^\dagger(t) = \frac{\partial^2 f_L^\dagger}{\partial h^2} = L^{-d+2y_h}\mathcal{X}^\dagger\left(b^{y_t}t, b^{y_h}h\right) \sim L^{\sigma} \tag{4.48}$$

The considered modes analysed here, for systems with PBCs, are defined by the shortest reciprocal vector. The first component takes 1, and the rest zero. For 1D this is $\hat{\mathbf{k}}_1 = 1$, for 2D $\hat{\mathbf{k}}_1 = [1,0]$, for 3D $\hat{\mathbf{k}}_1 = [1,0,0]$ and for 5D $\hat{\mathbf{k}}_1 = [1,0,0,0,0]$ respectively. In Fig. 4.11 we plotted the renormalised scaling for the first non-zero modes of the magnetization and the susceptibility in terms of closeness to the critical point for 1D LRIM. The FSS for such modes are plotted in Fig. 4.12 and the values for their slopes are written down in Table 4.4. One can observe that the results clearly follow the scaling predictions presented in Eqs.(4.47) and (4.48). This shows that the correct picture there is the GFSS instead of the standard FSS

when DIVs are suppressed. The distinguishing was possible for the magnetisation due to the difference in the value held for the $\beta^\dagger$ which is σ dependent.

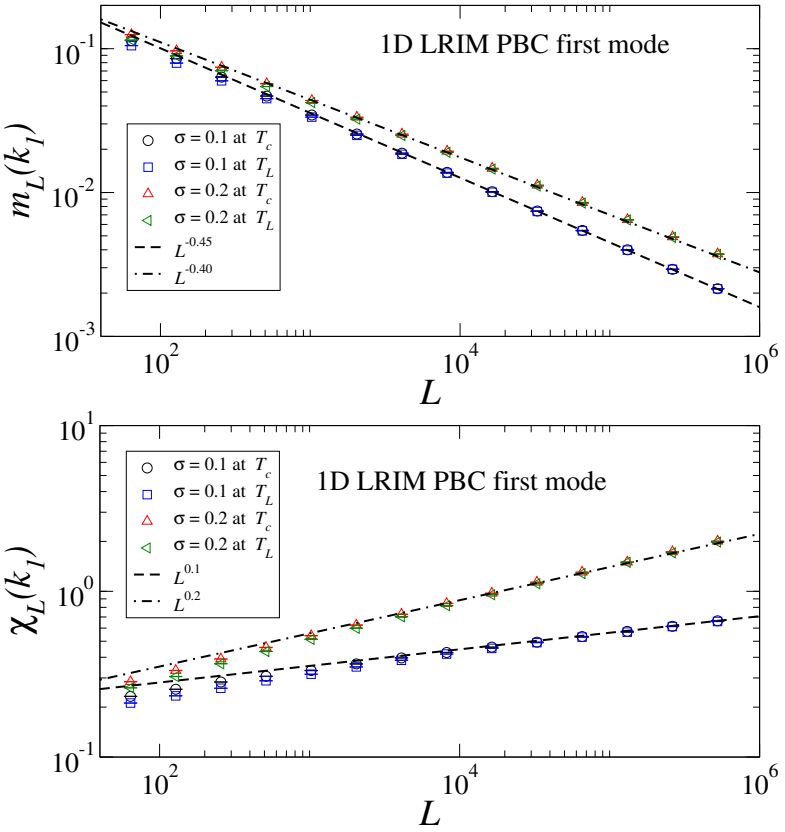

Figure 4.12: FSS in the magnetisation sector for non-zero modes for the 1D LRIM with PBCs. In the top image the first magnetisation mode clearly scales as $m_L^\dagger \sim L^{-(d-\sigma)/2}$. In the bottom image the first susceptibility mode clearly scales as $\chi_L^\dagger \sim L^\sigma$. Both manifestly are in favour of GFSS instead of the standard FSS.

4.3 Free boundary conditions

The Ising model with free boundaries above d_c is a widely studied problem, specially for the SRIM [11, 69] but it is not completely understood there.

One of the main issues with such boundaries is how to track the influence of the edges on the scaling of whole system. For the SRIM the particles in the edges have fewer interactions than those in the bulk. But for LRIM imposing FBCs does not affect the number of bonds, since all particles interact with all other.

Table 4.4: This table gathers the simulation results with PBCs for the magnetisation and susceptibility scaling exponents for the first non-zero mode. They should be compared GFSS predictions. The observables should follow: $m_L^\dagger \sim L^{-\beta^\dagger/\nu}$ and $\chi_L^\dagger \sim L^{\gamma/\nu}$

d	σ	T	$\beta^\dagger/\nu = (d-\sigma)/2$	$\gamma/\nu = \sigma$
1	0.1	T_c	0.448(2)	0.104(1)
		T_L	0.446(1)	0.108(1)
	0.2	T_c	0.396(1)	0.209(2)
		T_L	0.393(1)	0.213(1)
2	0.1	T_c	0.943(1)	0.113(2)
		T_L	0.940(2)	0.120(2)
	0.2	T_c	0.891(3)	0.216(2)
		T_L	0.889(1)	0.222(2)
3	0.1	T_c	1.438(5)	0.126(6)
		T_L	1.432(5)	0.140(6)
	0.3	T_c	1.333(6)	0.328(6)
		T_L	1.330(6)	0.347(6)
5	2.0	T_c	1.50(2)	2.01(5)
		T_L	1.50(2)	2.02(6)

The LRIM action for open boundaries is transformed to Fourier space through the sine transformation given by

$$F(\mathbf{k}) = \sum_{i=1}^{L} f(r_i) \prod_{\mu=1}^{d} \sin\left(k_\mu r_{i,\mu}\right) \tag{4.49}$$

where $k_\mu = \pi/(L+1)n_\mu$ with $n_\mu = 1, \ldots, L$. Its inverse transform is given by

$$f(\mathbf{r}) = \sum_{n=1}^{L} F(k_n) \prod_{\mu=1}^{d} \left(\sqrt{\frac{2}{L}} \sin\left(r_\mu k_{n,\mu}\right)\right. . \tag{4.50}$$

With this transformation the boundaries are successfully implemented because $F(n_0) = F(n_{L+1}) = 0$. In this context there are no zero mode, nevertheless we shall see then that the connection with DIVs will be through the parity of the modes.

With the sine transform, one can perform a perturbation expansion for the FBCs following the Rudnick-Gaspari-Privman steps in Ref. [82], and then the action

takes the form

$$S[\phi] = \frac{1}{2}\sum_{\mathbf{k}}\Big(r_0 + c|\mathbf{k}|^2 + c_\sigma|\mathbf{k}|^\sigma\Big)\phi_{\mathbf{k}}^2 - \left(\frac{8}{L}\right)^{\frac{d}{2}} h\sum_{\mathbf{k}\in Q}\phi_{\mathbf{k}}\prod_{j=1}^{d}\frac{1}{k_j} + \frac{u}{L^d}\sum_{\mathbf{k_1},\mathbf{k_2},\mathbf{k_3},\mathbf{k_4}}\Delta_{\mathbf{k_1},\mathbf{k_2},\mathbf{k_3},\mathbf{k_4}}\phi_{\mathbf{k_1}}\phi_{\mathbf{k_2}}\phi_{\mathbf{k_3}}\phi_{\mathbf{k_4}}, \tag{4.51}$$

where the Δ's are momentum conserving factors. In this case the DIVs for the self interaction term will affect the modes which couple to h, driven them by QFSS. The others, out of the influence for DIVs will follow GFSS. One can deliver the susceptibility from the integration of Gaussian model, after setting $h = 0$. There $|k|^\sigma$ term dominates over k^2, that allows us to neglect the term k^2, set $c = 0$ and to simplify $c_\sigma = 1$. In that sense

$$\chi = L^{-d}\frac{\partial^2}{\partial h^2}\ln\left(\int\left(\mathcal{D}\phi\; e^{-S[\phi]}\right)\right. \tag{4.52}$$

$$= \left(\frac{8}{L^2}\right)^d\sum_{\mathbf{k}\in Q}\left(\frac{1}{r_0 + |\mathbf{k}|^\sigma}\prod_{j=1}^{d}\frac{1}{k_j^2}\right). \tag{4.53}$$

Taking the limit at T_c, r_0 vanishes and then its behaviour is $\chi \sim L^\sigma$, that is independent of the parity of $\mathbf{k}$ and so not affected by DIVs. However, at pseudocritical point where the finite-size counterparts of phase transitions occur, i.e., inside of the scaling window, all the rest of the observables follow QFSS which includes DIVs. The FSS for T_c does not match since it is out of the scaling window. One can observe that in the upper image of Fig. 3.3.

4.3.1 Bulk definition for the SRIM and LRIM

For the 5D SRIM the nature of the interactions allow us to define a core. For 1D SRIM system with size L, only the particles at the extremities suffer the edge effect, and so the bulk contain $L_b = L - 2$ particles. So for the 5D SRIM $N_b = L_b^5 = (L-2)^5$ that in terms of proportion in $(1 - 2/L)^5$. Here we have

simulated lattices from $L = 8$ to $L = 48$, hence the proportion goes from 24% to 80% in the best case. That means that strong correction may come in the FSS. To reduce the problem we define the core has the $L_c = L/2$ that goes from the $L/4$ to $3L/4$ of the sites lattice. According to the core statistics one will also have m_{L_c} and χ_{L_c}.

The FBCs can lead to very strong corrections to the expected scaling behaviour. This feature is because the whole system is a mixture between the bulk scaling and the surface scaling. The SRIM specially suffers from this behaviour and one needs to separate and treat differently the scaling for the bulk and for the surface. However, the nature of the long-range interactions gives rise to a complex relation between the boundary terms and the bulk. In Fig. 4.13 we have plotted the magnetisation distribution $\mu(\mathbf{x})$ for 1D LRIM with PBCs and FBCs and at both T_L and T_c. There we can observe that for PBCs the behaviour is clear, up to fluctuation, all the spins take a thermal average of the thermal magnetisation. For FBCs the magnetisation depends on the lattice position but only at T_L, however at T_c the magnetisation take a very low value and the dependence seems to disappear. Since one can not determine a distance where the surface vanishes and when the bulk start we can reinforced from Fig. 4.14, where $\mu_{\mathbf{x}}$ has been plotted along $\mathbf{x}$ axis.

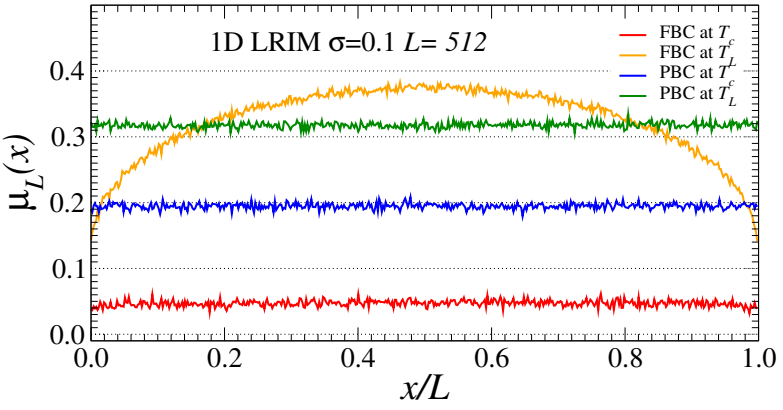

Figure 4.13: Comparison of the magnetisation profiles for the 1D LRIM with FBCs and PBCs at both T_L and T_c.

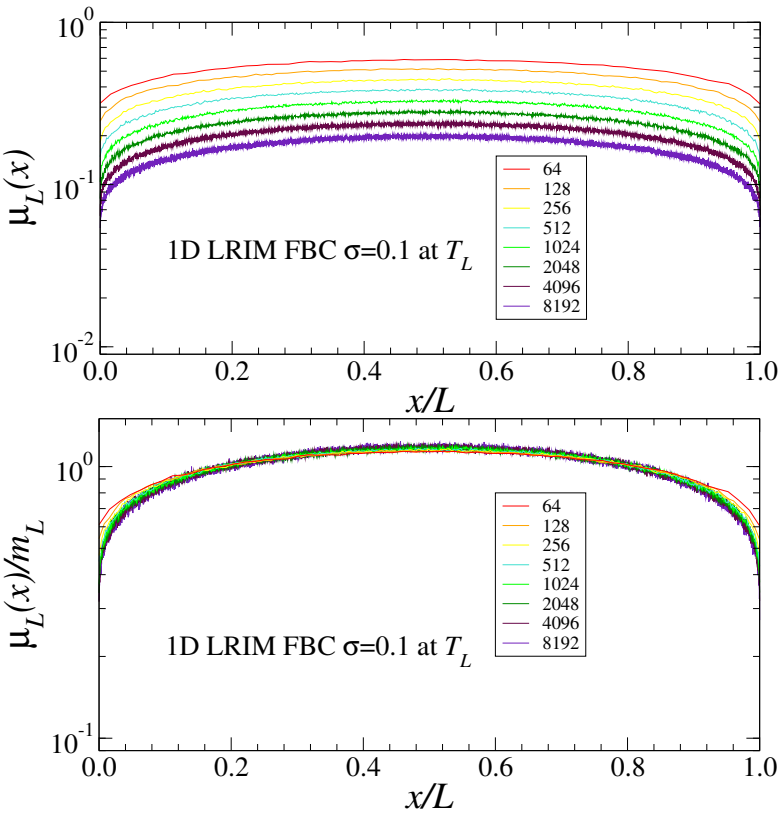

Figure 4.14: The bulk profile is plotted for 1D LRIM with FBCs at T_L. The top figure shows the magnetisation profile per spin $\mu_L(x)$. The bottom figure the rescaled profile over the total magnetisation $\mu_L(x)/m_L$ has been depicted showing the impossibility to define a bulk.

4.3.2 Shifting, rounding and heat capacity scaling

We perform a similar analysis to that carried out for systems with PBCs. We fit the shifting to the following function for the models with FBCs

$$T_c - T_L = z_0 L^{-\lambda}(1 + z_1 L^{-\omega}). \tag{4.54}$$

This expression is given in terms of the difference between the pseudocritical point for system with FBCs and the critical point computing from the PBCs analysis. For such boundaries we found that $\lambda = 1/\nu = \sigma$, and the first-order correction can not be considered as such since the fitting gives us the value $\omega \approx 0$. In Fig. 4.15 we plotted the shifting and the rounding for the 1D LRIM. Table 4.5 contains all

the numerical results for the critical point, shifting and rounding for several low-dimensionality LRIM and the 5D SRIM. The scaling relations at the pseudocritical point, as we see, are not influenced by DIVs. On the other hand the rounding is still controlled by them and so following QFSS, in contradiction with the standard FSS. In that sense, the rounding, or in other words, the scaling window converges to zero faster than the approach towards the critical point. We concluded that indeed the scaling relations are not given by the Landau mean-field exponents rather, they are given by the Gaussian FSS which implies $\lambda^{\dagger} = 1/\nu = \sigma$, both have the same prediction for the shift exponent though.

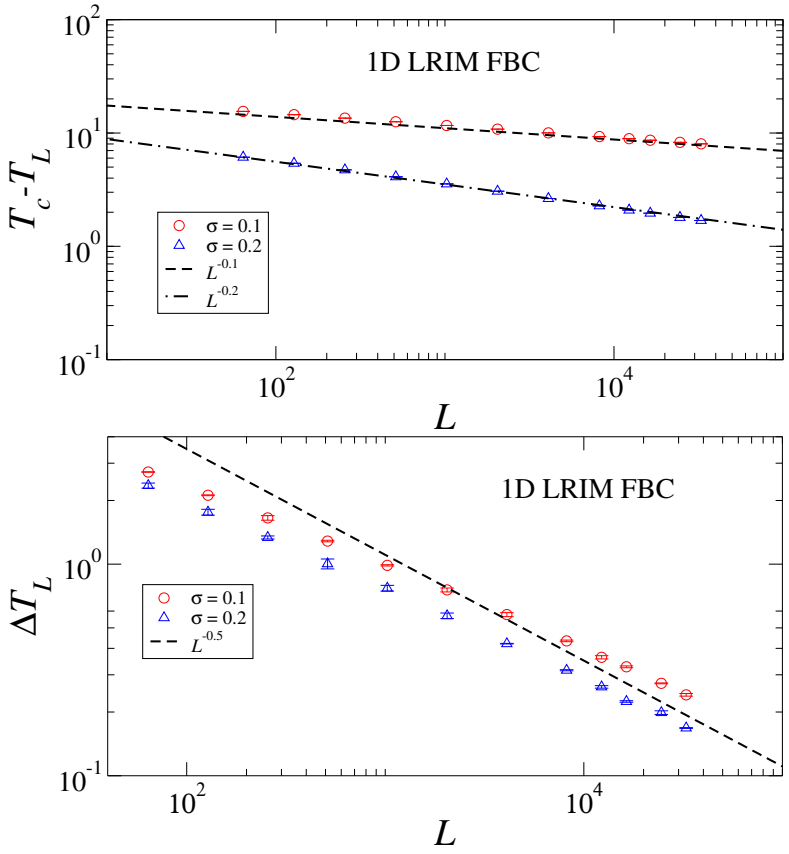

Figure 4.15: FSS for the shift and rounding exponents above d_c for the 1D LRIM with FBCs for two σ values 0.1 and 0.2. Top figure shows that the pseudocritical points T_L scale as $T_c - T_L \sim L^{-\sigma}$ following the dashed lines. The bottom figure shows the scaling for the rounding, both scaling approaching $\Delta T_L \sim L^{-1/2}$ denoted by the dashed line. GFSS takes over pseudocritical points and QFSS fits for the rounding.

Here, in the energy sector the things are not very clear because the singular part

Table 4.5: Results corresponding to the temperature sector for the LRIM. For different dimensions d and σ values. We have computed for the FBCs the shift and rounding exponent.

d	σ	T_c	$\lambda^\dagger = \sigma$	$\theta = d/2$
1	0.1	21.0013(3)	0.106(1)	0.43(1)
	0.2	10.8421(2)	0.209(2)	0.48(2)
2	0.1	65.3381(1)	0.107(1)	0.81(5)
	0.2	33.8384(1)	0.211(2)	0.83(4)
3	0.1	129.415(1)	0.102(1)	1.38(6)
	0.3	45.5543(1)	0.304(1)	1.40(7)
5	2.0	8.77847(1)	2.008(7)	2.38(6)

of the energy density is not properly fitting the predictions for such phenomena correctly. On one hand at T_L, the energy scaling should show a difference of scaling in the slopes given by the consideration of different σ values in the upper image of Fig. 4.16. However, in the lower plot corresponding to the heat capacity at T_L, the slopes go flat following the expected $\alpha = 0$. In contrast, the internal energy at T_c for the LRIM with PBCs is just flat as it is shown in Fig. 4.16. With this argumentation one can state that the flat slope shown by the capacity at T_c does not really show $\alpha = 0$, since scaling for the internal energy $e_L \sim L^{(1-\alpha)/\nu}$ is not satisfied.

4.3.3 Magnetization and susceptibility

The analysis of the magnetisation sector for systems with FBCs allows us to distinguish among QFSS, the Landau mean-field exponents with its derived FSS and Gaussian fixed-point exponents with GFSS at the critical point. For the magnetisation these three scaling manners are respectively given by $m_L \sim L^{-\beta/\nu} = L^{-d/4}$, $m_L \sim L^{-\beta/\nu} = L^{-\sigma/2}$ and $m_L^\dagger \sim L^{-\beta^\dagger/\nu} = L^{-(d-\sigma)/2}$. For the susceptibility they follow $\chi_L \sim L^{\gamma/\nu} = L^{d/2}$, $\chi_L \sim L^{\gamma/\nu} = L^\sigma$ and $\chi_L^\dagger \sim L^{-\gamma^\dagger/\nu} = L^\sigma$. In Fig. 4.17 we plotted the magnetisation and the susceptibility scaling behaviour for the 1D LRIM with FBCs with two values of $\sigma = 0.1$ and 0.2. The conclusion extracted for such figure is clear, QFSS predictions are valid at the pseudocritical point, i.e.,

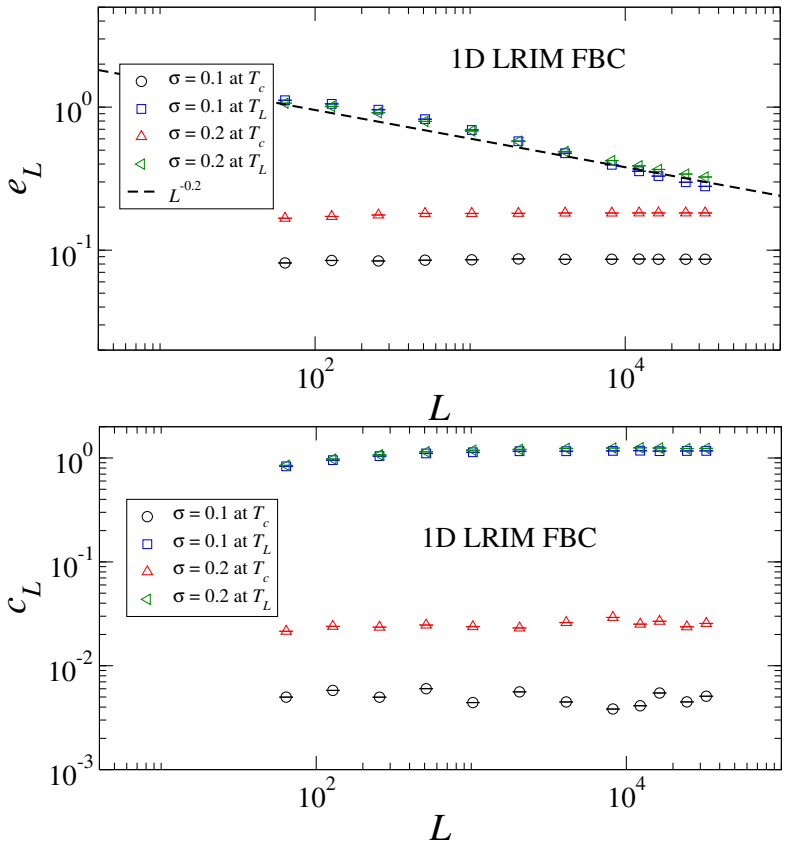

Figure 4.16: FSS for the internal energy and heat capacity in 1D LRIM with FBCs with two σ values 0.1 and 0.2. In the top image the energy scales close to $e_L \sim L^{-\sigma}$ for T_L and it clearly does not have any L dependence. Hence, the slopes for the heat capacity, in the bottom image, show no scaling dependence with L and deliver $\alpha = 0$.

inside of the scaling window. At the critical point, which is outside of the scaling windows, as $\gamma = \gamma^\dagger$ one can't distinguish which FSS is taking over, however the magnetisation is in favour of the GFSS. The estimation of the slopes for the other models such 2D and 3D LRIM and the 5D SRIM are written down in table 4.6. Despite in fact that Landau exponents were obtained for the susceptibility at the critical point for 5D SRIM with FBCs in Ref. [83–85], the conclusion delivered here is clear. The coincidence of the value $\gamma^\dagger = \gamma$ makes the susceptibility a bad quantity to distinguish standard FSS from GFSS. However, the magnetization scaling with $\beta^\dagger \neq \beta$ follows GFSS at the critical point as is shown in the tables and figures. Inside the scaling window, QFSS is the correct scheme, but outside, the influence of DIVs disappears and this invalidates the mean-field exponents in

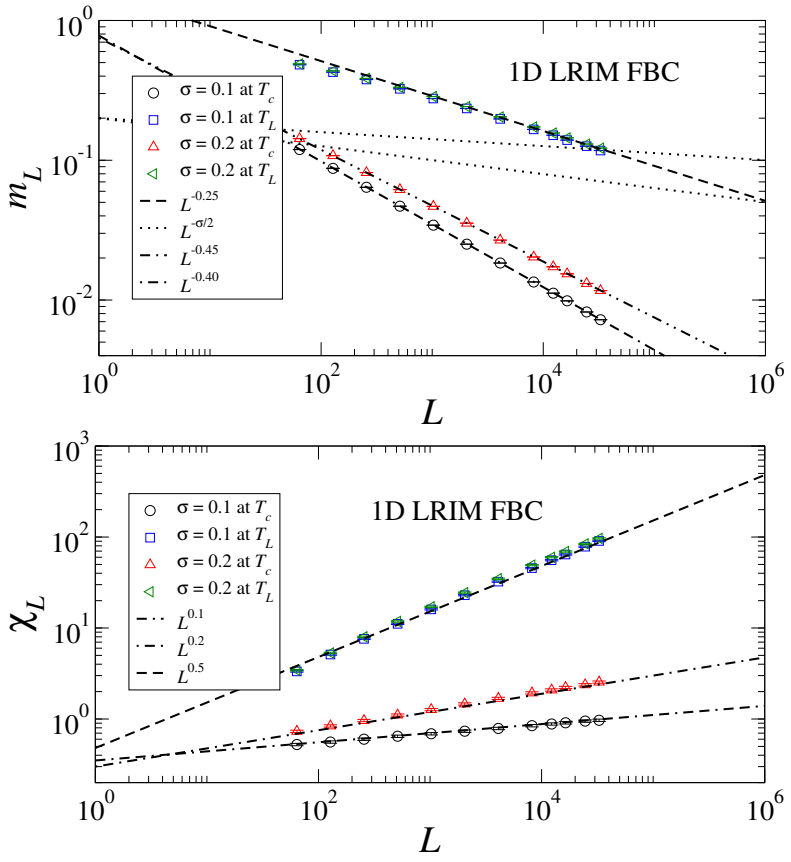

Figure 4.17: FSS for the magnetisation sector for the 1D LRIM with FBCs. In the top image the magnetisation clearly scales as $m_L \sim L^{-d/4}$ at T_L and $m_L^\dagger \sim L^{-(d-\sigma)/2}$ at T_c. In the bottom image the susceptibility clearly scales as $\chi_L \sim L^{d/2}$ at T_L and $\chi_L^\dagger \sim L^\sigma$ at T_c. These results are in favour of QFSS at T_L, and GFSS at T_c.

favour of GFSS.

4.3.4 Correlation function and correlation length

Here we use the Fourier transform for free boundary conditions in order to compute the correlation function and the correlation length. Hence, the correlation length can be estimated from [81]

$$\xi_L(t,h) = \frac{1}{2\sin(k_{\min}/2)}\left[\frac{\tilde{G}(k_1)}{\tilde{G}(k_2)} - 1\right]^{\frac{1}{\sigma}}. \tag{4.55}$$

Here, $k_{\min} = \pi/(L+1)$ is chosen to be the smallest wave vector for the open lattice.

Table 4.6: This table gathers some of the simulation results with FBCs for the scaling exponents and compared with QFSS and GFSS predictions. The observables should follow QFSS: $m_L \sim L^{-\wp\beta/\nu}$, $\chi_L \sim L^{\wp\gamma/\nu}$, $\xi_L \sim L^{\wp}$ and $G_L(L/2) \sim L^{-(d-2+\eta_\wp)}$; or GFSS: $m_L^\dagger \sim L^{-\beta^\dagger/\nu}$, $\chi_L^\dagger \sim L^{\gamma/\nu}$, $\xi_L^\dagger \sim L$ and $G_L^\dagger(L/2) \sim L^{-(d-2+\eta)}$. The $*$ symbol denotes that the observables were measured only in the core region.

d	σ	T	$\beta^\dagger/\nu = (d-\sigma)/2$	$\gamma/\nu = \sigma$	$\wp^\dagger = 1$	$d-2+\eta = d-\sigma$
			$\wp\beta/\nu = d/4$	$\wp\gamma/\nu = d/2$	$\wp = d/2\sigma$	$d-2+\eta_\wp = d/2$
1	0.1	T_c	0.450(4)	0.099(1)	1.01(3)	0.86(6)
		T_L	0.233(4)	0.522(3)	4.03(7)	0.487(5)
	0.2	T_c	0.401(3)	0.200(1)	1.03(2)	0.83(6)
		T_L	0.230(4)	0.225(5)	2.21(4)	0.483(6)
2	0.1	T_c	0.949(1)	0.094(2)	1.07(7)	2.07(9)
		T_L	0.501(1)	0.985(2)	7.48(4)	0.954(3)
	0.2	T_c	0.897(1)	0.198(2)	0.95(6)	1.70(9)
		T_L	0.494(1)	0.994(2)	3.97(4)	0.974(3)
3	0.1	T_c	1.446(2)	0.102(1)	0.92(6)	3.2(4)
		T_L	0.778(1)	1.408(2)	13.94(6)	1.55(2)
	0.3	T_c	1.371(2)	0.267(2)	0.94(6)	3.1(4)
		T_L	0.791(7)	1.388(2)	4.66(8)	1.54(3)
5	2.0	T_c	1.70(3)	1.67(6)	0.98(3)	3.3(1)
		T_L	1.65(6)	2.03(6)	1.19(6)	2.43(2)
	2.0*	T_c	1.57(3)	2.06(8)	-	-
		T_L	1.36(8)	2.51(2)	-	-

The analysis of the correlation sector for systems with FBCs does not allow us to distinguish between standard FSS and GFSS. Nevertheless, QFSS takes over the scaling window here too as expected. The overlap between standard FSS and GFSS can be shown as follows. For the correlation length both scaling are given by $\xi_L \sim L$, in the same line as $\eta = \eta^\dagger$ the correlation function at $r = L/2$ scales as $G(L/2) \sim L^{-(d-\sigma)}$. In Fig. 4.18 we plotted for both quantities their scaling behaviour for the 1D LRIM with FBCs with two values of $\sigma = 0.1$ and 0.2. The estimation of the slopes for the other models such 2D and 3D LRIM and the 5D SRIM are written down in table 4.6. Hence, these observables can't be used to observed the subtle scaling. On the other hand, the validity of QFSS at T_L is proven.

As we discuss in the PBCs, one observes different regimes between GFSS (we

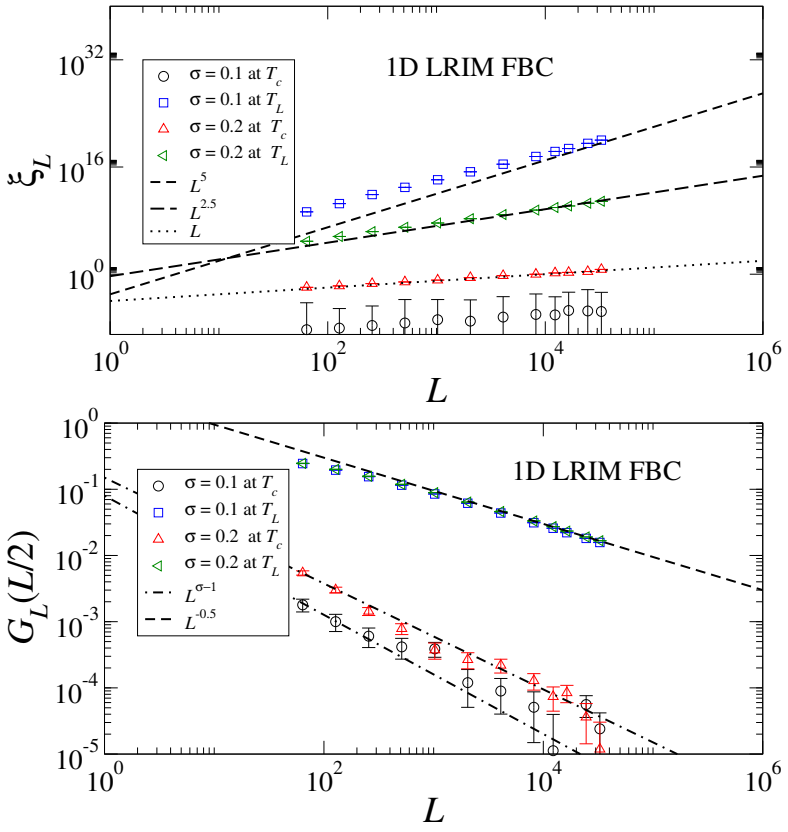

Figure 4.18: FSS for correlation sector for the 1D LRIM with FBCs. In the top image the correlation length scales close to $\xi_L \sim L^{\text{♀}}$ at T_L and $\xi_L^{\dagger} \sim L$ at T_c. In the bottom image the susceptibility clearly scales as $G_L(L/2) \sim L^{-d/2}$ at T_L and roughly $G_L^{\dagger}(L/2) \sim L^{\sigma-d}$ at T_c. These results manifestly are in favour of QFSS at T_L, and roughly GFSS at T_c.

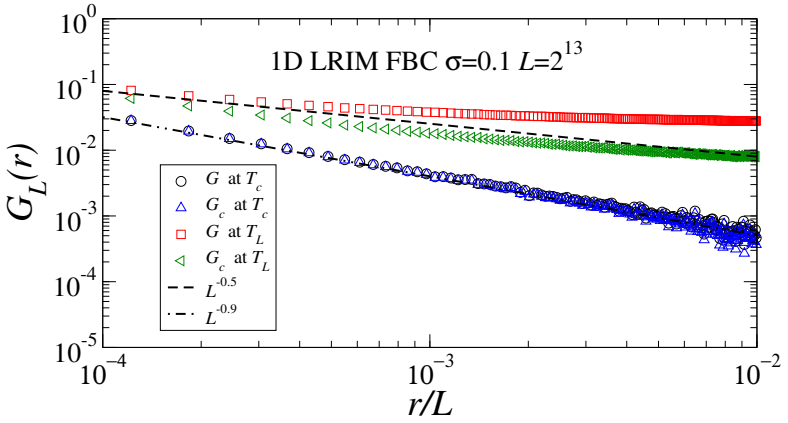

Figure 4.19: Correlation function in terms of distance for the 1D LRIM with FBCs. The dashed lines show QFSS and GFSS. For such small system with FBCs, one can observe QFSS at T_L rather than GFSS. For the scaling at T_c, GFSS seems to dominate in all the regime.

already discarded standard FSS) and QFSS independent if considering connected or unconnected correlation functions. For the FBCs one observes more subtle aspects. In fact, after the scaling at T_c is suspected as GFSS, one can speculate how G_c or G will look in such special boundaries. The answer is plotted in Fig. 4.19, at pseudocritical point some crossover with GFSS and QFSS is expected, but at T_c, out of the scaling windows the influence of DIVs disappears and one then expects a pure GSS behaviour that is shown in the figure. This result should be clearly seen in systems with larger sizes than those simulated here, $L = 2^{15}$, where the crossover is not specially clear. However, QFSS is not definitely expected at the critical point.

4.3.4.1 Fourier modes

The Fourier modes for the systems with FBCs are slightly more complicated than with PBCs. That is given by the sine transform, that couple the modes with DIVs in terms of the parity. The magnetisation modes are given for such boundaries by

$$m(\mathbf{k}) = \frac{1}{L^d}\left\langle \sum_i \prod_\nu S_i \sin(\mathbf{k}_\nu \mathbf{r}_{\mathbf{i},\nu}) \right\rangle \Bigg(\tag{4.56}$$

There are no zero modes for FBCs. Moreover, those modes with odd parity have a projection onto the real magnetisation and consequently follow QFSS. By contrast the even modes do not experience such a projection and the DIV dependence vanishes giving GFSS. Actually this is only true at T_L because for FBCs, T_c is out of the scaling window, and then the modes will follow GFSS independent of the parity.

The modes analysed here correspond to the two first modes, first odd modes allowed in the Fourier space with FBCs which contain all the elements of the vectors $k_1 = \pi/(L+1)$. They take $n_1 = 1$ for the 1D system, and $[1,1]$, $[1,1,1]$ and $[1,1,1,1,1]$ for 2D, 3D and 5D systems respectively. The first even mode

considered here is the one that takes a 2 in the first element of the vector. They are $n_2 = 2$ for 1D system, and $[2,1]$, $[2,1,1]$ and $[2,1,1,1,1]$ for the 2D, 3D and 5D systems respectively. The numerical results extracted from the simulations are gathered in Table 4.7. The plot in Fig. 4.20 shows the magnetization and susceptibility modes.

Again to get a non vanishing m_k for MC simulation, the thermal average is

$$|m(\mathbf{k})| = \frac{1}{L^d}\left\langle \left| \sum_i \left(\prod_\nu S_i \sin(\mathbf{k}_\nu \mathbf{r}_{\mathbf{i},\nu}) \right) \right| \right\rangle . \tag{4.57}$$

The susceptibility definition is not affected by that since $\chi_{\mathbf{k}} = L^d \langle |m_{\mathbf{k}}|^2 \rangle$. Regarding to the local spin magnetisation $\mu(\mathbf{x})$, one can also extract their related modes. In that particular case, the nonvanishing modes are only those that have the projection onto real magnetisation, the rest are just fluctuations around zero. This transformation is given by

$$\mu(\mathbf{k}) = \frac{1}{L^d} \sum_i \prod_\nu \mu(r_i) \sin(\mathbf{k}_\nu \mathbf{r}_{\mathbf{i},\nu}). \tag{4.58}$$

The comparison between the odd and even modes, for 1D LRIM with FBCs at T_L for systems size $L = 512$, are plotted in Fig. 4.21. One can observe that only the odd modes have a projection to the real magnetisation.

4.4 The LRIM with external magnetic field

To give more support to this project statement, the new scaling ansatz for the correlation length and its related ♀ exponent, we study the critical phenomena in terms of the external magnetic field scaling. The aim is to show that the correct picture above d_c compatible with RG is only given by QFSS in all the schemes. We also shows that the special case for FBCs at the critical point where DIVs are

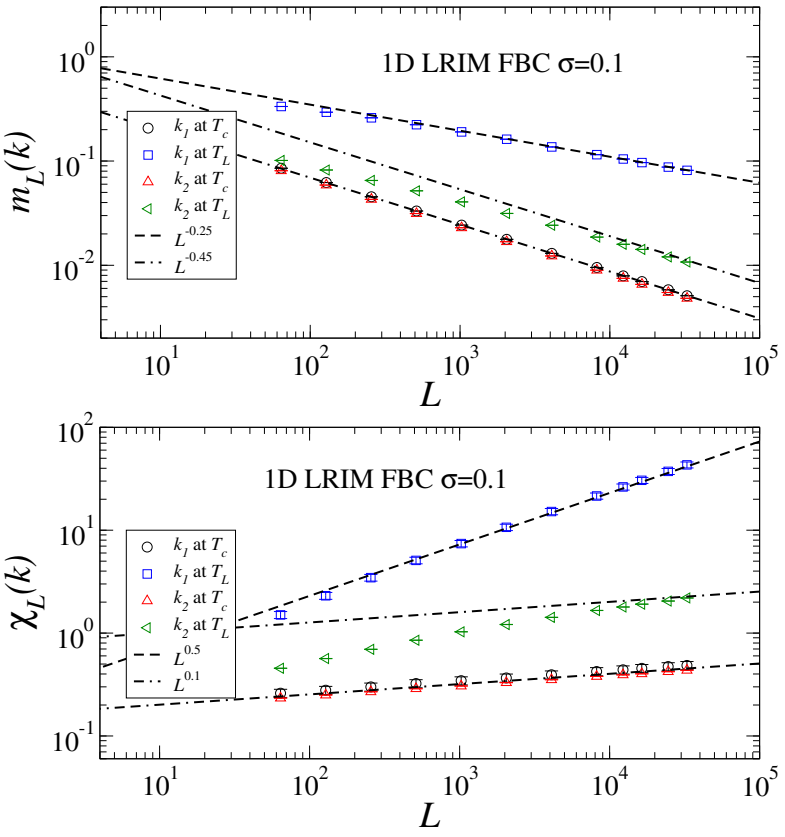

Figure 4.20: FSS for the magnetisation sector for two first modes for the 1D LRIM with FBCs. In the top image first magnetisation mode clearly scales as $m_L^{\dagger} \sim L^{-(d-\sigma)/2}$ and at T_L following $m_L \sim L^{-d/4}$ and the second modes scales at T_c and at T_L as GFSS. In the bottom image first susceptibility mode clearly scales as $\chi_L^{\dagger} \sim L^{\sigma}$ and at T_L following $\chi_L \sim L^{d/2}$ and the second modes scales at T_c and at T_L as GFSS too.

not expected, the FSS there is predicted by GFSS, in concordance with the result showed in Chapter 4 regarding to the non-zero modes. In this sense, one should able to distinguish, for example, the MF scaling for the magnetisation with $\delta = 3$ from the Gaussian with $\delta^{\dagger} = (d+\sigma)/(d-\sigma)$.

To simulate the LRIM with external megntic field h, we have used the update of the cluster-algorithm for the Fukui-Todo version that is explained in Chapter 3.

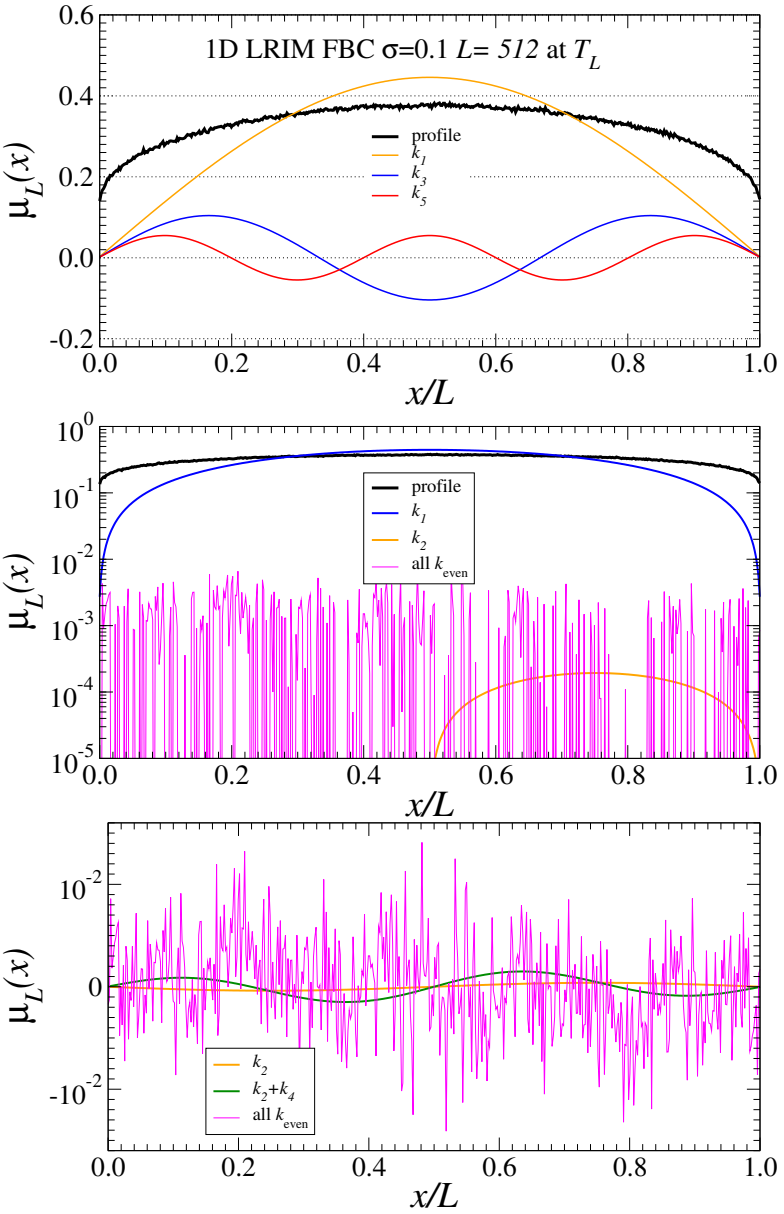

Figure 4.21: Profile for magnetisation for the 1D LRIM with FBCs. The top picture shows the contribution of the first three odd modes to the magnetisation profile. In the middle plot a log scale has been applied to y-axis in order to compare k_1 and k_2 modes. The bottom image shows the fluctuation around zero for such even modes whose projection do not contribute to the real magnetisation.

4.4.1 Scaling

In Chapter 3, we had ignored the scaling of the observables in terms of external magnetic field h, since we had focused on FSS without external field. However, we now consider the critical phenomena in terms of $h \neq 0$ at the critical point

Table 4.7: FSS for the first two modes for LRIM with FBCs for magnetisation and susceptibility. Odd modes k_1 follow QFSS and the even modes, GFSS.

			k_1		k_2	
d	σ	T	$\wp\beta/\nu = d/4$	$\wp\gamma/\nu = d/2$	$\beta^\dagger/\nu = (d-\sigma)/2$	$\gamma/\nu = \sigma$
1	0.1	T_c	0.453(2)	0.093(3)	0.449(4)	0.100(3)
		T_L	0.249(1)	0.501(7)	0.396(4)	0.206(4)
	0.2	T_c	0.401(3)	0.197(4)	0.403(4)	0.200(4)
		T_L	0.255(4)	0.491(5)	0.360(4)	0.273(4)
2	0.1	T_c	0.945(2)	0.08(1)	0.968(4)	0.06(1)
		T_L	0.547(2)	0.96(2)	0.809(4)	0.34(4)
	0.2	T_c	0.921(3)	0.17(2)	0.911(4)	0.17(2)
		T_L	0.525(1)	0.97(1)	0.953(4)	0.42(2)
3	0.1	T_c	1.446(2)	0.102(1)	1.51(4)	0.05(4)
		T_L	0.778(1)	1.408(2)	1.28(6)	1.40(5)
	0.3	T_c	1.371(2)	0.267(2)	1.45(5)	0.05(4)
		T_L	0.791(7)	1.388(2)	1.27(5)	1.45(5)
5	2.0	T_c	1.66(6)	1.67(6)	1.53(1)	2.00(3)
		T_L	1.64(6)	2.03(5)	1.60(5)	1.77(5)

$t = 0$. In the thermodynamic limit, the observables are given by the following scaling relations. For the energy sector the energy density and the heat capacity scale as

$$e_\infty(0,h) \sim h^\epsilon, \qquad c_\infty(0,h) \sim h^{-\alpha_c}. \tag{4.59}$$

The magnetic sector is given by

$$m_\infty(0,h) \sim h^{1/\delta}, \qquad \chi_\infty(0,h) \sim h^{1/\delta-1}. \tag{4.60}$$

Finally, the correlation length scales as

$$\xi_\infty(0,h) \sim h^{-\nu_c}. \tag{4.61}$$

These exponents are related with the others [86] by

$$\epsilon = 2 - \frac{(\gamma+1)}{\Delta}, \qquad \alpha_c = -2 + \frac{(\gamma+2)}{\Delta}, \qquad \nu_c = \frac{\nu}{\Delta}, \tag{4.62}$$

with the gap exponent $\Delta = \beta + \gamma$. These exponents can be found in Abe's publication in [87] (carefully noting the Abe's exponents $\Delta_{\text{Abe}} = 2\Delta$), in Suzuki's [80] or in the paper by Domb and Gaunt in [88].

In the MF regime for the LRIM one recalls the values of the exponents, $\gamma = 1$, $\beta = 1/2$, $\delta = 3$ and $\nu = 1/\sigma$. So the gap exponent $\Delta = 3/2$. Hence, the last exponents related to the critical phenomena for external field take the following values

$$\epsilon = \frac{2}{3}, \qquad \alpha_c = 0, \qquad \nu_c = \frac{2}{3\sigma}. \tag{4.63}$$

For the special case which is given by the Gaussian fixed point so that the scaling belongs to GFSS, the critical exponents are $\gamma = 1$, $\beta^\dagger = (d-\sigma)/2\sigma$, $\delta^\dagger = (d+\sigma)/(d-\sigma)$ and $\nu = 1/\sigma$. The corresponding gap exponent is $\Delta^\dagger = (d+\sigma)/2\sigma$. The exponents in Eq.(4.62) take the following values

$$\epsilon^\dagger = 2\frac{d-\sigma}{d+\sigma}, \qquad \alpha_c^\dagger = 2\frac{d-2\sigma}{d+\sigma}, \qquad \nu_c^\dagger = \frac{2}{d+\sigma}. \tag{4.64}$$

4.4.2 QFSS for PBCs and FBCs

To show all the possible scaling schemes, QFSS with DIVs and GFSS with non-DIVs, we recall the free energy densities. In terms of DIVs we write

$$f_L(t,h) = b^{-d} F_{L/b}\left(b^{y_t^*} t, b^{y_h^*} h\right), \tag{4.65}$$

with $y_t^* = d/2$ and $y_h^* = 3d/4$. The corresponding free energy in terms of non-DIVs for Gaussian scaling is

$$f_L^\dagger(t,h) = b^{-d} F_{L/b}^\dagger\left(b^{y_t} t, b^{y_h} h\right), \tag{4.66}$$

with $y_t = 1/\sigma$ and $y_h = (d+\sigma)/2$. We will follow this notation along this section to distinguish both type of scaling. We will see the finite-size effects are quite considerable in the behaviour of the observables in terms of h.

4.4.3 Energy and heat capacity

We are interested in the scaling of the internal energy that is obtained by differentiating the free energy with respect to t, and then setting $t = 0$ and replacing $b = h^{-1/y_h^*}$,

$$e_L(0,h) = h^{(d-y_t^*)/y_h^*} U_{L/b}\left(b^{y_h^*} h\right), \tag{4.67}$$

or with $b = h^{-1/y_h}$ for the Gaussian case

$$e_L^\dagger(0,h) = h^{(d-y_t)/y_h} U_{L/b}^\dagger\left(b^{y_h} h\right). \tag{4.68}$$

One finds respectively the scaling for both schemes in terms of h

$$e_L(0,h) \sim h^{(d-y_t^*)/y_h^*} = h^{2/3}, \tag{4.69}$$

$$e_L^\dagger(0,h) \sim h^{(d-y_t)/y_h} = h^{2(d-\sigma)/(d+\sigma)}. \tag{4.70}$$

in the sense that $b = L$. The internal energy scaling is plotted in Fig. 4.22 for the 1D LRIM with $\sigma = 0.1$ and $L = 8192$. The validity of QFSS at T_L and at T_c for systems with PBCs is clearly shown. This scheme is also contrasted with FBCs at T_L in concordance with the conclusions in the Chapter 4. The expected GFSS at T_c for those systems with FBCs is also corroborated. Similar analysis is done for the heat capacity

$$c_L(0,h) = h^{(d-2y_t^*)/y_h^*} C_{L/b}\left(b^{y_h^*} h\right), \tag{4.71}$$

$$c_L^\dagger(0,h) = h^{(d-2y_t)/y_h} C_{L/b}^\dagger\left(b^{y_h} h\right). \tag{4.72}$$

One finds respectively setting $b = L$,

$$c_L(0,h) \sim h^{(d-2y_t^*)/y_h^*} = h^0, \tag{4.73}$$

$$c_L^\dagger(0,h) \sim h^{(d-2y_t)/y_h} = h^{2(d-2\sigma)/(d+\sigma)}. \tag{4.74}$$

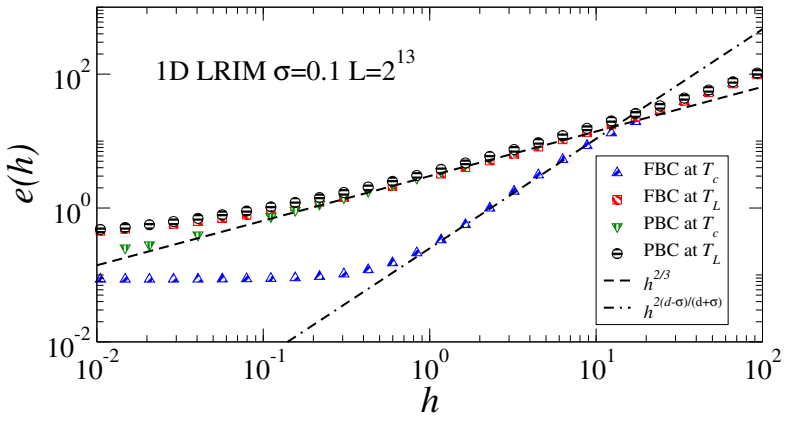

Figure 4.22: Internal energy scaling in terms of h for the 1D LRIM with $\sigma = 0.1$ for $L = 512$. With PBCs at T_L and T_c and also with FBCs at T_L the scaling observed $e \sim h^{2/3}$ is compatible with the QFSS. With FBCs at T_c the scaling observed is given by GFSS where $e^\dagger \sim h^{2(d-\sigma)/(d+\sigma)}$.

4.4.4 Magnetization and susceptibility

The scaling of the magnetisation and the susceptibility in terms of h also follows different scaling depending on the influence of DIVs. Their sets for both kind of scaling, with the same setting up as the internal energy, are given by

$$m_L(0,h) = h^{(d-y_h^*)/y_h^*}\mathcal{M}_{L/b}\left(b^{y_h^*}h\right), \tag{4.75}$$

$$m_L^\dagger(0,h) = h^{(d-y_h)/y_h}\mathcal{M}_{L/b}^\dagger\left(b^{y_h}h\right), \tag{4.76}$$

$$\chi_L(0,h) = h^{(d-2y_h^*)/y_h^*}\mathcal{X}_{L/b}\left(b^{y_h^*}h\right), \tag{4.77}$$

$$\chi_L^\dagger(0,h) = h^{(d-2y_h)/y_h}\mathcal{X}_{L/b}^\dagger\left(b^{y_h}h\right). \tag{4.78}$$

One respectively finds setting $b = L$,

$$m_L(0,h) \sim h^{(d-y_h^*)/y_h^*} = h^{1/3}, \tag{4.79}$$

$$m_L^\dagger(0,h) \sim h^{(d-y_h)/y_h} = h^{(d-\sigma)/(d+\sigma)}, \tag{4.80}$$

$$\chi_L(0,h) \sim h^{(d-2y_h^*)/y_h^*} = h^{-2/3}, \tag{4.81}$$

$$\chi_L^\dagger(0,h) \sim h^{(d-2y_h)/y_h} = h^{-2\sigma/(d+\sigma)}. \tag{4.82}$$

These scaling predictions are supported by the plots in Fig. 4.23.

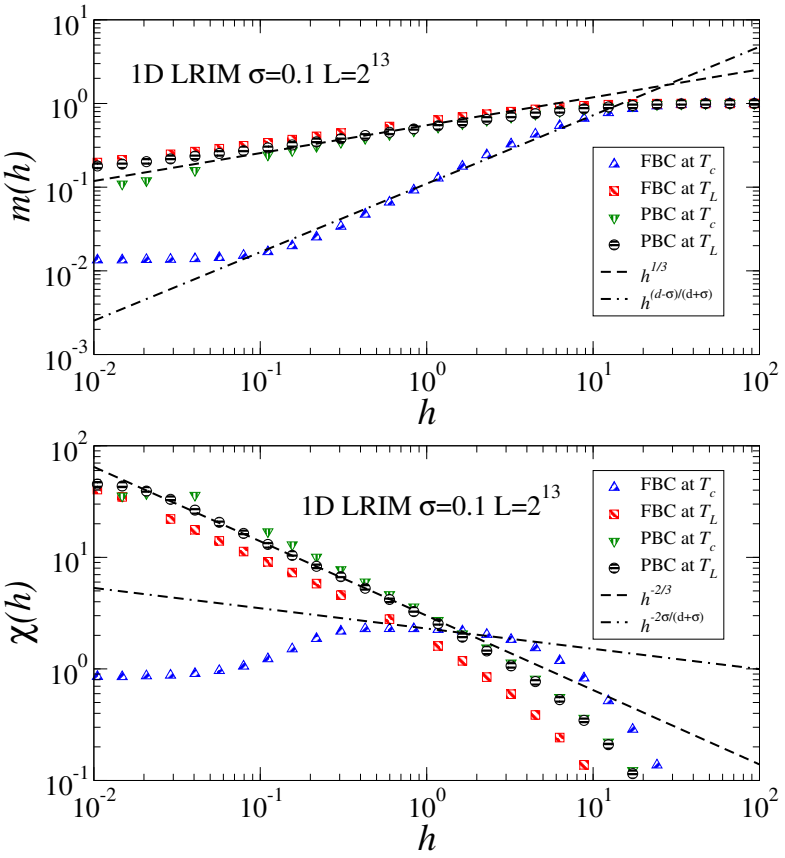

Figure 4.23: Magnetization ans susceptibility scaling in terms of h for the 1D LRIM with $\sigma = 0.1$ for $L = 512$. With PBCs at T_L and T_c and also with FBCs at T_L the scaling observed $m_L \sim h^{1/3}$ and $\chi_L \sim h^{-2/3}$ are compatible with the QFSS. With FBCs at T_c the scaling observed is given by GFSS where $m_L^\dagger \sim h^{(d-\sigma)/(d+\sigma)}$ and $\chi_L^\dagger \sim h^{-2\sigma/(d+\sigma)}$.

4.5 Conclusion

As the core of this thesis, this chapter contains the more relevant results from the study of the finite-size scaling above d_c. We have analysed in detail the long-range interacting ferromagnetic Ising model for the one, two and three dimensional systems with $\sigma < d/2$, and together with the 5 dimensional Ising model with nearest-neighbour interactions denoted as SRIM with $\sigma = 2$. Both of these systems were also analysed with two kind the boundary conditions, PBC and FBCs. Thereby for the PBCs, where the system is close to the thermodynamic limit, every scaling law is rather clear and undoubtedly in favour of the modified finite-size scaling. Instead, when the FBCs were imposed, far away from the thermodynamic limit not everything seems to satisfy the finite-size scaling theory or either the normalisation group theory. In fact in this chapter we have shown how the non-zero modes, in principle not very relevant, can actually explain the finite-size scaling at the critical point for systems with FBCs which follow the Gaussian scaling laws. So that supports the QFSS where above the upper critical dimension there are no ambiguity since when QFSS is absent we can not recover FSS with Landau exponent. We recover Gaussian scaling instead. Clearly supporting the modified finite-size scaling, where the fundamental new features arising from the fact that the dangerous irrelevant variable affects with no doubts the correlation sector. Hence, the pseudocritical exponent $\wp = d/d_c$ for the scaling behaviour of the correlation length, $\xi \sim L^{\wp}$ is claimed as universal. Its new companion for the anomalous dimension exponent, $\eta_{\wp}$ solves the puzzle of the negative anomalous dimension for the 5D Ising model. Then they should contribute to understanding of such phenomena in a simple and clear way by replacing standard finite-size scaling. The resultant picture for the modes is gather in table 4.8, which divided the Fourier modes into dangerous and non-dangerous sectors.

Finally, the inclusion of the external magnetic field in the analysis of the LRIM

Table 4.8: The partitioning of Fourier modes into dangerous ($\mathcal{Q}$) and non-dangerous ($\mathcal{G}$) sectors of the model.

	PBCs		**FBCs**	
	$k = \frac{2\pi}{L}(n_1, \ldots, n_d)$		$k = \frac{\pi}{L+1}(n_1, \ldots, n_d)$	
	$\mathcal{Q}$ (DIVs): All $n_\alpha = 0$	$\mathcal{G}$ (Non-DIVs): Any $n_\alpha \neq 0$	$\mathcal{Q}$ (DIVs): All n_α odd	$\mathcal{G}$ (Non-DIVs): Any n_α even
FSS at T_L	$m \sim L^{-\frac{d}{4}}$ $\chi \sim L^{\frac{d}{2}}$	$m \sim L^{-\frac{d-\sigma}{2}}$ $\chi \sim L^{\sigma}$	$m \sim L^{-\frac{d}{4}}$ $\chi \sim L^{\frac{d}{2}}$	$m \sim L^{-\frac{d-\sigma}{2}}$ $\chi \sim L^{\sigma}$
FSS at T_c	$m \sim L^{-\frac{d}{4}}$ $\chi \sim L^{\frac{d}{2}}$	$m \sim L^{-\frac{d-\sigma}{2}}$ $\chi \sim L^{\sigma}$	$m \sim L^{-\frac{d-\sigma}{2}}$ $\chi \sim L^{\sigma}$	$m \sim L^{-\frac{d-\sigma}{2}}$ $\chi \sim L^{\sigma}$

allowed us to restate the validity of the QFSS for systems with PBCs and the description at pseudocritical points for those with FBCs above the d_c. On the other hand, the expected GFSS predictions for systems with FBCs at the critical point is also shown. This illustrated the validity of the replacement of standard FSS by the combination of QFSS and GFSS.

Chapter 5

Partition function zeros of the LRIM

5.1 Introduction

This chapter complements the analysis for the LRIM above d_c carried out in Chapter 4, by studying FSS of the partition function zeros in order to give stronger support to QFSS. An alternative approach to the study of critical phenomena is to perform an analysis of the zeros of the partition function. As mentioned in Chapter 2, the 'fundamental theory of phase transitions' is the basis for the description of the scaling behaviour of the zeros which approach the real axis at the critical point in the thermodynamic limit.

The main idea behind this approach is that the zeros of the partition function lie in the complex plane of a parameter entering the partition function (i.e., temperature or external field). The first to develop this theory were Lee and Yang [12, 13], who studied the ferromagnetic case by looking at the partition function as a polynomial in terms the of external magnetic field. Following a similar idea, Fisher focused on the study of the zeros for the temperature complex plane [15]. Many studies

have since been carried out in this topic. For example, an investigation for Fisher zeros in the mean-field region can be found in Ref. [89] and for gauge models in Ref. [90].

The partition function $Z_L = \sum_{\{s_i\}} e^{-\beta \mathcal{H}[s_i]}$ is defined in real space. It can be re-expressed in terms of energy and total magnetisation

$$Z_L = \sum_{E,M} p(E,M) e^{-\beta E + hM}, \tag{5.1}$$

where $p(E,M)$ is the density of states. If one relaxes the demand that $\beta, h \in \mathbb{R}$ by extending them to the complex plane, i.e. $\beta, h \in \mathbb{C}$, for finite-size systems the partition function vanishes for specific values of β and h. These vanishings represent the roots of the partition function and are called zeros. Hence one can express the partition function in terms of the set of Fisher or Lee-Yang zeros, respectively $\{z_j\}$ and $\{h_j\}$,

$$Z_L(z) = A_z(Z) \prod_j (z - z_j(L)), \qquad Z_L(h) = A_h(Z) \prod_j (h - h_j(L)), \tag{5.2}$$

where $A_z(z)$ and $A_h(z)$ denote non vanishing smooth functions. From the first factorised representation for complex variables the free energy in terms of Fisher zeros is given by

$$f_L(z) = L^{-d} \ln A_z(z) + L^{-d} \sum_j \ln(z - z_j(L)). \tag{5.3}$$

Analogously the expression in terms of Lee-Yang zeros is obtained replacing z_j by h_j. The first term of the last equation contributes to the non-singular part of the energy. Singular behaviour is associated with the second term. The zeros z_j approach the critical point in the real axis with a angle ϕ. In principle, one expects that the number of zeros depends on the system size. Differentiating twice the

singular part of the free energy with respect to t one obtains the heat capacity,

$$c_L = L^{-d} \sum_j (z - z_j(L))^{-2}. \tag{5.4}$$

On the other and, differentiating the free energy twice with respect to h one obtains the expression for the susceptibility,

$$\chi_L = L^{-d} \sum_j (h - h_j(L))^{-2}. \tag{5.5}$$

This chapter is divided in two main sections and the conclusion. The Section 2 contains the QFSS analysis of the Fisher zeros. In section 3 we analyse the QFSS of the Lee-Yang zeros. Finally, section 4 contains the conclusion.

5.2 Fisher zeros

To derive QFSS for Fisher zeros we use Abe's prescription presented in Ref. [87]. Let

$$z_j = z_c + r_j e^{i\phi_j}, \tag{5.6}$$

where z_c is the critical point, r_j is the distance to the jth zero and ϕ_j the angle between them. If this notation is introduced in Eq.(5.4), the heat capacity is expressed as

$$c_L = L^{-d} \sum_j (r_j e^{i\phi_j})^{-2}. \tag{5.7}$$

Assuming that the main contribution is given by the lowest zeros, one obtains [91] $c_L \simeq L^{-d} r_1^{-2}$. Isolating r_1, and introducing QFSS for the heat capacity $c_L \sim L^{-\wp\alpha/\nu}$,

$$r_1^2(L) \sim L^{\wp\alpha/\nu - d}. \tag{5.8}$$

From the hyperscaling relation $\nu d/\wp = 2 - \alpha$, one then finds that the QFSS for r_1 is given by

$$r_1(L) \sim L^{-\wp/\nu}. \tag{5.9}$$

The prediction of the scaling for Fisher zeros in terms of GFSS is

$$r_1(L) \sim L^{-1/\nu}. \tag{5.10}$$

5.2.1 Numerical determination of Fisher zeros

The numerical determination of the positions of the Fisher zeros is carried out using a reweighting technique. The data for this method is given by a MC simulation. In this case, one can't efficiently use the Fukui-Todo update because the exact energy per sample is required. One can't use the activated bonds to extrapolate the energy and rather as one needs to compute the exact value of the energy that has a $\mathcal{O}(N)$ runtime. Consequently it reduces the maximum system sizes achievable to $L = 2^{14}$.

The methodology, following the guides from Ref. [92], is as follows: one considers the partition function in Eq.(5.1) with $H = 0$, and extends the inverse temperature in the complex plane, $\beta = \eta + i\xi$. The partition function takes the form of

$$Z(\beta) = \sum_E p(E,\beta) e^{-(\eta + i\xi)E} = \sum_E p(E,\beta) e^{-\eta E} \left(\cos[\xi E] - i \sin[\xi E]\right), \tag{5.11}$$

where $p(E,\beta)$ is the density of states. One defines a normalised version for last equation by $R(\eta,\xi) = Z(\beta)/Z[\mathrm{Re}(\beta)]$. Explicitly this is

$$\begin{aligned} R(\eta,\xi) &= \frac{\sum_E p(E,\beta) e^{-\eta E} (\cos[\xi E] - i \sin[\xi E])}{\sum_E p(E,\beta) e^{-\eta E}} \\ &= \langle \cos[\xi E] \rangle_\eta - i \langle \sin[\xi E] \rangle_\eta. \end{aligned} \tag{5.12}$$

where $\langle \ldots \rangle_\eta$ is the thermal average given by η. The first Fisher zero, for example, is expected to appear close to the pseudocritical point and one then has to perform MC simulation at $\beta_L = 1/T_L$, constructing its related $p(E, \beta_L)$. For this zero or in general, to locate the zeros, one considers the points that make $\langle \cos[\xi E] \rangle_\eta$ and $\langle \sin[\xi E] \rangle_\eta$ vanish, their overlap satisfies $R(\eta, \xi) = 0$ delivering the estimation of the position of the zero. There are two ways to extract the zeros, one is identifying then graphically. In Fig. 5.1 we can observe the vanishing point for both cosine and sine parts depicted by red and green points respectively. This methodology depends on size of the grid considered; big grid sizes deliver large errors and small grid sizes deliver, on the other hand, a costly runtime. The precision also is related in the manner that one constructs the density of states, that works with finite precision depending on the MC samples taken or adding a binning error if one decides to use histograms. Despite these sources of errors, the graphical search of zeros is a very useful technique as a first approach. To get better precision, the second methodology employed the AMOEBA search algorithm [93], a searching technique to find zeros in a 2D plane.

The typical picture for the zeros is given by the upper plot in Fig. 5.1, where MC simulations were used to identify the first zeros of the 5D SRIM. Here, we also use the same procedure to find the zeros for the LRIM. The results of the plots for LRIM surprisingly look slightly different above the critical temperature from those from the SRIM. To show that indeed this different form is also correct, we have computed all the possible states for very small system size, the usual picture then takes the form of the lower plot in Fig. 5.1 above d_c for LRIM. This difference is due to the large amount of the energy configuration that a LRIM can take for the similar spin configuration, even manifesting the possibility to take positive values of the energy in some spin configurations.

We are interested in the scaling of those zeros. There are two ways to represent the Fisher zeros, implicitly in the β-complex plane referenced in plots as Fig. 5.1

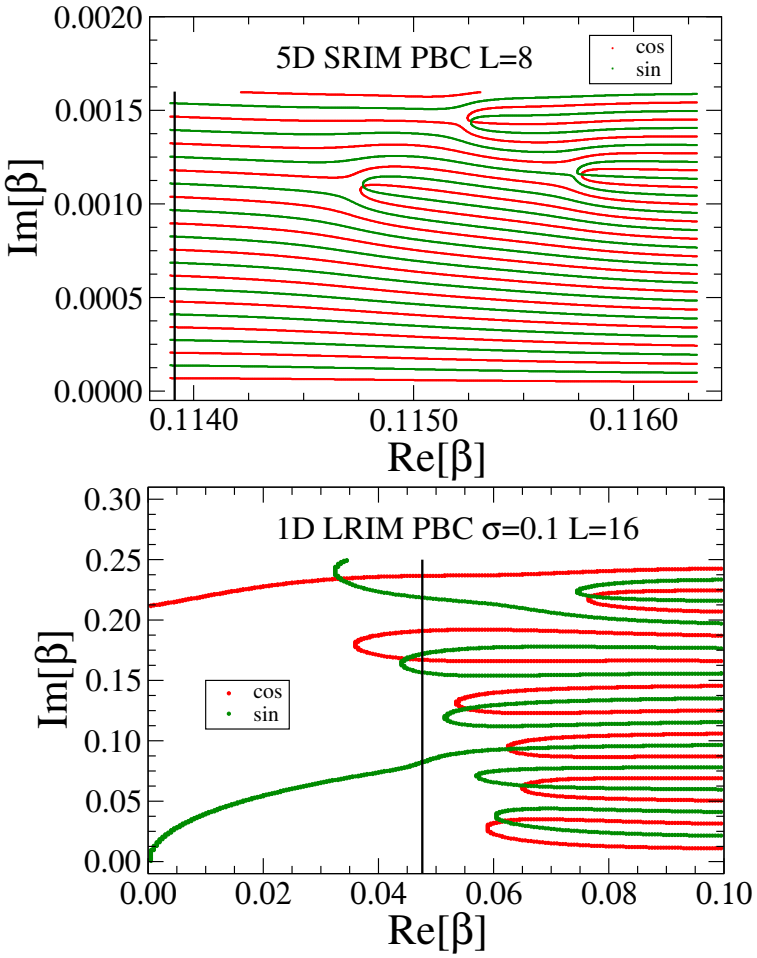

Figure 5.1: The upper image shows the graphical scan of Fisher zeros for 5D SRIM from a MC simulation. The lower image shows the graphical scan for 1D LRIM from an exact small system size

or explicitly in terms of partition-function zeros z (see Eq.(5.2)). We consider $z_j = \exp(-\beta_j)$, where the j is the position of the Fisher zero. In this manner, to find the FSS for the zeros one is interested in the scaling of the real and imaginary parts, respectively

$$\mathrm{Re}(z_j) = \exp(-\eta_j)\cos(\xi_j) \tag{5.13}$$

$$\mathrm{Im}(z_j) = \exp(-\eta_j)\sin(\xi_j). \tag{5.14}$$

The modulus is of these variables is $z_j = \exp(-\eta_j)$ and the critical value is given by $z_c = \exp(-\beta_c)$. The interested FSS is exactly through the scaling behaviour of $|\mathrm{Re}(z_j) - z_c|$ and $\mathrm{Im}(z_j)$. They are plotted for 1D LRIM for $\sigma = 0.1$ for

PBCs and FBCs in Fig. 5.2. The upper image can be related to the shift since $|\mathrm{Re}(z_j) - z_c| \sim L^{-d/2}$ for PBCs and $|\mathrm{Re}(z_j) - z_c| \sim L^{-\sigma}$ for FBCs. On the other hand, the imaginary part scales as $\mathrm{Im}(z_j) \sim L^{-d/2}$, independently of the boundary conditions.

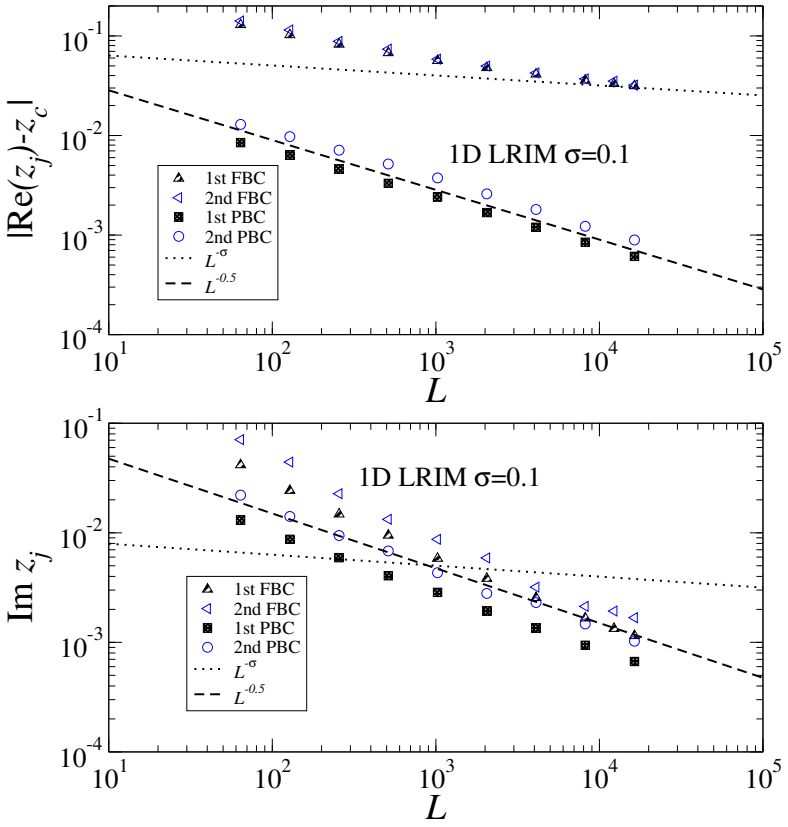

Figure 5.2: FSS for the first and second Fisher zeros for 1D LRIM with PBCs and FBCs for $\sigma = 0.1$ in terms of $|\mathrm{Re}(z_j) - z_c|$ and $\mathrm{Im}(z_j)$.

5.2.2 Impact angles

The impact angles can be given either in terms of z or β. Here we shall follow the notation given from Gordillo et *al* in [92]. For those in the β-plane:

- $\phi_{j,c}(z)$: angle between z_c-jth zero line and the z-axis.
- $\phi_{1,2}(z)$: angle between z_1-z_2 line, and the z-axis.
- $\phi_{j,c}(\beta)$: angle between line β_c-jth zero and the β-axis.

► $\phi_{1,2}(\beta)$: angle between β_1-β_2 line and the β-axis.

The results for the 1D LRIM for $\sigma = 0.1$ with PBCs and FBCs are plotted in Fig. 5.3. There, one can observe the scaling of the angles defined before such $\phi_{1,c}$, $\phi_{2,c}$ and $\phi_{1,2}$ for z and β variables. Meanwhile the impact angle for the system with PBCs approaches angles close to 45°, for FBCs the angles converge to zero.

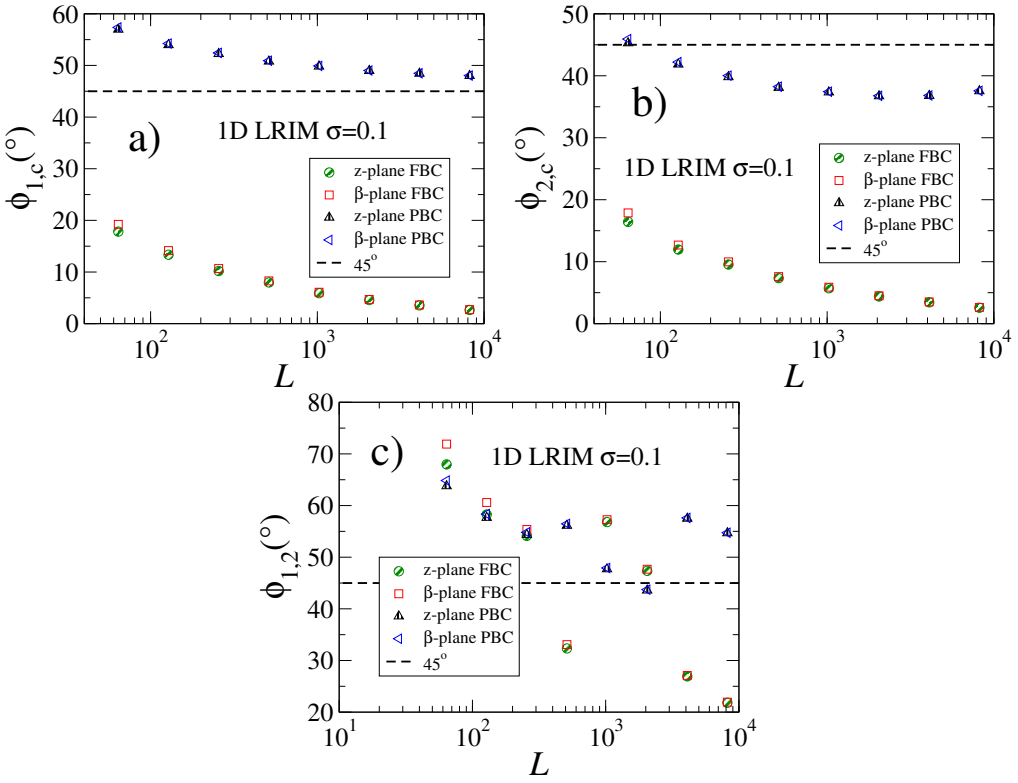

Figure 5.3: The plot in panel a) and b) show the impact angle in terms of system size for the first and second zeros respectively. The plot in panel c) shows the angle between the first and second zeros. For the system with PBCs the set of the first zeros appears to approach an angle of 45°. For systems with FBCs, the impact angle for the first and second zeros appears to vanish. The impact angle between the first and second zeros is more unstable, but the tendency is clear, for PBCs the angles seem to converge to some value around 45° and for FBCs the angles tends to zero.

There is not a complete FSS theory for the impact angles of Fisher zeros. Nevertheless, they can be linked with the shift, ν and ♀ exponents above d_c. The angle is expected to scale following the ratio of the imaginary and real part of the

lowest-laying zero [92],

$$\tan\phi \approx \frac{\mathrm{Im}z_1}{|\mathrm{Re}(z_1) - z_c|} \propto \frac{L^{-\wp/\nu}}{L^{-\lambda}} \sim CL^{\lambda-\wp/\nu} + \dots . \tag{5.15}$$

With this prescription and comparing Fig. 5.2 with those results in Fig. 5.3 we concluded that the impact angles, similarly to the shifting exponent, depend on boundary conditions. Whereas $\mathrm{Im}z_1$ is located very close to T_L, i.e., inside the QFSS window, the term $\mathrm{Re}(z_1)$ is far away from T_c for systems with FBCs and consequently, outside of the scaling window and the influence of DIVS. The impact angles for PBCs should approach $\pi/4$ since $\lambda = \wp/\nu$ leading $\tan\phi \sim C$, whereas for the systems with FBCs $\lambda^{\dagger} = 1/\nu < \wp/\nu$ and its impact angles should converge to zero since $\tan\phi \sim 0$. These results are compatible with the simulation results plotted in Fig. 5.3.

5.3 Lee-Yang zeros

We now proceed to study the complex h-plane zeros corresponding to the external magnetic field, changing consequently the notation from z to h in Eq.(5.2). In the thermodynamic limit close to the critical point these Lee-Yang zeros terminate at the so-called Lee-Yang edge, which scales as $h_{\mathrm{edge}}(t) \sim t^{\Delta}$, where the gap exponent $\Delta = \beta\delta = 3/2$ in mean-field regime. For finite systems the zeros form a discrete set distributed on the imaginary-h axis. They are labelled as $h_j(L,t)$ where j is an integer that records the closeness to the real-h axis so that.

To obtain the FSS for the Lee-Yang zeros one recalls Eq.(5.5) and follows the same argumentation made for the Fisher zeros. The susceptibility is given by the scaling of the first zero [91]

$$\chi_L \simeq L^{-d} h_1^{-2}. \tag{5.16}$$

We isolate h_1, and introducing the QFSS for the susceptibility $\chi_L \sim L^{-\wp\alpha/\nu}$

$$h_1^2(L) \sim L^{-(\wp\gamma/\nu+d)}. \tag{5.17}$$

Using the hyperscaling and Rushbrooke relation together $\nu d/\wp = 2\beta + \gamma$ and the relation for the gap $\Delta = \beta + \gamma$, one finds that the QFSS for h_1 is given by

$$h_1(L) \sim L^{-\wp\Delta/\nu} = L^{-3d/4}. \tag{5.18}$$

Otherwise, considering the GFSS picture, the zeros behaves as

$$h_1(L) \sim L^{-\Delta/\nu} = L^{-3\sigma/2}. \tag{5.19}$$

We have seen that the inclusion of DIVs breakdown of the standard FSS. This also includes the scaling of the Lee-Yang zeros. This was also shown for the 5D SRIM in [11].

5.3.1 Numerical determination of Lee-Yang zeros

With these considerations, the interest here is to see how the Lee-Yang zeros scale when approaching the real axis in terms of system size. To achieve that, we use reweighting method in the Eq.(5.1) using the complex external magnetic field as $h = h_r + ih_i$. In that sense, the normalized partition function is given by $R(\beta, h) = Z_L(\beta, h)/Z_L(\beta, h_r)$. All the cases considered here obey the Lee-Yang theorem and hence the zeros in h-plane are pure imaginary. This is translated to an impact angle of $\pi/2$. In conclusion, one can set $h_r = 0$ and only consider variation in h_i. Then

$$\begin{aligned} R(\beta, h_i) &= \frac{\sum_{E,M} p(E,M)e^{-\beta E}(\cos(h_i M) + i\sin(h_i M))}{Z_L(\beta, 0)} \\ &= \langle\cos(h_i M)\rangle + i\langle\sin(h_i M)\rangle \end{aligned} \tag{5.20}$$

where the sine term can be neglected because of parity $\langle \sin(h_i M) \rangle = 0$. Hence, one just finds the Lee-Yang zeros when the cosine terms vanishes. In Fig. 5.4 one observes the FSS at T_L and T_c for the first two zeros h_1 and h_2 for the 1D and 2D LRIM with PBCs and FBCs, with $\sigma = 0.1$ for both systems. The scaling showed is clearly in favour of QFSS, where the predicted scaling is $h_{1,2} \sim L^{-3d/4}$, over of the standard Landau which predicts $h_{1,2} \sim L^{-3\sigma/2}$.

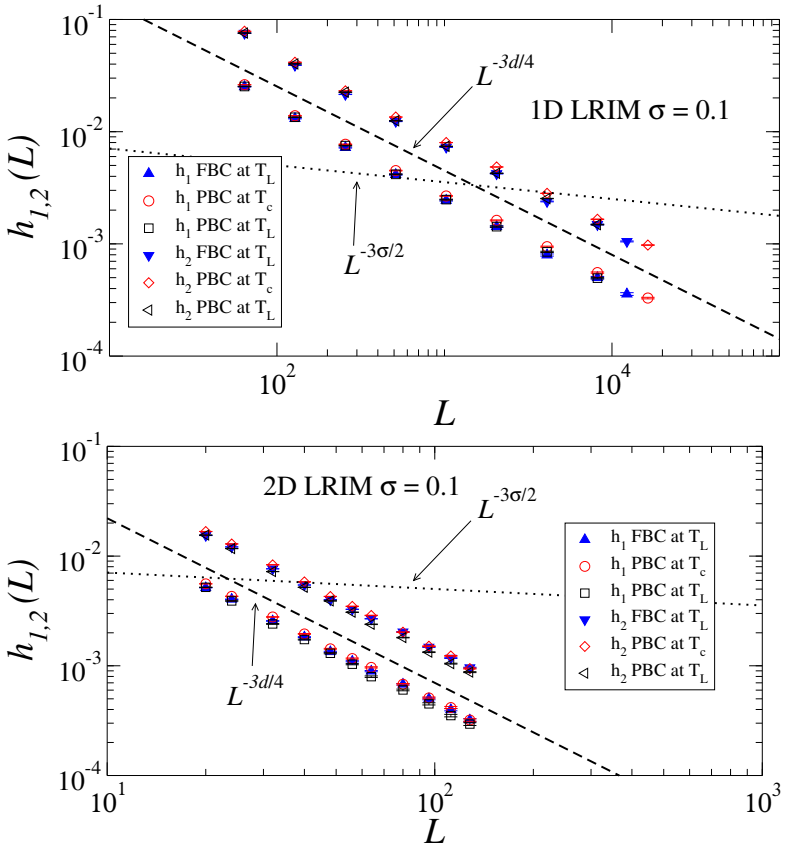

Figure 5.4: FSS of the first two Lee-Yang zeros for LRIM at T_L with PBCs and FBCs and at T_c with PBCs. The upper image shows 1D model and the bottom image the 2D model, both with $\sigma = 0.1$. These results are clearly in favour of QFSS, which predicts $h_j \sim L^{-3d/4}$.

5.4 Conclusion

In this chapter we have seen that FSS for the Fisher and Lee-Yang zeros are fully compatible with QFSS, and indeed they also required the introduction of ♀ in the

correlation length in order to reconcile RG with the MF exponents. The impact angle for the Fisher zeros, as it was shown, depends on the boundary conditions. For systems with PBCs the impact angle approximates to $\pi/4$, a earlier estimate for such angle in the MF regime. However the impact angle for systems with FBCs converges to zero due to the difference of the scaling between the imaginary and the real part of such zeros.

Chapter 6

Logarithmic corrections for QFSS at the upper critical dimension for the Ising model with long-range interactions

6.1 Introduction

In this chapter we consider critical phenomena at the upper critical dimension. The Gaussian fixed point there becomes marginally stable and this introduces multiplicative logarithmic corrections to the power laws. The correlation length, in such a scheme, experiences a logarithmic counterpart $\hat{\varphi}$, in line with φ in the QFSS. This consideration already was presented in Ref. [94–96] (through the symbols q and counterpart $\hat{q}$), and lately in terms of QFSS, where $\hat{\varphi}$ formally appeared in [41]. The counterpart related to η_φ for the Fisher scaling, named $\hat{\eta}_\varphi$ was numerically corroborated for the 4D SRIM in [42]. Herein, we aim to numerically test the

prediction given by the last references and so we focus on the main logarithmic counterparts for the LRIM with PBCs and FBCs.

This chapter is divided as follow. Section 2 contains the logarithmic scaling corrections. In section 3 QFSS at d_c is presented. Section 4 contains the relations for the logarithmic counterpart for the exponents. In section 5 the solutions for the RG equation for the marginal case are derived. In section 6 the main numerical results are shown. Finally in section 7 the conclusion is given.

6.2 Logarithmic scaling corrections

The multiplicative logarithmic corrections, that appears at d_c, modify the power-law scaling for the observables, in terms of t and h, as follows. The internal energy and the heat capacity are affected as

$$e_\infty(t,0) \sim t^{1-\alpha}|\ln t|^{\hat{\alpha}}, \qquad e_\infty(0,h) \sim h^{\epsilon}|\ln h|^{\hat{\epsilon}}, \tag{6.1}$$

$$c_\infty(t,0) \sim t^{-\alpha}|\ln t|^{\hat{\alpha}}, \qquad c_\infty(0,h) \sim h^{-\alpha_c}|\ln h|^{\hat{\alpha}_c}. \tag{6.2}$$

The magnetisation and the susceptibility are given by

$$m_\infty(t,0) \sim t^{\beta}|\ln t|^{\hat{\beta}}, \qquad m_\infty(0,h) \sim h^{1/\delta}|\ln h|^{\hat{\delta}}, \tag{6.3}$$

$$\chi_\infty(t,0) \sim t^{-\gamma}|\ln t|^{\hat{\gamma}}, \qquad \chi_\infty(0,h) \sim h^{1/\delta-1}|\ln h|^{\hat{\delta}}. \tag{6.4}$$

The correlation length and the correlation function follow

$$\xi_\infty(t,0) \sim t^{-\nu}|\ln t|^{\hat{\nu}}, \qquad \xi_\infty(0,h) \sim h^{-\nu_c}|\ln h|^{\hat{\nu}_c}, \tag{6.5}$$

$$G_\infty(r,t,0) \sim r^{-(d-2+\eta)}|\ln r|^{\hat{\eta}}. \tag{6.6}$$

Finally, the Lee-Yang edge, and so the scaling for the zeros, is affected

$$r_{\mathrm{YL}}(t) \sim t^{\Delta} |\ln t|^{\hat{\Delta}}. \tag{6.7}$$

6.3 Q-finite-size scaling

Here, the correlation length still plays a crucial role because at $d = d_c$ it takes logarithmic corrections given by the marginal value of the self-interaction term. Meanwhile $\wp = 1$, the counterpart $\hat{\wp}$ is controlling the behaviour of the correlation length following

$$\xi_L \sim L |\ln L|^{\hat{\wp}}. \tag{6.8}$$

Either using RG or FSS hypotheses in terms of QFSS, i.e. where ξ can be replaced by $L|\ln L|^{\hat{\wp}}$ in the scaling window regime one can obtain the scaling for the other observables, as is shown in Ref. [94, 96] by Kenna, Johnston and Janke. For the magnetisation, susceptibility and Lee-Yang edge the associated QFSS takes the form of

$$m_L \sim L^{-\frac{\beta}{\nu}} |\ln L|^{\hat{\beta}+\beta\frac{\hat{\nu}-\hat{\wp}}{\nu}}, \tag{6.9}$$

$$\chi_L \sim L^{\frac{\gamma}{\nu}} |\ln L|^{\hat{\gamma}-\gamma\frac{\hat{\nu}-\hat{\wp}}{\nu}}, \tag{6.10}$$

$$r_{LY}(t) \sim L^{-\frac{\Delta}{\nu}} |\ln L|^{\hat{\Delta}+\Delta\frac{\hat{\nu}-\hat{\wp}}{\nu}}. \tag{6.11}$$

Other quantities such as the scaling of the pseudocritical point are also affected by logarithmic corrections. The shifting is now given by

$$t_L \sim L^{-\lambda} |\ln L|^{\hat{\lambda}} \sim L^{-\frac{1}{\nu}} |\ln L|^{\frac{\hat{\nu}-\hat{\wp}}{\nu}}, \tag{6.12}$$

where the hatted shift exponent is

$$\hat{\lambda} = \frac{\hat{\nu} - \hat{\mathfrak{Y}}}{\nu}. \tag{6.13}$$

6.4 Relations for hatted critical exponents

The hatted exponents presented before are also related to each other. These relations can be found by differentiating the subsequent observables from the thermodynamic functions as it has been done along this manuscript. They are contained in [94, 97]. The relations are the following

$$\hat{\alpha} = \begin{cases} 1 + d(\hat{\mathfrak{Y}} - \hat{\nu}) & \text{if } \alpha = 0 \text{ and } \phi \neq \pi/4 \\ d(\hat{\mathfrak{Y}} - \hat{\nu}) & \text{otherwise .} \end{cases}, \tag{6.14}$$

$$2\hat{\beta} - \hat{\gamma} = d(\hat{\mathfrak{Y}} - \hat{\nu}), \tag{6.15}$$

$$\hat{\beta}(\delta - 1) = \delta\hat{\delta} - \hat{\gamma}, \tag{6.16}$$

$$\hat{\eta} = \hat{\gamma} - \hat{\nu}(2 - \eta). \tag{6.17}$$

In QFSS scheme there is also the corresponding counterpart $\hat{\eta}_{\mathfrak{Y}}$, derived from the fluctuation-dissipation at d_c in [42]. The added relations for the hatted exponents in QFSS are

$$\hat{\gamma} = (2 - \eta)\hat{\nu} + \hat{\eta}, \tag{6.18}$$

$$\hat{\gamma} = (2 - \eta_{\mathfrak{Y}})(\hat{\nu} - \hat{\mathfrak{Y}}) + \hat{\eta}_{\mathfrak{Y}}, \tag{6.19}$$

$$\hat{\eta}_{\mathfrak{Y}} = \hat{\eta} + (2 - \eta)\hat{\mathfrak{Y}}. \tag{6.20}$$

For the exponents identified in the scaling relation associated with systems in external magnetic field the relations are given by

$$\hat{\epsilon} = \frac{(\gamma+1)(\hat{\beta}-\hat{\gamma})}{\beta+\gamma}+\hat{\gamma}, \tag{6.21}$$

$$\hat{\alpha}_c = \frac{(\gamma+2)(\hat{\beta}-\hat{\gamma})}{\beta+\gamma}+\hat{\gamma}, \tag{6.22}$$

$$\hat{\delta} = d(\hat{\mathfrak{Y}}-\hat{\nu}), \tag{6.23}$$

$$\hat{\Delta} = \hat{\beta}-\hat{\gamma}. \tag{6.24}$$

The values for these hatted exponents for the LRIM are found to be

$$\hat{\alpha} = \frac{1}{3}, \quad \hat{\beta} = \frac{1}{3}, \quad \hat{\gamma} = \frac{1}{3}, \quad \hat{\delta} = \frac{1}{3}, \tag{6.25}$$

$$\hat{\epsilon} = \frac{1}{3}, \quad \hat{\alpha}_c = \frac{1}{3}, \quad \hat{\nu} = \frac{1}{3\sigma}, \quad \hat{\nu}_c = \frac{6-\sigma}{12\sigma}, \tag{6.26}$$

$$\hat{\Delta} = 0, \quad \hat{\mathfrak{Y}} = \frac{1}{2\sigma}, \quad \hat{\eta} = 0 \quad \hat{\eta}_{\mathfrak{Y}} = \frac{1}{2}. \tag{6.27}$$

All these results are, together with other models at d_c, presented in Ref.[86].

6.5 Solution for the RG equations

We proceed to construct the thermodynamic functions for the marginal case $\sigma_U = d/2$, i.e., at $d = d_c$. We follow the steps given by Luijten in [58] as presented in chapter 4 for the case above d_c. The RG equations, given in Eq.(4.15) now take $\epsilon = 2\sigma - d = 0$. Hence,

$$\begin{aligned} \frac{dr_0}{dl} &= \sigma r_0 + 3au(c-r_0) \\ \frac{du}{dl} &= \epsilon u - 9au^2 = -9au^2. \end{aligned} \tag{6.1}$$

One solves first the equation related to u. Then one introduces $u(l)$ in the differential equation of r_0. Solving this system of first order differential equations, the

corresponding solutions, up to order $u(l)$, are

$$u(l) = \frac{\bar{u}}{1+\tilde{\beta}\bar{u}l}, \tag{6.2}$$

$$r_0(l) = [\bar{r}_0 - \tilde{\alpha}\bar{u}]\, e^{\sigma l}[1+\tilde{\beta}\bar{u}\ln b]^{-\frac{1}{3}} + \frac{\tilde{\alpha}\bar{u}}{1+\tilde{\beta}\bar{u}\ln b}, \tag{6.3}$$

denoting $\bar{u} = u_{l=0}$ and $\bar{r} = r_{l=0}$. The tilde variables follows the notation in chapter 4, they are $\tilde{\beta} = 9a$ and $\tilde{\alpha} = -3ac/(d-\sigma)$ respectively. The logarithmic correction can clearly be identified in the last equation. For set of variables $u(l)$ and $r_0(l)$ one constructs the free energy density up to leading order [58],

$$f_L(t,h,u) = b^{-d} f_{L/b}\left(b^{y_t}\frac{t+\tilde{\alpha}\bar{u}[1+\tilde{\beta}\bar{u}\ln b]^{-2}}{[1+\tilde{\beta}\bar{u}\ln b]^{\frac{1}{3}}}, b^{y_h}h, \frac{u}{1+\tilde{\beta}\bar{u}\ln b}\right)\Bigg(+ g_L(t,h,u), \tag{6.4}$$

where $f_{L/b}(t,h,u)$ is the singular part and $g_L(t,h,u)$ is the analytic part. To treat correctly and take into account the u variables in order to obtain the correct FSS, one has to rescale the free energy density as it was done in chapter 4 through Eq.(4.20) and (4.21). In that sense, one obtains a rescaled version of Eq.(6.4)

$$f(t,h,u,1/L) = b^{-d}F_{L/b}\left(b^{y_t}\frac{t+\tilde{\alpha}\bar{u}[1+\tilde{\beta}\bar{u}\ln b]^{-2}}{[1+\tilde{\beta}\bar{u}\ln b]^{-\frac{1}{6}}}, b^{y_h}h\frac{[1+\tilde{\beta}\bar{u}\ln b]^{\frac{1}{4}}}{u^{1/4}}\right)\Bigg(\tag{6.5}$$

The shifting can be extracted by setting the first argument to a constant value c since the first derivative of susceptibility or the heat capacity should vanish at the pseudocritical point where it experiences a maximum. In that sense, setting $b = L$, the shifting is given by

$$t_L = c\sqrt{u}L^{-d/2}[1+\tilde{\beta}\bar{u}\ln L]^{-\frac{1}{6}}\left(1-\frac{\tilde{\alpha}}{c}[1+\tilde{\beta}\bar{u}\ln L]^{-\frac{1}{2}}\right)\Bigg(\tag{6.6}$$

6.6 Results for PBCs and FBCs

In this section we show the numerical results for the LRIM system at d_c with PBCs and FBCs. We have used the same simulation method and the same configuration presented in chapter 4 and 5 for the set up of the PBCs. The critical points were also found using the FSS for pseudocritical points.

6.6.1 Magnetization and susceptibility

Here, we show the logarithmic corrections for the scaling of the magnetisation and the susceptibility. The expected behaviour for such observables are respectively

$$m_L \sim L^{-d/4}(\ln L)^{\hat{\beta}+\beta(\hat{\nu}-\hat{\wp})/\nu} \sim L^{-d/4}(\ln L)^{1/4}, \tag{6.7}$$

$$\chi_L \sim L^{d/2}(\ln L)^{\hat{\gamma}-\gamma(\hat{\nu}-\hat{\wp})/\nu} \sim L^{d/2}(\ln L)^{1/2}. \tag{6.8}$$

Where $(\hat{\nu}-\hat{\wp})/\nu = -1/6$. In Fig. 6.1 we can observed the validity of these predictions for those systems with PBCs at T_L and T_c and also with FBCs at T_L. For systems with FBCs at T_c DIVs are not affecting its behaviour and then they do not have logarithmic corrections as it can be seen in that figure.

6.6.2 Correlation function and correlation length

We have also analysed the logarithmic corrections for the correlation length and the correlation function. Both are given by

$$\xi_L \sim L(\ln L)^{\hat{\wp}} = L(\ln L)^{1/2\sigma}, \tag{6.9}$$

$$G_L(L/2) \sim L^{-d/2}(\ln L)^{\hat{\eta}\wp} = L^{-d/2}(\ln L)^{1/2}. \tag{6.10}$$

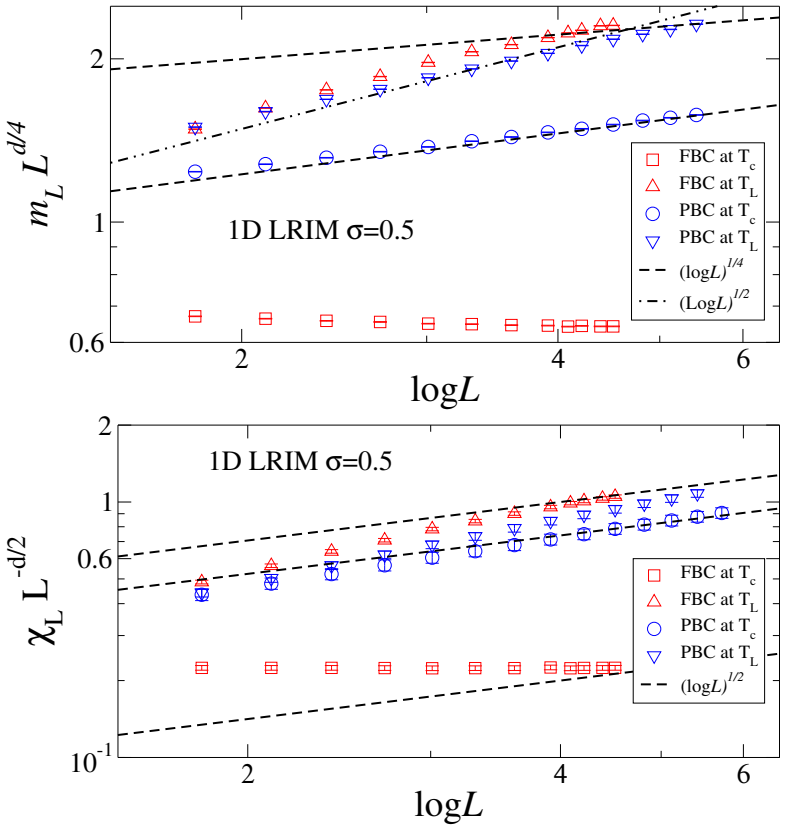

Figure 6.1: FSS for the magnetisation and susceptibility for the 1D LRIM at d_c with PBCs and FBCs. The upper image shows that the scaling with PBCs at T_L and T_c together with FBCs at T_L, up to corrections, follow the expected scaling $m_L \sim (\log L)^{1/4}$ marked as dashed line. The lower image shows that the scaling with PBCs at T_L and T_c together with FBCs at T_L, up to corrections, follow the expected scaling $\chi_L \sim (\log L)^{1/2}$ marked as dashed line. Logarithmic corrections are not observed for systems with FBCs at T_c.

The simulation results for the 1D LRIM at d_c with PBCs and FBCs are plotted in Fig. 6.2. There we can observe that those results with FBCs at T_L, do not show logarithmic correction as expected. For the other set up as PBCs or FBCs at T_L, the scaling approaches slopes compatible with $\hat{\gamma}$ and $\hat{\eta}_{\gamma}$.

6.6.3 Lee-Yang zeros

Finally, we analysed the Lee-Yang zeros scaling which are expected to follow

$$h_j(L) \sim L^{-3d/4}(\log L)^{\hat{\Delta}} \sim L^{-3d/4}, \tag{6.11}$$

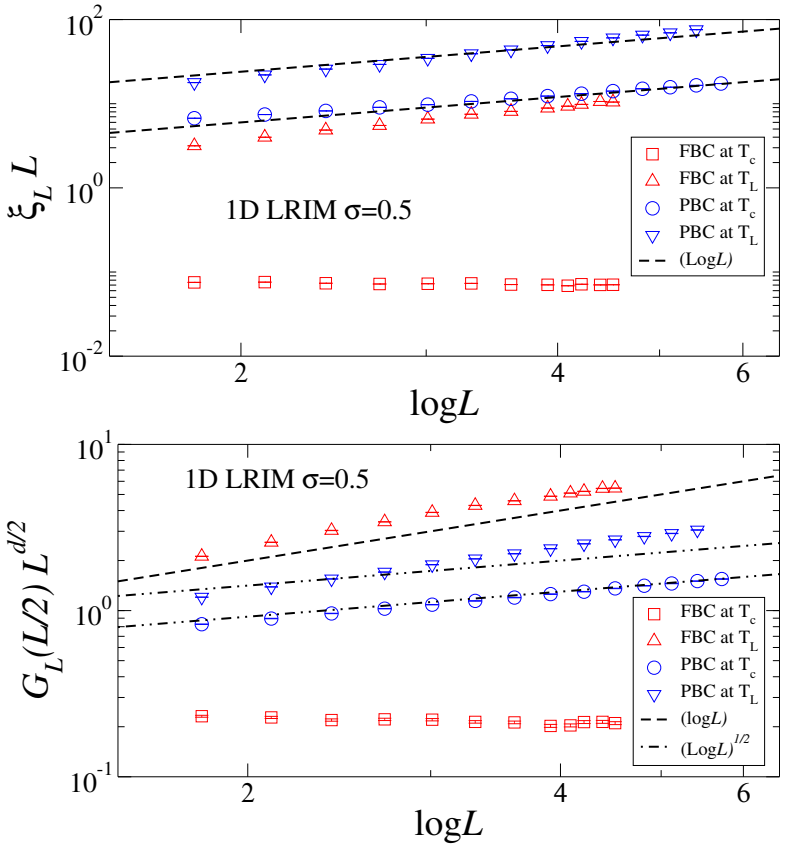

Figure 6.2: FSS for the correlation length and correlation function for the 1D LRIM at d_c with PBCs and FBCs. The upper image shows that the scaling for PBCs at T_L and T_c together with FBCs at T_L, up to corrections, follow the expected scaling $\xi_L \sim (\log L)$ marked as dashed line. The lower image shows that the scaling with PBCs at T_L and T_c together with FBCs at T_L, up to corrections, follow the expected scaling $G_L(L/2) \sim (\log L)^{1/2}$ marked as dashed line. Logarithmic corrections are not observed for systems with FBCs at T_c.

because $\hat{\Delta} = 0$. In Fig. 6.3 we observed that the logarithmic corrections for the two first Lee-Yang zeros approach zero, up to other corrections given by T_L regime. This shows the validity of the QFSS predictions at d_c.

6.7 Conclusion

We have analysed the FSS for the logarithmic corrections for LRIM at d_c for PBCs and FBCs. There the values for the leading exponents such γ, β, etc. converge either for QFSS or GFSS since $\wp = 1$. The predictions given by the

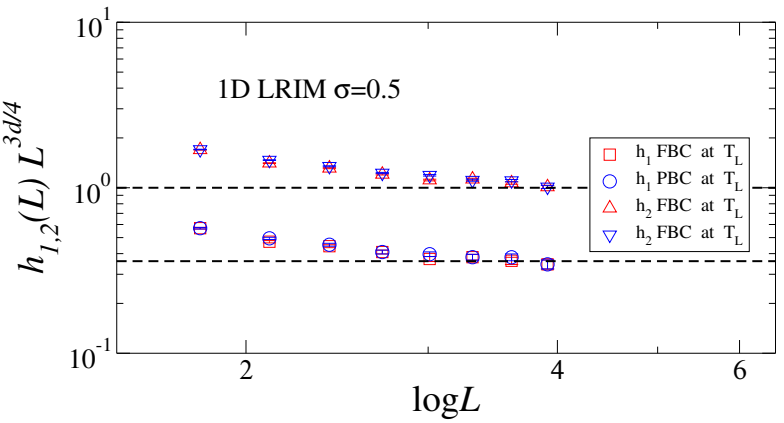

Figure 6.3: FSS for the two first Lee-Yang zeros for the 1D LRIM at d_c with PBCs and FBCs at T_L. One can observe that the expected scaling $h_j(L) \sim L^{-3d/4}(\log L)^0$ is fitted, approaching the dashed line with no slope.

theory for the hatted exponents mainly fit the estimations carried out in this project. The prediction for the counterpart $\hat{\varphi}$, fit suitably the estimations made here. In concordance with FSS for systems with FBCs at T_c where DIVs do no take place, i.e, the regime out of the scaling window, there are not sign of logarithmic corrections.

Chapter 7

Discussion

In chapter 2 we revisited the long-standing problem of FSS. Considering the correlation sector also to be affected by DIVs, as is the free energy, allows one to relax the standard scaling relation for the correlation length in terms of system size, namely $\xi_L \sim L$. This new scheme replaces standard FSS and is called QFSS. In such a scheme the correlation length is dangerously affected by the self-interaction term in the ϕ^4 theory leading to a new scaling behaviour namely $\xi_L \sim L^{\wp}$, with a pseudocritical exponent that takes the value $\wp = 1$ below d_c, but $\wp = d/d_c$ above d_c. The non-trivial relation of the two lengths reconciles the FSS hypothesis and RG. Besides, it gives a repaired formula for hyperscaling namely $\nu d/\wp = 2 - \alpha$, which now is satisfied for any arbitrary dimension. Analogously, the inclusion of such new scaling in the fluctuation-dissipation theorem delivers a complementary anomalous dimension $\eta_{\wp} = 2 - d/2$ which resolves the puzzle about the negative anomalous dimension. Heuristically, the relation between the correlation length and system length may be understand by demanding that the volume of the system is similar to the volume of the correlation length restricted by the critical dimension, i.e., $\xi^{d_c} = L^d$.

In chapter 4, we tested QFSS theory for the LRIM above d_c with different boundary configuration, namely PBCs and FBCs. These systems with long-range interactions can be tuned to the MF regime because one can control the strength of the interaction given by the coupling $r^{-(d+\sigma)}$. In chapter 3 we presented the numerical work to study such systems, specially for the LRIM that approximately contain N^2 interaction. We simulated spin systems for several dimensionalities using a suitable techniques like the Fukui-Todo algorithm. This method is based on extended Fortuin-Kasteleyn representation and it experiences a runtime of $\mathcal{O}(N)$ instead of the typical runtime of the Swendsen-Wang algorithm which is $\mathcal{O}(N^2)$. The FT algorithm also allows one to simulated systems with FBCs where spacial symmetries are not presents. We have also develop a single-cluster variant for the FT algorithm which reduces the autocorrelation time.

In this way, we have measured quantities such as the magnetization, susceptibility, correlation function and correlation length and their FSS. The validity of QFSS is clear through the tables and plots presented in this manuscript, specially for the estimation of the slope of the correlation length that gives straightforwardly that $\wp = d/2\sigma$ (for the LRIM). QFSS prevails for systems with PBCs and with FBCs, but only at pseudocritical point. We have shown that the correct picture to describe the FSS at the critical point for systems with FBCs is GFSS. This is the FSS derived for the Gaussian Fixed Point which prevails when DIVs are suppressed. It is not the same as the predictions from Landau Theory. This occurs when the critical point is located outside of the scaling windows which is in a narrow regime around the pseudocritical point. Although this effect is manifest for the total magnetization at the critical point for systems with FBCs where $\beta^{\dagger} \neq \beta$, the exponent related to the susceptibility coincides for both standard FSS and GFSS $\gamma^{\dagger} = \gamma$. Hence, the final differentiation between the standard FSS and the GFSS was made possible by analysing the non-zero modes which decouple with DIVs.

As complement to QFSS, we have measured the Lee-Yang and Fisher zeros and the impact angle for the 1D LRIM above d_c. There we have shown that the impact angle depends on the boundary conditions finding that for PBCs it approaches $\pi/4$. Instead for FBCs the angles seem to approach zero. To finish this project we have also checked the logarithmic corrections for the $\hat{\mathfrak{f}}$ counterpart, when the variables of the self-interaction terms become marginal. We have shown that QFSS at d_c is coherent with the ansatz of a relaxed scaling for the correlation length for the logarithmic corrections. This scaling, indeed, is given by $\xi_L \sim L(\ln L)^{\hat{\mathfrak{f}}}$.

Some of the results presented here are published in Ref. [43, 44].

Appendix A

Walker's method of Alias

The alias method allow us to generate a probability distribution from a discrete sampling. Here we present Walker's algorithm together with an optimization given by Fukui and Todo in the appendix of [62]. We shall illustrate the alias method using one example related to our simulation, the 1D LRIM with PBCs and $\sigma = 0.1$ for $L = 12$. In this example one uses the invariance symmetry given by PBC and then, instead of J_ℓ couplings with $\ell = 1, \ldots, N_b$, one has that $J_i = 1, \ldots, L-1$. Hence one can assign a $p_i = J_i/J_{\text{tot}}$ to each coupling, or rough speaking to each distance since $J_i = r_i^{-(d+\sigma)}$, satisfying $\sum_i p_i = 1$. Walker's method uses two tables $0 < P_i < 1$, which is a modified probability distribution and alias numbers A_i's that associates two couplings. The modified distribution probability determined by $P_i = Np_i$, where $N = L^d$. The algorithm for choosing an i bond, or distance following the example, is

1. Chose randomly a k spin in the lattice, $1 \leq k \leq L^d$.

2. Throw a random number $0 \leq g < 1$.

3. If $g \leq P_k$ continue with $i = k$, otherwise $i = A_k$.

Summarizing, if we look the table [A.1], the probability to choose $i = 2$, in this case, is with a $g < P_2$ plus another $g \geq P_8$. This is expressed in general by

$$p_i = \frac{1}{N}\left[P_i + \sum_{j=i}^{N}(1 - P_j)\delta_{i,Aj}\right]\Bigg(\tag{A.1}$$

Table A.1: This table contains all the needed data for Walker's method in terms of $p_i = J_i/J_{\text{tot}}$ for 1D LRIM with PBC and $\sigma = 0.1$ for $L = 12$

i	1	2	3	4	5	6	7	8	9	10	11
p_i	0.120	0.093	0.085	0.082	0.080	0.079	0.080	0.082	0.085	0.093	0.120
P_i	1.000	0.925	0.937	0.898	0.880	0.874	0.880	0.898	0.937	0.907	0.910
A_i	-	1	11	11	11	11	10	2	1	1	1

In order to assign the A_i properly one has to divide the p_i in two blocks, those $P_i \geq 1$ and those $P_i < 1$. The $\circ$ denotes the last i with $P_i \geq 1$ and $\bullet$ the last with $P_i < 1$.

				$\circ$							$\bullet$
i	1	2	10	11	9	8	7	6	5	4	3
P_i	1.321	1.027	1.027	1.321	0.937	0.898	0.880	0.874	0.880	0.898	0.937

The assignation of A_i's starts consecutively from the $\bullet$ following this step until the $\bullet$ and $\circ$ take the same place. The step is, giving a new P_i to the element marked with $\circ$, in our case $i = 11$, following $P'_\circ = P_\circ - (1 - P_\bullet)$, then $A_\bullet = \circ$. And the $\bullet$ is passed to the next left element. One performs this iteration until $P'_\circ < 1$, then $\circ$ goes to the next left element and so on. Here we have iterated until $\circ$ was moved to the $i = 10$, giving for the four first $P_k < 1$ elements the $A_k = 11$.

			$\circ$				$\bullet$				
i	1	2	10	11	9	8	7	6	5	4	3
P_i	1.321	1.027	1.027	0.910	0.937	0.898	0.880	0.874	0.880	0.898	0.937
A_i								11	11	11	11

	○●										
i	1	2	10	11	9	8	7	6	5	4	3
P_i	1.000	0.925	0.907	0.910	0.937	0.898	0.880	0.874	0.880	0.898	0.937
A_i	-	1	1	1	1	2	10	11	11	11	11

Following that criteria one finishes the alias table when the two dots coincide. As optional once can set all the rest $P_i \geq 1$ to 1. Indeed this tables is the same as table[A.1]

Appendix B

Ewald sum method

Here, the Ewald sum method is explain in detail follow Ref. [98]. This methodology to manage slow convergent sum has been used in this project in order to set up in a proper way the PBCs for systems with LRIs. As we have seen, we had to modify the coupling in Eq.(3.1) to Eq.(3.52). In this set up the LRIM Hamiltonian takes the form of

$$\mathcal{H} = -\lim_{\mathbf{k}\to\infty} \sum_{\mathbf{n}=-\mathbf{k}}^{\mathbf{k}} \sum_{i<j} \left(\frac{s_i s_j}{|\mathbf{r}_{ij} + \mathbf{n}L|^{d+\sigma}}, \right. \tag{B.1}$$

where $\mathbf{r}_{ij} = \mathbf{r}_i - \mathbf{r}_j$ and the replicas were introduced through the terms $\boldsymbol{n} = \sum_i n_i \hat{\boldsymbol{e}}_i$ with $n_i \in \mathcal{Z}$. They refer to the positions that the replicas take over along an infinite space. In order to sum last expression, we use the properties of the complete and incomplete gamma functions given respectively by

$$\Gamma(x) = \int_0^\infty t^{x-1} e^{-t} dt = \lambda^z \int_0^\infty t^{x-1} e^{-\lambda t} dt, \tag{B.2}$$

$$\Gamma(x,y) = \int_y^\infty t^{x-1} e^{-t} dt. \tag{B.3}$$

We also consider the result for this exponential integral

$$e^{-a^2 w^2} = \frac{\sqrt{\pi}}{a} \int_0^\infty e^{-\frac{\pi^2 u^2}{a^2}} e^{-2\pi i w u} du. \tag{B.4}$$

The Ewald method is implemented as follows. One identifies the and $\lambda = |\mathbf{r}_{ij}+\mathbf{n}L|^2$ and $x = (d+\sigma)/2$ in Eq.(B.2). The isolating λ one gets

$$\frac{1}{|\mathbf{r}_{ij}+\mathbf{n}L|^{d+\sigma}} = \frac{1}{\Gamma(\frac{d+\sigma}{2})}\int_0^\infty t^{\frac{d+\sigma}{2}-1}e^{-|\mathbf{r}_{ij}+\mathbf{n}L|^2 t}dt. \tag{B.5}$$

In that sense the decaying interaction coupling including infinite number of replicas looks like

$$\begin{aligned}
\mathcal{J}_{ij} &= \sum_n \frac{1}{|\mathbf{r}_{ij}+\mathbf{n}L|^{d+\sigma}} = \sum_n \left(\frac{1}{\Gamma(\frac{d+\sigma}{2})}\int_0^\infty t^{\frac{d+\sigma}{2}-1}e^{-|\mathbf{r}_{ij}+\mathbf{n}L|^2 t}dt, \right. && \text{(B.6)}\\
&= \sum_n \left(\frac{1}{\Gamma(\frac{d+\sigma}{2})}\int_0^{\alpha^2} t^{\frac{d+\sigma}{2}-1}e^{-|\mathbf{r}_{ij}+\mathbf{n}L|^2 t}dt \right. && \text{(B.7)}\\
&+ \sum_n \left(\frac{1}{\Gamma(\frac{d+\sigma}{2})}\int_{\alpha^2}^\infty t^{\frac{d+\sigma}{2}-1}e^{-|\mathbf{r}_{ij}+\mathbf{n}L|^2 t}dt, \right. && \text{(B.8)}
\end{aligned}$$

where the integral has been divided into two part of intervals $[0,\alpha^2]$ and $[\alpha^2,\infty)$. One focuses on the second term given in Eq.(B.8), renaming $\mathbf{r}_{ij}+\mathbf{n}L|t = s$. Thus

$$\begin{aligned}
\int_{\alpha^2}^\infty t^{\frac{d+\sigma}{2}-1}e^{-|\mathbf{r}_{ij}+\mathbf{n}L|^2 t}dt &= \frac{1}{|\mathbf{r}_{ij}+\mathbf{n}L|^{d+\sigma}}\int_{\alpha^2|\mathbf{r}_{ij}+\mathbf{n}L|^2}^\infty s^{\frac{d+\sigma}{2}-1}e^{-s}ds,\\
&= \frac{\Gamma(\frac{d+\sigma}{2},\alpha^2|\mathbf{r}_{ij}+\mathbf{n}L|^2)}{|\mathbf{r}_{ij}+\mathbf{n}L|^{d+\sigma}}.
\end{aligned} \tag{B.9}$$

In this manner the second term can be written in a compact form in terns of an incomplete gamma function. The first term given in Eq.(B.7), is summed using the Poisson-Jacobi formula [99]

$$\sum_{\mathbf{n}} e^{-|\mathbf{r}_{ij}+\mathbf{n}L|^2 t} = \frac{1}{L^d}\left(\frac{\pi}{t}\right)^{\frac{d}{2}}\sum_{\mathbf{k}\in\mathcal{R}}\left(e^{i\mathbf{k}\cdot\mathbf{r}}e^{-\frac{k^2}{4t}}, \right. \tag{B.10}$$

with $\mathbf{k} = 2\pi/L\mathbf{n}'$ with $\mathbf{n}'\in\mathcal{N}$. Incorporating last result in Eq.(B.7)

$$\frac{1}{\Gamma(\frac{d+\sigma}{2})}\int_0^{\alpha^2} t^{\frac{d+\sigma}{2}-1}\sum_n e^{-|\mathbf{r}_{ij}+\mathbf{n}L|^2 t}dt = \frac{1}{L^d}\frac{1}{\Gamma(\frac{d+\sigma}{2})}\sum_{\mathbf{k}\in\mathcal{R}}\int_0^{\alpha^2} t^{\frac{d+\sigma}{2}-1}\left(\frac{\pi}{t}\right)^{\frac{d}{2}}e^{i\mathbf{k}\cdot\mathbf{r}}e^{-\frac{k^2}{4t}}dt. \tag{B.11}$$

Simplifying this expression and if one applies the following change of variables $\frac{k^2}{4} = ts$, one then writes

$$= \frac{1}{L^d}\frac{\pi^{\frac{d}{2}}}{\Gamma(\frac{d+\sigma}{2})}\sum_{\mathbf{k}\in\mathcal{R}} e^{i\mathbf{k}\cdot\mathbf{r}} \int_0^{\alpha^2} t^{\frac{\sigma}{2}-1}e^{-\frac{k^2}{4t}}dt = \frac{1}{2^\sigma L^d}\frac{\pi^{\frac{d}{2}}}{\Gamma(\frac{d+\sigma}{2})}\sum_{\mathbf{k}\in\mathcal{R}} e^{i\mathbf{k}\cdot\mathbf{r}} k^\sigma \Gamma\left(-\frac{\sigma}{2}, \frac{k^2}{4\alpha^2}\right), \tag{B.12}$$

The terms has also been compacted in terms of incomplete gamma function, but in the reciprocal space. The limit for $\mathbf{k} = \mathbf{0}$ generates a independent factor that will be included in the final result.

Merging all the computed integrals, the coupling finally is written as

$$\mathcal{J}_{ij} = \frac{1}{\Gamma(\frac{d+\sigma}{2})}\Big[\sum_n \frac{\Gamma(\frac{d+\sigma}{2}, \alpha^2|\mathbf{r}_{ij}+\mathbf{n}L|^2)}{|\mathbf{r}_{ij}+\mathbf{n}L|^{d+\sigma}} \tag{B.13}$$

$$+ \frac{\pi^{\frac{d}{2}}}{2^\sigma L^d}\sum_{k\in\mathcal{R}} e^{ik\cdot r}k^\sigma\Gamma(-\frac{\sigma}{2}, \frac{k^2}{4\alpha^2}) + \frac{2}{\sigma}\frac{\pi^{\frac{d}{2}}}{L^d}\alpha^\sigma\Big]. \tag{B.14}$$

The sum now is perform in the real and Fourier space with and extra does not depend on σ and it rapidly converges. The distance α that splits the sum in order to be able to perform this calculation has to be set according to the quantities d, σ, $\mathbf{k}$ and $\mathbf{n}$. To estimate α one has to maximise the coupling. This is perform by

$$\frac{d}{d\alpha}\mathcal{J}_{ij} = 0. \tag{B.15}$$

The coupling can be written as

$$\mathcal{J}_{ij} = \frac{1}{\Gamma(\frac{d+\sigma}{2})}\Big[\sum_{\mathbf{n}} \Phi_I + \sum_{\mathbf{k}\in\mathcal{R}} \Phi_{II} + \Phi_{III}\Big] \tag{B.16}$$

For each member one calculates its differentiate with respect to α. respectively these are

$$\frac{d}{d\alpha}\Phi_I = -2e^{-\alpha^2|\mathbf{r}_{ij}+\mathbf{n}L|^2}\alpha^{d+\sigma-1}, \tag{B.17}$$

$$\frac{d}{d\alpha}\Phi_{II} = \frac{2\pi^{\frac{d}{2}}}{L^d}e^{-\frac{k^2}{4\alpha^2}}e^{ik\cdot r}\alpha^{\sigma-1}, \tag{B.18}$$

$$\frac{d}{d\alpha}\Phi_{III} = 2\frac{\pi^{\frac{d}{2}}}{L^d}\alpha^{\sigma-1}. \tag{B.19}$$

Hence, the equation for whom root has to be found is

$$-\sum_n e^{-\alpha^2|\mathbf{r}_{ij}+\mathbf{n}L|^2}\alpha^d + \sum_k \left(\frac{\pi^{\frac{d}{2}}}{L^d}e^{-\frac{k^2}{4\alpha^2}}e^{ik\cdot r} + \frac{\pi^{\frac{d}{2}}}{L^d} = 0. \right. \tag{B.20}$$

During this search, one can realise that, indeed, the sum in the Fourier space for the systems consider here can be neglected since by the fast decay suffered. The **n** variable also decays very fast and only dozens of terms have to be take into account.

Appendix C

Supplementary material

In this appendix and for the future reference, we present plots corresponding to the 2D and 3D LRIM above d_c for system with PBCc and FBCs. FSS is shown for the following quantities: the shift, rounding, magnetization, susceptibility, correlation length, correlation function, and non-zero modes. These quantities for both, 2D and 3D LRIM, with PBCs are respectively illustrated from Fig. C.1 to Fig. C.8. The same quantities for systems with FBCs are respectively plotted from Fig. C.9 to Fig. C.16. We have also included the FSS of the non-zero modes of the magnetization and the susceptibility for the 5D SRIM with PBCs and FBCs, which are plotted in Fig. C.17.

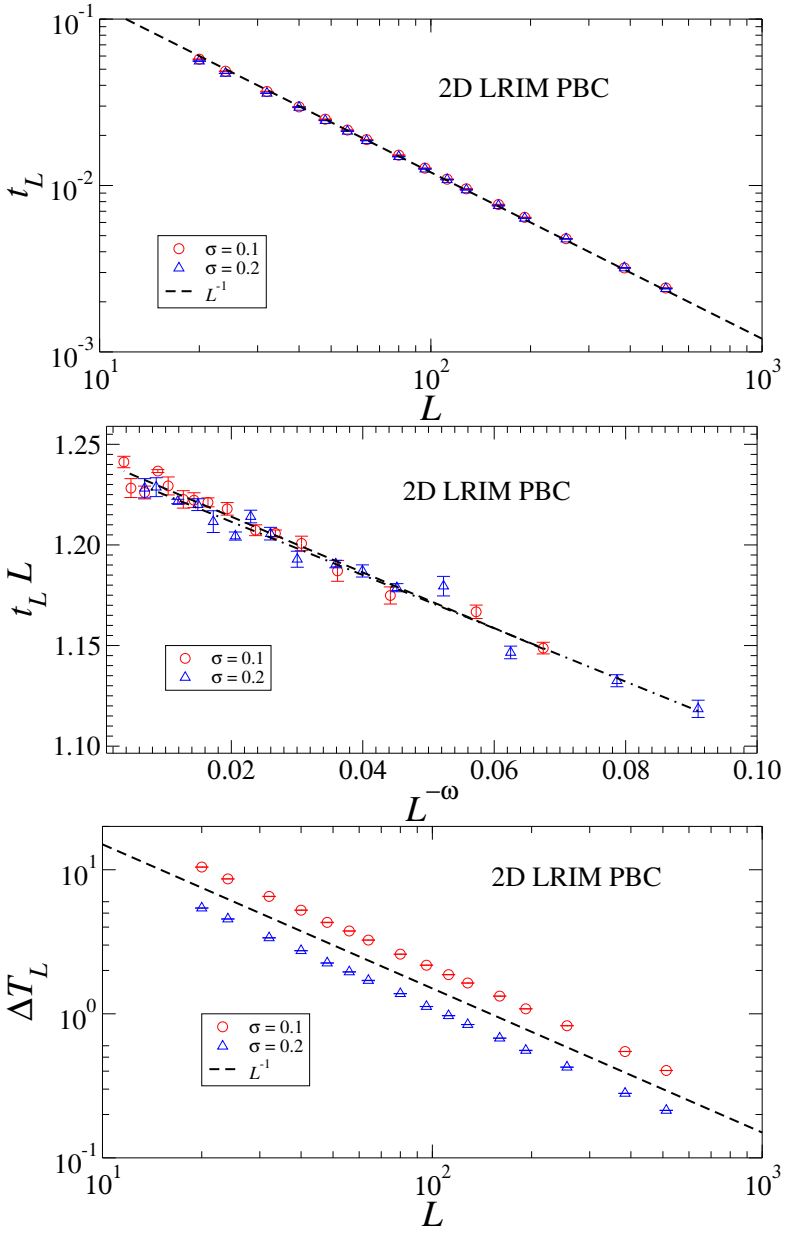

Figure C.1: FSS for the shift and rounding exponents above d_c for the 2D LRIM with PBCs for two σ values 0.1 and 0.2. The top figure shows that the pseudocritical points scale as $t_L \sim L^{-1}$ following the dashed line. The bottom figure shows the scaling for the rounding, following $\Delta T_L \sim L^{-1}$ denoted by the dashed line. QFSS predictions match perfectly such scaling behaviours. In the middle panel the t_L has been normalised by the predicted scaling $t_L \sim L^{-1}$, and the y-axis have also been rescaled by its corresponding $\omega = 0.9$ and 0.8 for $\sigma = 0.1$ and 0.2 respectively. The points follow the straight lines denoted by dashed lines.

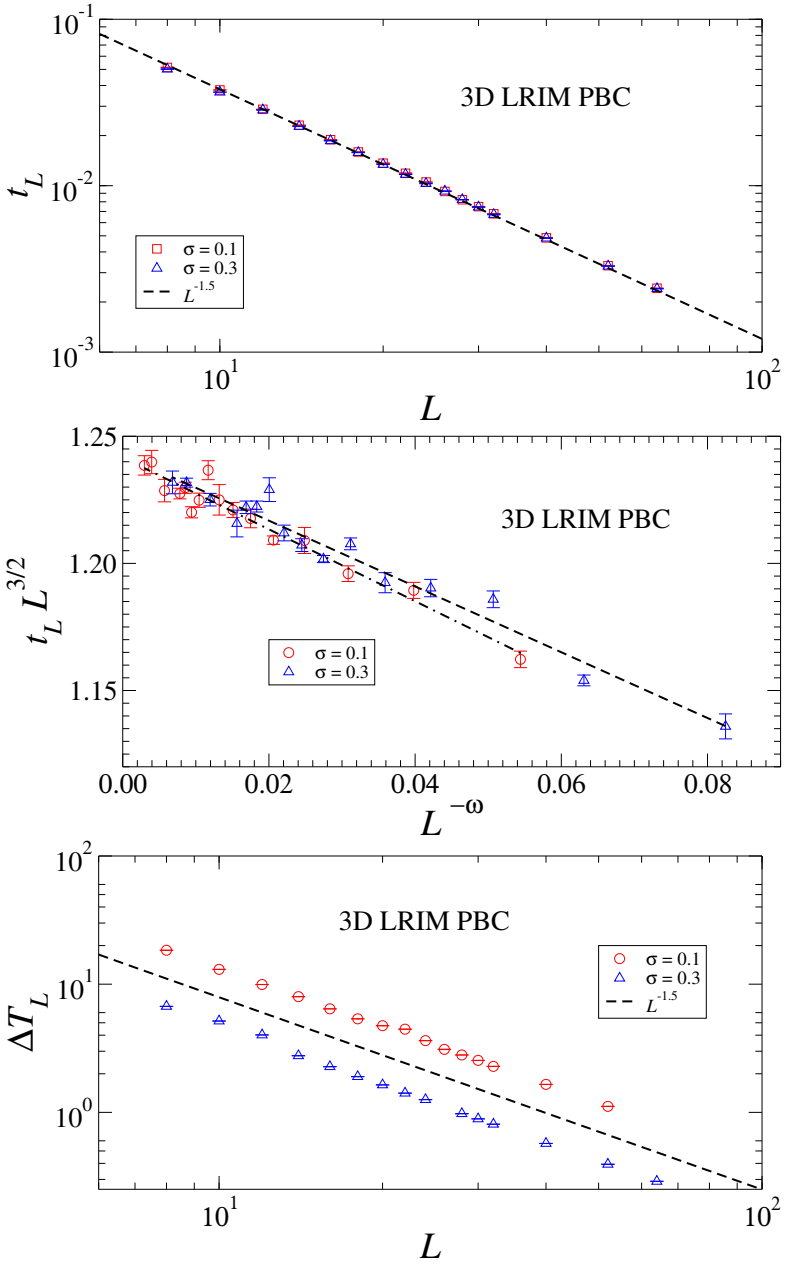

Figure C.2: FSS for the shift and rounding exponents above d_c for the 3D LRIM with PBCs for two σ values 0.1 and 0.3. The top figure shows that the pseudocritical points scale as $t_L \sim L^{-3/2}$ following the dashed line. The bottom figure shows the scaling for the rounding, following $\Delta T_L \sim L^{-3/2}$ denoted by the dashed line. QFSS predictions match perfectly such scaling behaviours. In the middle panel the t_L has been normalised by the predicted scaling $t_L \sim L^{-3/2}$, and the y-axis have also been rescaled by its corresponding $\omega = 1.4$ and 1.2 for $\sigma = 0.1$ and 0.3 respectively. The points follow the straight lines denoted by dashed lines.

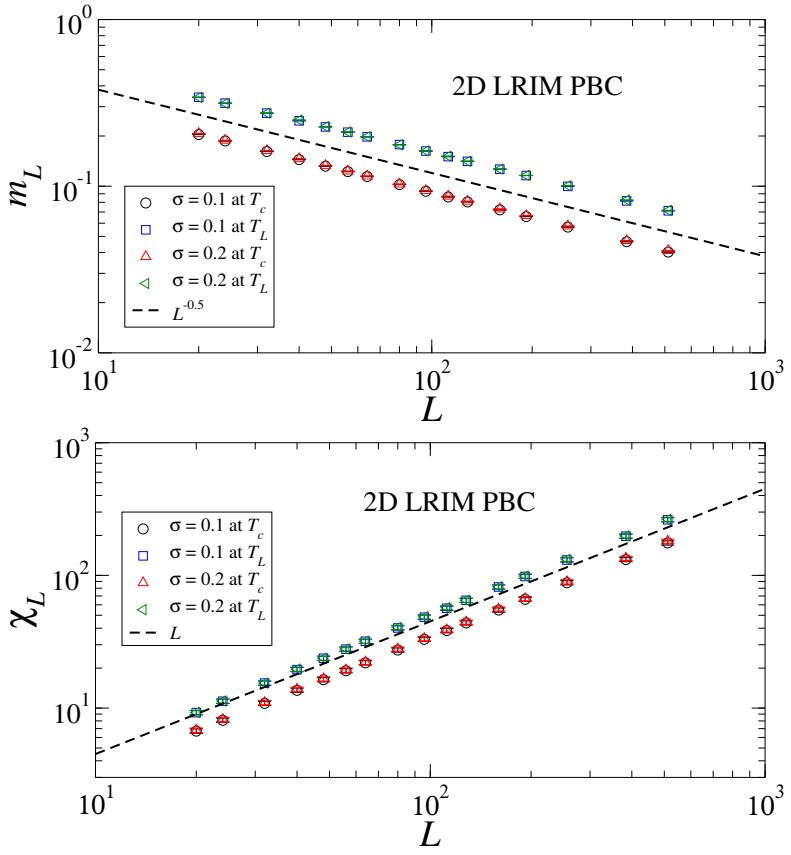

Figure C.3: FSS for the magnetisation and susceptibility for the 2D LRIM with PBCs for $\sigma = 0.1$ and 0.2. In the top image the magnetisation clearly scales as $m_L \sim L^{-1/2}$ following the dashed line. The bottom image shows the susceptibility clearly scaling as $\chi_L \sim L^1$ following the dashed line.

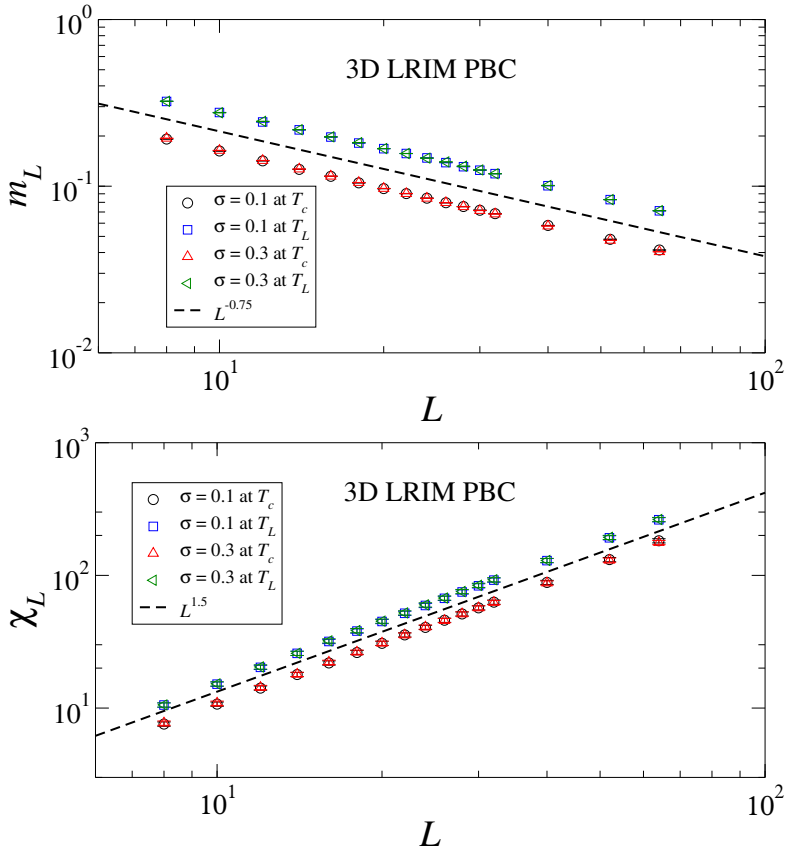

Figure C.4: FSS for the magnetisation and susceptibility for the 3D LRIM with PBCs for $\sigma = 0.1$ and 0.3. In the top image the magnetisation clearly scales as $m_L \sim L^{-3/4}$ following the dashed line. The bottom image shows the susceptibility clearly scaling as $\chi_L \sim L^{3/2}$ following the dashed line.

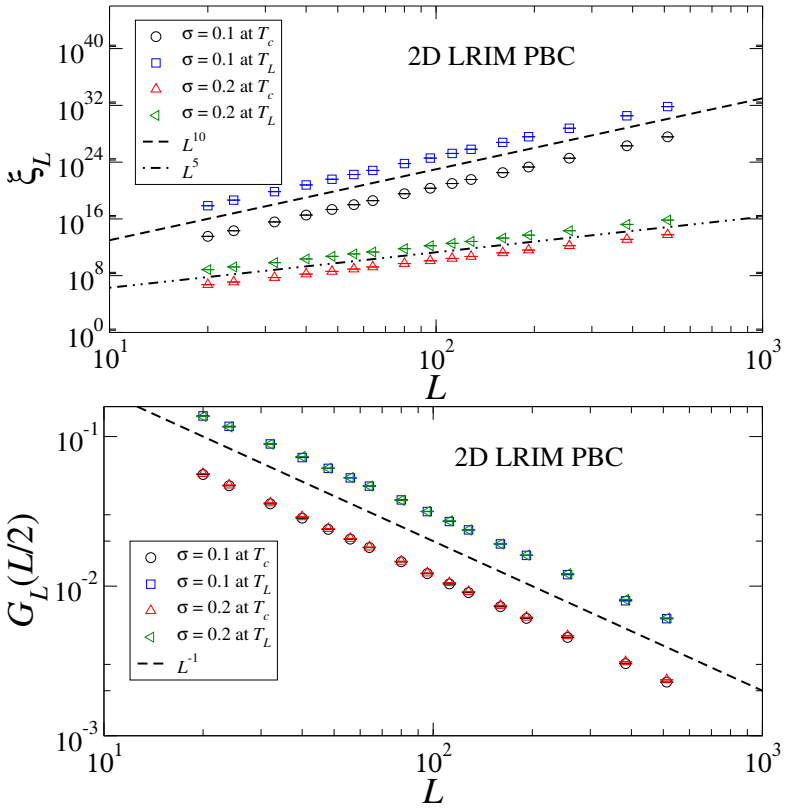

Figure C.5: FSS for the correlation sector for the 1D LRIM. In the upper image the correlation length clearly scales as $\xi_L \sim L^{\wp}$ with $\wp = 10$ for the system with $\sigma = 0.1$ denoted by the short dashed line and $\wp = 5$ for $\sigma = 0.2$, denoted the long dashed line. The lower image shows the correlation function scaling as $G_L(L/2) \sim L^{-1}$ for the dashed line. Both are manifestly favour QFSS.

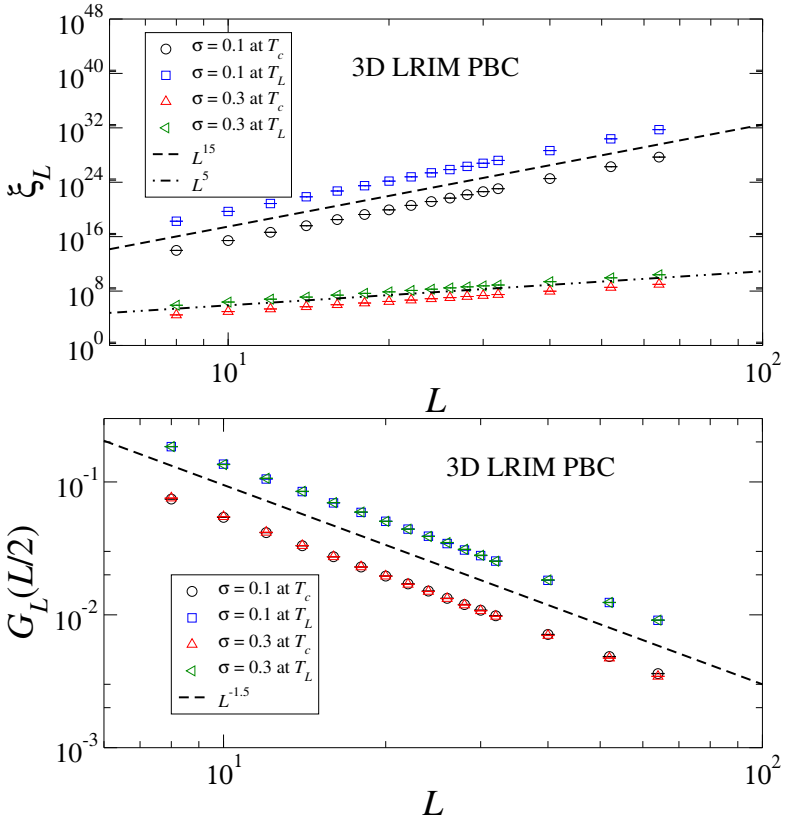

Figure C.6: FSS for the correlation sector for the 1D LRIM. In the upper image the correlation length clearly scales as $\xi_L \sim L^{\wp}$ with $\wp = 15$ for the system with $\sigma = 0.1$ denoted by the short dashed line and $\wp = 5$ for $\sigma = 0.3$, denoted the long dashed line. The lower image shows the correlation function scaling as $G_L(L/2) \sim L^{-3/2}$ for the dashed line. Both are manifestly favour QFSS.

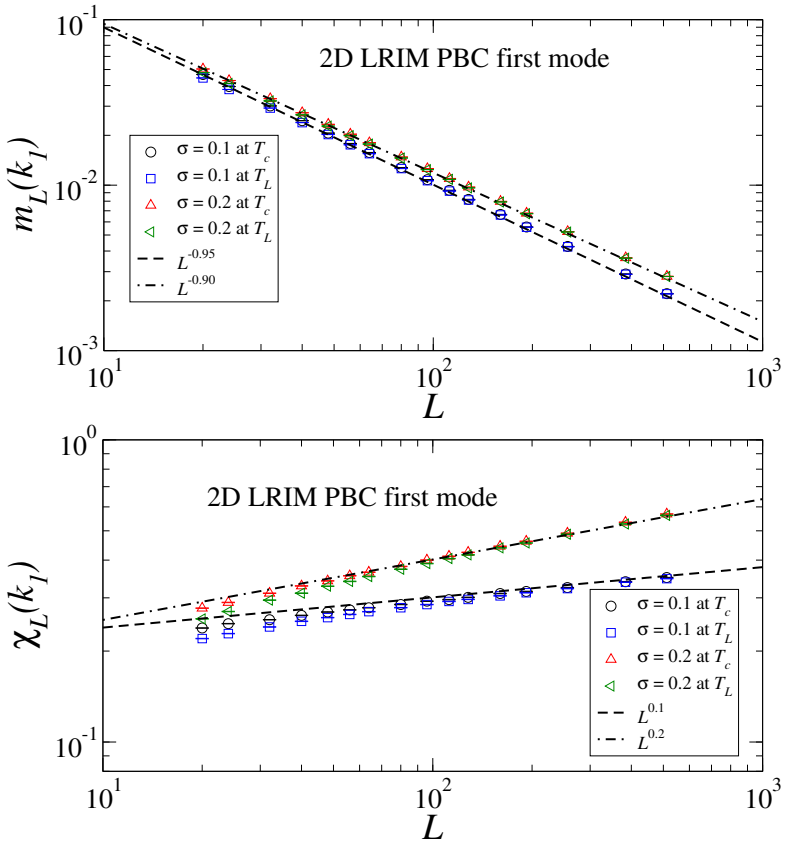

Figure C.7: FSS in the magnetisation sector for non-zero modes for the 2D LRIM with PBCs. In the top image the first magnetisation mode clearly scales as $m_L^\dagger \sim L^{-(2-\sigma)/2}$. In the bottom image the first susceptibility mode clearly scales as $\chi_L^\dagger \sim L^\sigma$. Both manifestly in favour of GFSS instead of the standard FSS.

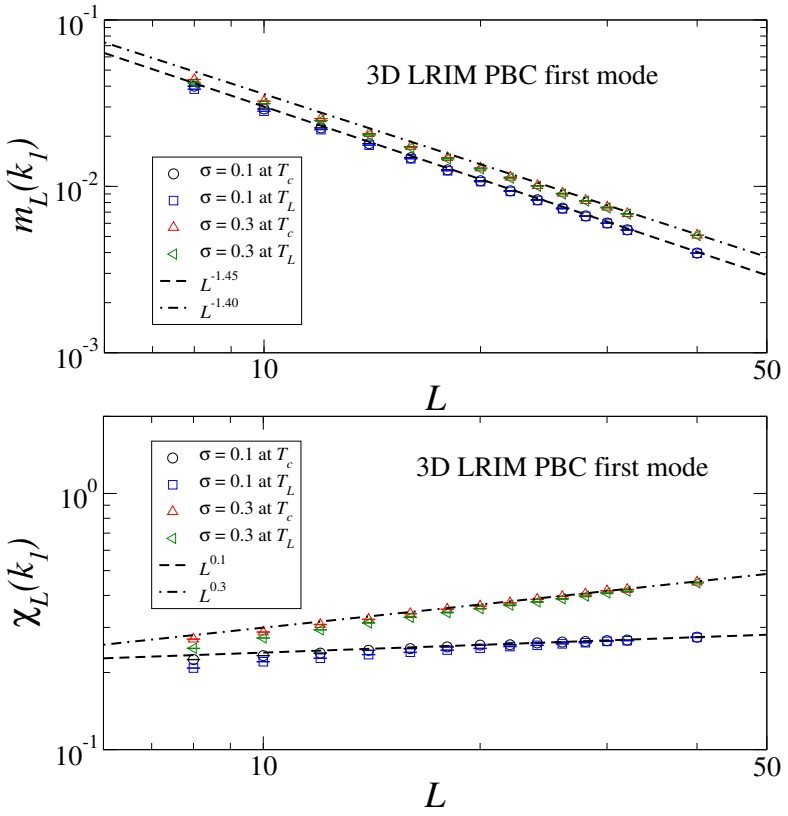

Figure C.8: FSS in the magnetisation sector for non-zero modes for the 3D LRIM with PBCs. In the top image the first magnetisation mode clearly scales as $m_L^\dagger \sim L^{-(3-\sigma)/2}$. In the bottom image the first susceptibility mode clearly scales as $\chi_L^\dagger \sim L^\sigma$. Both manifestly in favour of GFSS instead of the standard FSS.

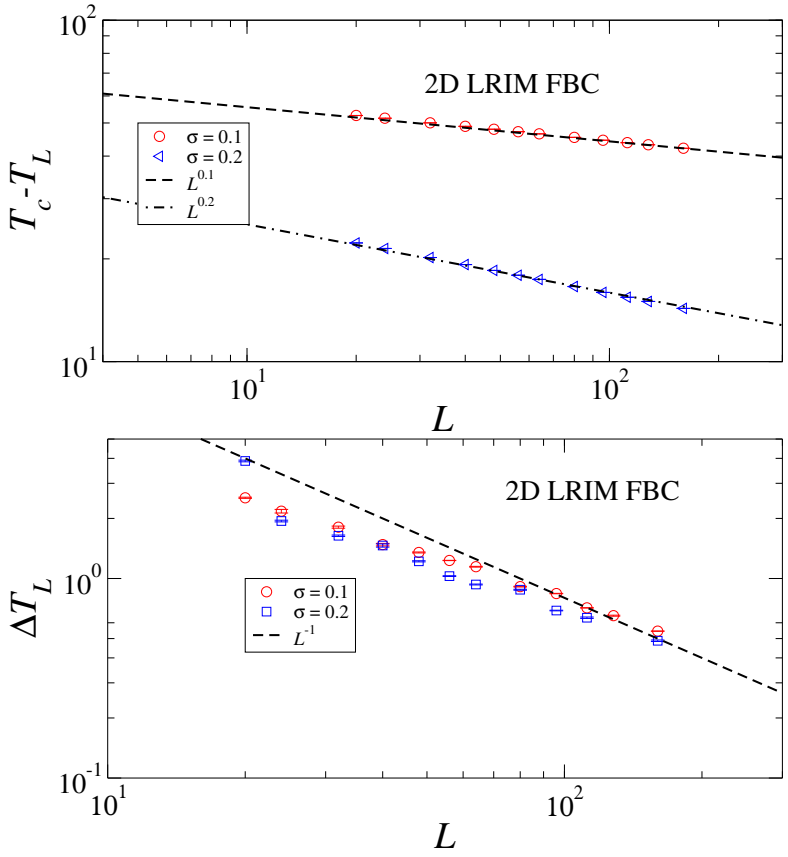

Figure C.9: FSS for the shift and rounding exponents above d_c for the 2D LRIM with FBCs for two σ values 0.1 and 0.2. Top figure shows that the pseudocritical points T_L scale as $T_c - T_L \sim L^{-\sigma}$ following the dashed lines. The bottom figure shows the scaling for the rounding, both scaling approaching $\Delta T_L \sim L^{-1}$ denoted by the dashed line. GFSS takes over pseudocritical points and QFSS fits for the rounding.

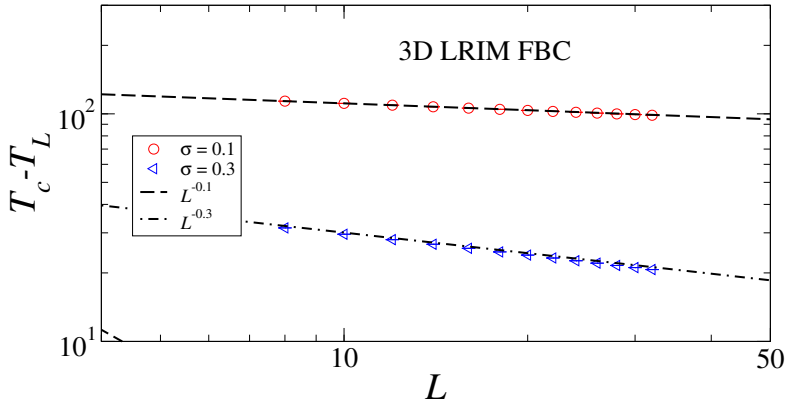

Figure C.10: FSS for the shift exponent above d_c for the 3D LRIM with FBCs for two σ values 0.1 and 0.3. The figure shows that the pseudocritical points T_L scale as $T_c - T_L \sim L^{-\sigma}$ following the dashed lines.

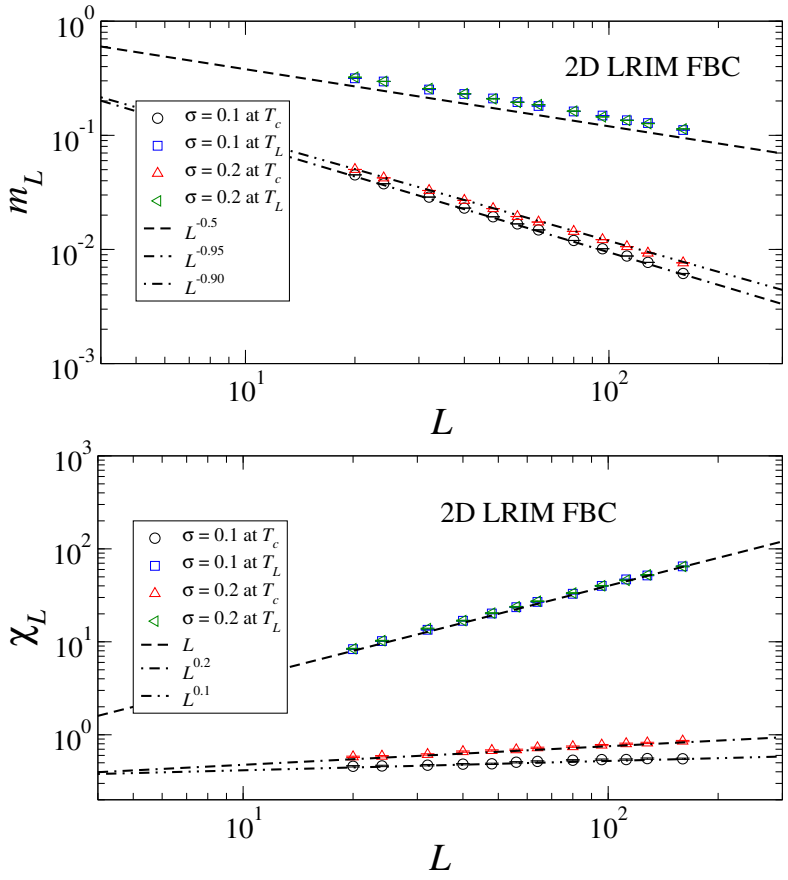

Figure C.11: FSS for the magnetisation sector for the 2D LRIM with FBCs. In the top image the magnetisation clearly scales as $m_L \sim L^{-1/2}$ at T_L and $m_L^\dagger \sim L^{-(2-\sigma)/2}$ at T_c. In the bottom image the susceptibility clearly scales as $\chi_L \sim L$ at T_L and $\chi_L^\dagger \sim L^\sigma$ at T_c. These results are in favour of QFSS at T_L, and GFSS at T_c.

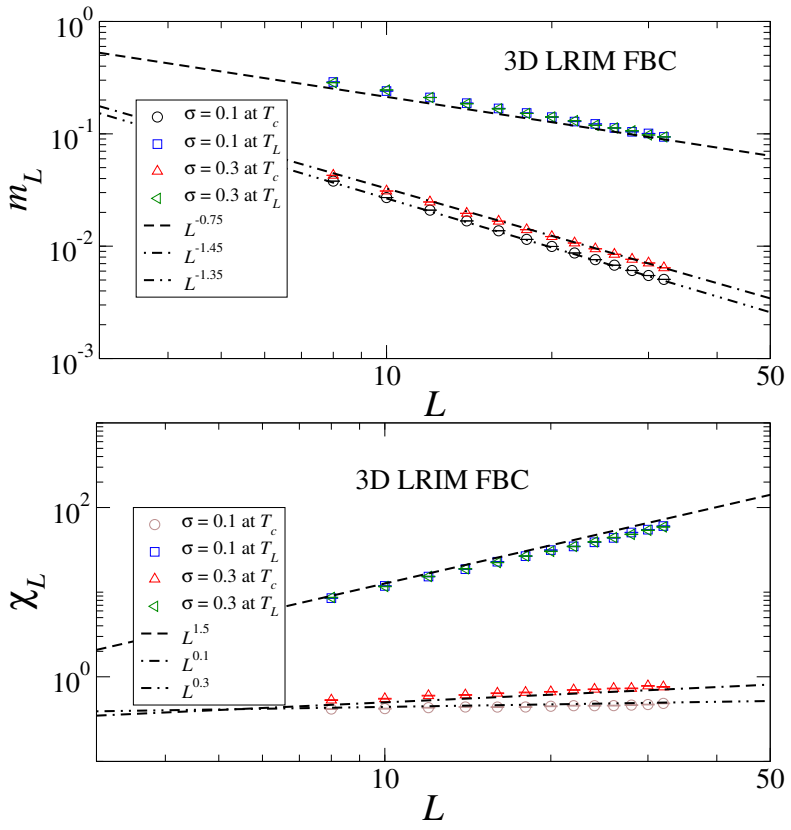

Figure C.12: FSS for the magnetisation sector for the 3D LRIM with FBCs. In the top image the magnetisation clearly scales as $m_L \sim L^{-3/4}$ at T_L and $m_L^\dagger \sim L^{-(3-\sigma)/2}$ at T_c. In the bottom image the susceptibility clearly scales as $\chi_L \sim L^{3/2}$ at T_L and $\chi_L^\dagger \sim L^\sigma$ at T_c. These results in favour of QFSS at T_L, and GFSS at T_c.

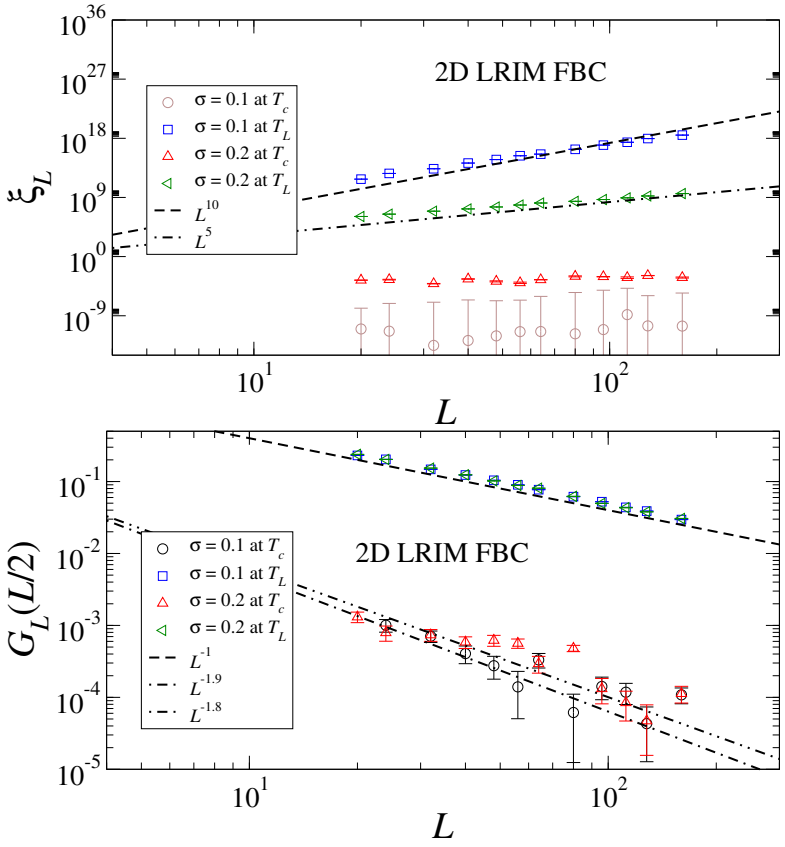

Figure C.13: FSS for the correlation sector for the 1D LRIM. In the upper image the correlation length clearly scales as $\xi_L \sim L^{\wp}$ with $\wp = 15$ for the system with $\sigma = 0.1$ denoted by the short dashed line and $\wp = 5$ for $\sigma = 0.3$, denoted the long dashed line. The lower image shows the correlation function scaling as $G_L(L/2) \sim L^{-3/2}$ for the dashed line. Both are manifestly favour QFSS.

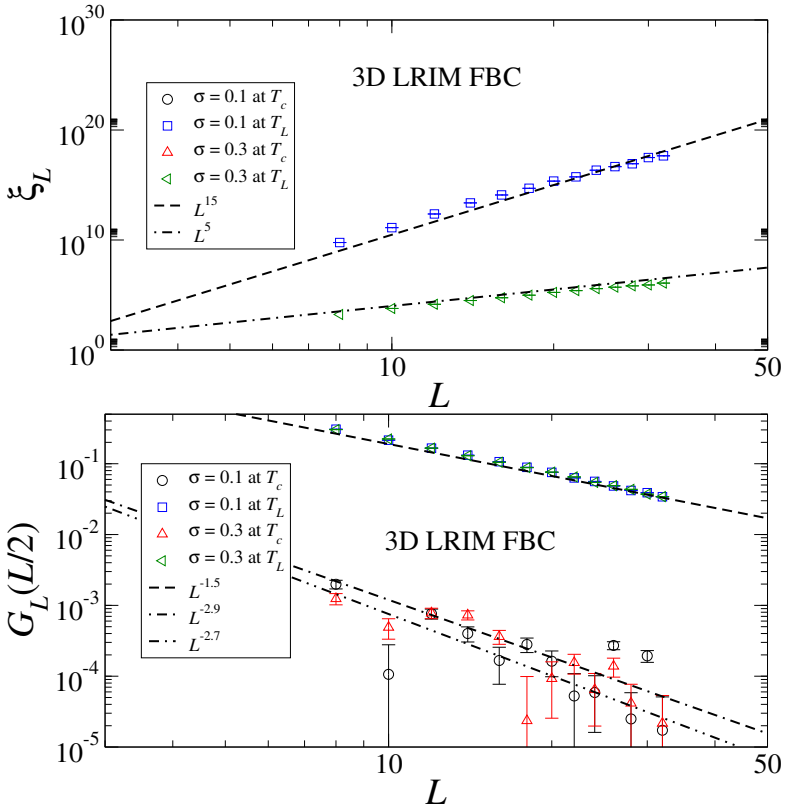

Figure C.14: FSS for the correlation sector for the 1D LRIM. In the upper image the correlation length clearly scales as $\xi_L \sim L^{\wp}$ with $\wp = 15$ for the system with $\sigma = 0.1$ denoted by the short dashed line and $\wp = 5$ for $\sigma = 0.3$, denoted the long dashed line. The lower image shows the correlation function scaling as $G_L(L/2) \sim L^{-3/2}$ for the dashed line. Both are manifestly favour QFSS.

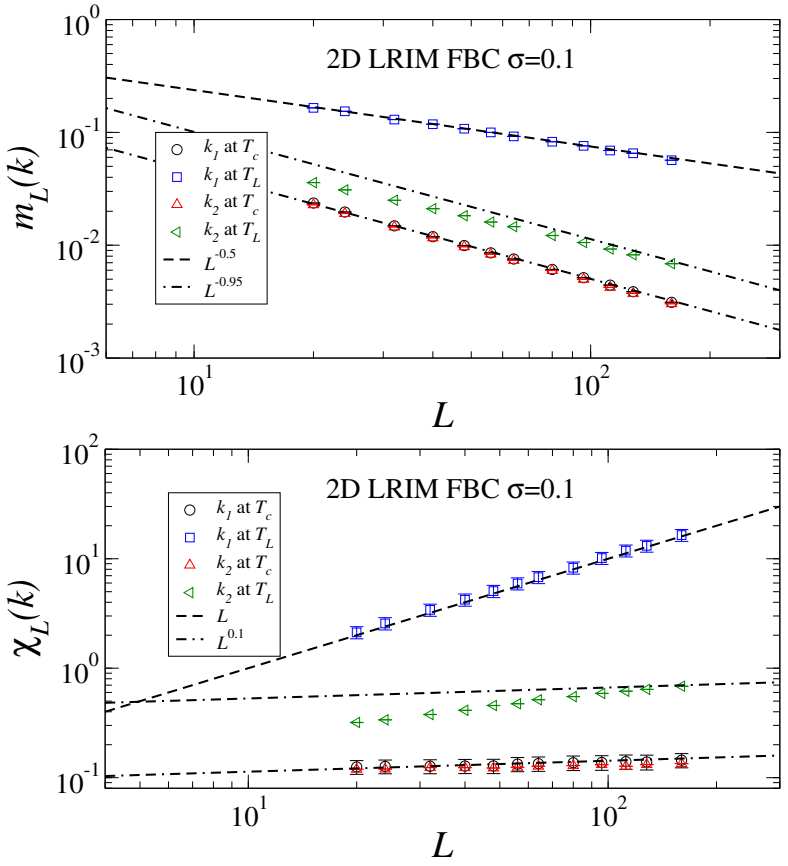

Figure C.15: FSS in the magnetisation sector for non-zero modes for the 2D LRIM with FBCs. In the top image the first magnetisation mode clearly scales as $m_L^\dagger \sim L^{-(2-\sigma)/2}$. In the bottom image the first susceptibility mode clearly scales as $\chi_L^\dagger \sim L^\sigma$. Both manifestly in favour of GFSS instead of the standard FSS.

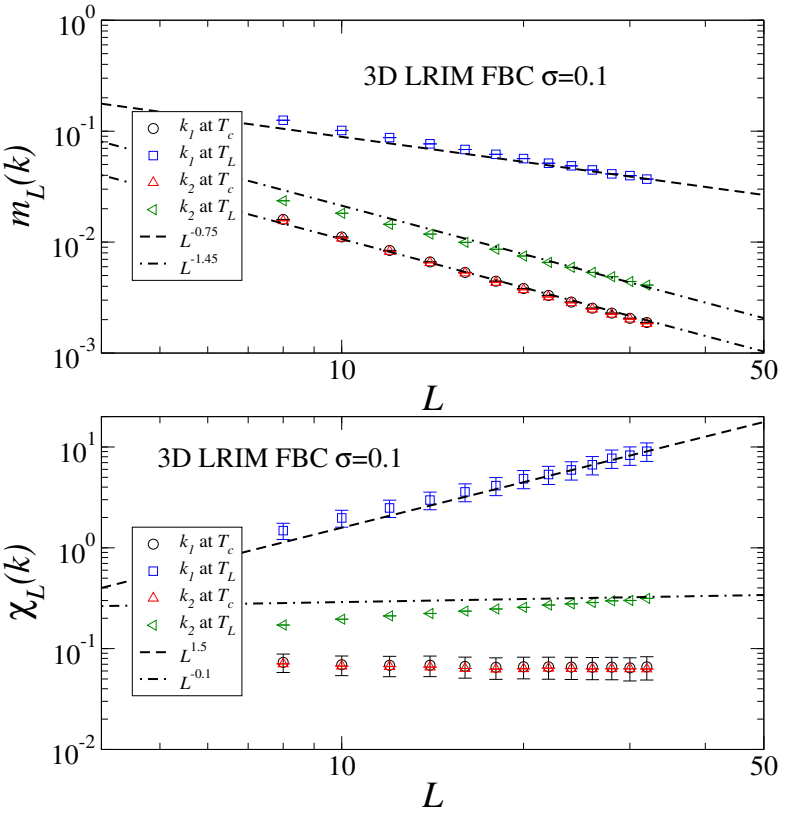

Figure C.16: FSS in the magnetisation sector for non-zero modes for the 3D LRIM with FBCs. In the top image the first magnetisation mode clearly scales as $m_L^\dagger \sim L^{-(3-\sigma)/2}$. In the bottom image the first susceptibility mode clearly scales as $\chi_L^\dagger \sim L^\sigma$. Both manifestly in favour of GFSS instead of the standard FSS.

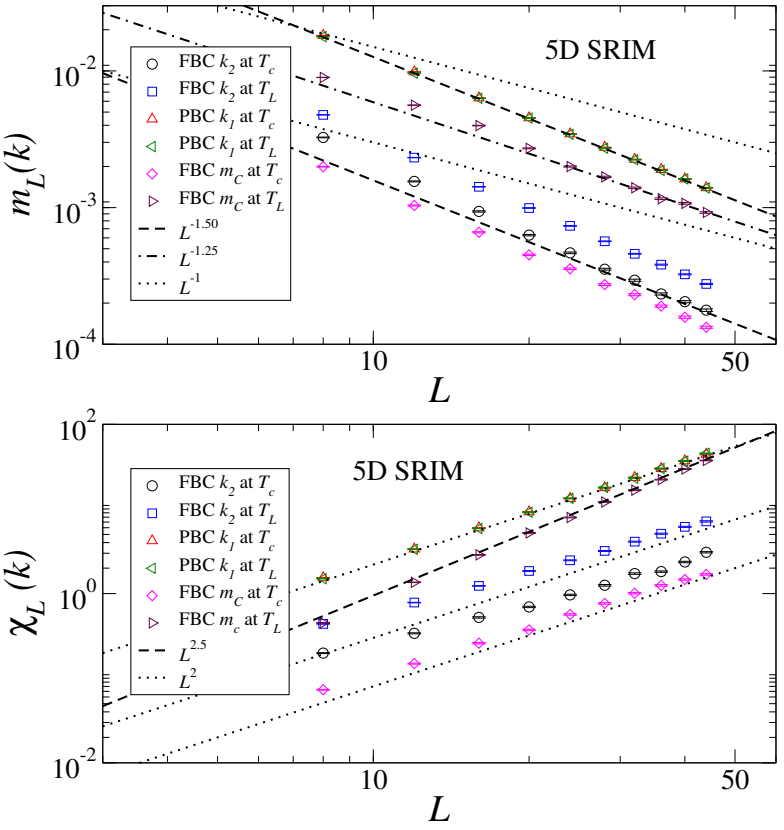

Figure C.17: FSS in the magnetisation sector for non-zero modes for the 3D LRIM with FBCs. In the top image the first magnetisation mode clearly scales as $m_L^\dagger \sim L^{-3/2}$. In the bottom image the first susceptibility mode clearly scales as $\chi_L^\dagger \sim L^2$. Both manifestly in favour of GFSS instead of the standard FSS.

Bibliography

[1] K. G. Wilson. Renormalization Group and Critical Phenomena. I. Renormalization Group and the Kadanoff Scaling Picture. *Phys. Rev. B*, **4**, 3174, (1971).

[2] K. G. Wilson. Renormalization Group and Critical Phenomena. II. Phase-Space Cell analysis of Critical Behaviour, Scaling Picture. *Phys. Rev. B*, **4**, 3184, (1971).

[3] K. G. Wilson and J. B. Kogut. The Renormalization Group and the ϵ Expansion. *Phys. Rep.*, **12**, 75 (1974).

[4] S. K. Ma. *Modern Theory of Critical Phenomena*. West Press, New York, (1976).

[5] E. Brézin. An Investigation of Finite Size Scaling. *J. Physique*, **43**, 15, (1982).

[6] M. E. Fisher. *The Theory of Critical Point Singularities, in Cristal Phenomena, Proceedings of 51st Enrico Fermi Summer School, Varenna, Italy*. M. S. Green, New York, (1971).

[7] M. E. Fisher. Scaling, Universality and Renormalization Group Theory, in Critical Phenomena. *Lecture notes in physics Vol. 186*, page 1, (1983).

[8] K. Binder. Critical Properties and Finite-Size Effects of the Five-Dimensional Ising Model. *Z. Phys. B*, **61**, 13, (1985).

[9] K. Binder. Finite size effects on phase transitions. *Ferroelectrics*, **73**, 43, (1987).

[10] E. Luijten, K. Binder, and H. W. J. Blöte. Finite-size scaling above the upper critical dimension revisited: the case of the five-dimensional Ising model. *The European Physical Journal B - Condensed Matter and Complex Systems*, **9**, 289, (1999).

[11] B. Berche, R. Kenna, and J. C. Walter. Hyperscaling above the Upper Critical Dimension. *Nucl. Phys. B*, **865**, 115, (2012).

[12] C. N. Yang and T. D. Lee. Statistical Theory of Equations of State and Phase Transitions. I. Theory of Condensation. *Phys. Rev. Lett.*, **87**, 404, (1952).

[13] T. D. Lee and C. N. Yang. Statistical Theory of Equations of State and Phase Transitions. II. Lattice Gas and Ising Model. *Phys. Rev. Lett.*, **87**, 410, (1952).

[14] F. Y. Wu. Professor C. N. Yang and statistical mechanics. *International Journal of Modern Physics B*, **22**, 1899, (2008).

[15] M. E. Fisher. *The nature of critical points*. (1965).

[16] M. N. Barber. *Finite-size scaling in phase transition and critical phenomena Vol. 8*. Academic Press, New York, (1983).

[17] B. Widom. Surface Tension and Molecular Correlations near the Critical Point. *The Journal of Chemical Physics*, **43**, 3892, (1965).

[18] M. E. Fisher. Renormalization group theory: Its basis and formulation in statistical physics. *Rev. Mod. Phys.*, **70**, 653, (1998).

[19] M. E. Fisher. Correlation Functions and the Critical Region of Simple Fluids. *Journal of Mathematical Physics*, **5**, 944, (1964).

[20] F. J. Wegner. Corrections to Scaling Laws. *Phys. Rev. B*, **5**, 4529, (1972).

[21] K. Binder, M. Nauenberg, V. Privman, and A. P. Young. Finite Size Tests of Hyperscaling. *Phys. Rev. B*, **31**, 1498, (1985).

[22] E. Brézin and J. Zinn-Justin. Finite Size Effects in Phase Transitions. *Nucl. Phys. B*, **257**, 867, (1985).

[23] E. Luijten and H. W. J. Blöte. Finite-Size Scaling and Universality above the Upper Critical Dimension. *Phys. Rev. Lett.*, **76**, 1557, (1996).

[24] K. Binder and E. Luijten. Monte Carlo Test of Renormalization Group Predictions for Crtitical Phenomena in Ising Models. *Phys. Rep.*, **344**, 179, (2001).

[25] John L Cardy. *Scaling and renormalization in statistical physics*. Cambridge lectrue notes in physics. Cambridge Univ. Press, Cambridge, (1996).

[26] I. G. Brankov, D. M. Danchev, and N. S. Tonchev. Theory of critical phenomena in finite-size systems: scaling and quantum effects. *World Scientific*, (2000).

[27] N. Aktekin and Ş. Erkoş. The test of the finite-size scaling relations for the six-dimensional Ising model on the Creutz cellular automato. *Physica A*, **284**, 206, (2000).

[28] N. Aktekin and Ş. Erkoş. The test of the finite-size scaling relations for the seven-dimensional Ising model on the Creutz cellular automato. *Physica A*, **290**, 123, (2001).

[29] Z. Merdan, D. Atille, G. Mülazimğlu, and A. Günen. The test of the finite-size scaling relations in seven and eight dimensions on the Creutz Cellular Automaton. *Physica A*, **366**, 265, (2006).

[30] J. L. Jones and A. P. Young. Finite-size scaling of the correlation length above the upper critical dimension in the five-dimensional Ising model. *Phys. Rev. B*, **71**, 174438, (2005).

[31] H. Katzgraber, D. Larson, and A. P. Young. Study of the de Almeida˘Thouless Line Using Power-Law Diluted One-Dimensional Ising Spin Glasses. *Phys. Rev. Lett.*, **102**, 177205, (2009).

[32] D. Larson, H. Katzgraber, M. A. Moore, and A. P. Young. Numerical studies of a one-dimensional three-spin spin-glass model with long-range interactions. *Phys. Rev. B*, **81**, 064415, (2010).

[33] F. Beyer, M. Weigel, and M. A. Moore. One-dimensional infinite-component vector spin glass with long-range interactions. *Phys. Rev. B*, **86**, 014431, (2012).

[34] G. A. Baker and G. R. Golner. Spin-Spin Correlations in an Ising Model for Which Scaling is Exact. *Phys. Rev. Lett.*, **31**, 22, (1973).

[35] J. F. Nagle and J. C. Bonner. Numerical studies of the Ising chain with long-range ferromagnetic interactions. *Journal of Physics C: Solid State Physics*, **3**, 352, (1970).

[36] E. Luijten and H. W. J. Blöte. Classical critical behavior of spin models with long-range interactions. *Phys. Rev. B*, **56**, 8945, (1997).

[37] V. Privman. *in Finite Size Scaling and Numerical Simulation of Statistical Systems*. World Scientific, Singapore, (1990).

[38] P. M. Chaikin and T. C. Lubensky. *Principles of Condensed Matter Physics*. Cambridge Univ. Press, Cambridge, (2000).

[39] P. Kopietz, L. Bartosch, and F. Schütz. *Introduction to the Functional Renormalization Group*. Lecture notes. Lecture notes in Physics Vol. 798, Springer-Verlag, Berlin, (2010).

[40] H. Nishimori. *Elements of Phase Transitions and Critical Phenomena.* . Oxford Univ. Press, Oxford, (2011).

[41] R. Kenna and B. Berche. A new Critical Exponent ♀ and its Logarithmic counterpart $\hat{♀}$. *Cond. Matter Phys.*, **16**, 23601, (2013).

[42] R. Kenna and B. Berche. Fisher's Scaling Relation above the Upper Critical dimension. *Europhys. Lett.*, **105**, 26005, (2014).

[43] E. J. Flores-Sola, B. Berche, R. Kenna, and M. Weigel. Finite-Size Scaling above the Upper Critical Dimension in Ising Models with Long-range Interactions. *Eur. Phys. J. B*, **88**, 28, (2015).

[44] E. J. Flores-Sola, B. Berche, R. Kenna, and M. Weigel. Role of Fourier Modes in Finite-Size Scaling above the Upper Critical Dimension. *Phys. Rev. Lett.*, **116**, 115701, (2016).

[45] D. P. Landau and K. Binder. *A Guide to Monte Carlo Simulations in Statisticl Physics*. Cambridge University Press, Cambridge, third edition, (2009).

[46] N. Metropolis, A.W. Rosenbluth, M.N. Rosenbluth, A.H. Teller, and E. Teller. Equations of state calculations by fast computing machines. *Journal of Chemical Physics*, **21**, 1087, (1953).

[47] W. Janke. Statistical Analysis of Simulations: Data Correlations and Error Estimation. *Quantum Simulations of Complex Many-Body Systems: From Theory to Algorithms*, **10**, 423, (2002).

[48] W. Janke. Nonlocal Monte Carlo algorithms for statistical physics applications. *Mathematics and Computers in Simulation (MATCOM)*, **47**, 329, (1998).

[49] M. P. Nightingale and H. W. J. Blöte. Dynamic Exponent of the Two-Dimensional Ising Model and Monte Carlo Computation of the Subdominant Eigenvalue of the Stochastic Matrix. *Phys. Rev. Lett.*, **76**, 4548, (1996).

[50] C. F. Baillie and P. D. Coddington. Comparison of cluster algorithms for two-dimensional Potts models. *Phys. Rev. B*, **43**, 10617, (1991).

[51] P. Tamayo, R. C. Brower, and W. Klein. Single-cluster Monte Carlo dynamics for the Ising model. *Journal of Statistical Physics*, **58**, 1083, (1990).

[52] N. Persky, R. Ben-Av, I. Kanter, and E. Domany. Mean-field behavior of cluster dynamics. *Phys. Rev. E*, **54**, 2351, (1996).

[53] R. H. Swendsen and J. S. Wang. Nonuniversal, critical dynamics in Monte Carlo simulations. *Phys. Rev. Lett.*, **58**, 86, (1987).

[54] U. Wolff. Collective Monte Carlo updating for spin systems. *Phys. Rev. Lett.*, **62**, 361, (1989).

[55] P. W. Kasteleyn and C. M. Fortuin. Phase transitions in lattice systems with random local properties. *J. Phys. Soc. Jpn. Suppl.*, **26**, 11, (1969).

[56] C. M. Fortuin and P. W. Kasteleyn. On the Random-Cluster Model: I. Introduction and Relation to Other Models. *Physica*, **57**, 536, (1972).

[57] J. Hoshen and R. Kopelman. Percolation and cluster distribution. I. Cluster multiple labeling technique and critical concentration algorithm. *Phys. Rev. B*, **14**, 3438, (1976).

[58] E. Luijten. Interaction Range, Universality and the Upper Critical Dimension. *Ph.D. thesis*, (1997).

[59] E. Luijten and H. W. J. Blöte. Monte Carlo method for spin models with long-range interactions. *International Journal of Modern Physics C*, **06**, 359, (1995).

[60] M. C. Angelini, G. Parisi, and F. Ricci-Tersenghi. Relations between short-range and long-range Ising models. *Phys. Rev. E*, **89**, 062120, (2014).

[61] M. Picco. Critical behavior of the Ising model with long range interactions. *arXiv:1207.1018*, (2012).

[62] K. Fukui and S. Todo. Order-N cluster Monte Carlo method for spin systems with long-range interactions. *Journal of Computational Physics*, **228**, 2629, (2009).

[63] D. E. Knuth. *The Art of Computer Programming, Volume 2 (3rd Ed.): Seminumerical Algorithms*. Addison-Wesley Longman Publishing Co., Inc., Boston, MA, USA, (1997).

[64] M. E. J. Newman and R. M. Ziff. Fast Monte Carlo algorithm for site or bond percolation. *Phys. Rev. E*, **64**, 016706, (2001).

[65] J. L. deLyra. The Wolff Algorithm with External Sources and Boundaries. *http://latt.if.usp.br/technical-pages/twawesab/Text.html/*, (2006).

[66] M. Abramowitz and I. A. Stegun. *Handbook of Mathematical Functions: with Formulas, Graphs, and Mathematical Tables*. Dover Publication, 1st edition edition, (1965).

[67] A. M. Ferrenberg and R. H. Swendsen. New Monte Carlo technique for studying phase transitions. *Phys. Rev. Lett.*, **61**, 2635, (1988).

[68] R. B. Griffiths. Dependence of Critical Indices an a Parameter. *Phys. Rev. Lett.*, **24**, 1479, (1970).

[69] M. Wittmann and A. P. Young. Finite-Size Scaling above the Upper Critical Dimension. *Phys. Rev. E*, **90**, 062137, (2014).

[70] M. E. Fisher, S. K. Ma, and B. G. Nickel. Critical Exponents for Long-Range Interactions. *Phys. Rev. Lett.*, **29**, 917, (1972).

[71] J. Sak. Recursion Relations and Fixed Points for Ferromagnets with Long-Range Interactions. *Phys. Rev. B*, **8**, 281, (1973).

[72] J. Honkonen and E. Karjalainen. Diffusion in a random medium with long-range correlations. *Journal of Physics A: Mathematical and General*, **21**, 4217, (1988).

[73] J. Fröhlich and T. Spencer. The phase transition in the one-dimensional Ising model with $1/r^2$ interaction energy. *Comm. Math. Phys.*, **84**, 87, (1982).

[74] T. Blanchard, M. Picco, and M. A. Rajabpour. Influence of long-range interactions on the critical behavior of the Ising model. *Europhys. Lett.*, **101**, 56003, (2013).

[75] E. Brezin, G. Parisi, and F. Ricci-Tersenghi. The Crossover Region Between Long-Range and Short-Range Interactions for the Critical Exponents. *Journal of Statistical Physics*, **157**, 855, (2014).

[76] S. K. Ma. Introduction to the Renormalization Group. *Rev. Mod. Phys.*, **45**, 589, (1973).

[77] G. Parisi and J. J. Ruiz-Lorenzo. Scaling above the upper critical dimension in Ising models. *Phys. Rev. B*, **54**, R3698, (1996).

[78] Z. Merdan and R. Erdem. The finite size scaling study of the specific heat and the Binder parameter for the six-dimensional Ising model. *Phys. Lett. A*, **330**, 403, (2004).

[79] Z. Merdan and M. Bayrih. The effect of the increase of Linear Dimensions on Exponents Obtained by finite-size scaling relations for the six dimensional Ising Model on the Creutz Cellular Automaton. *Appl. Math. Comput.*, **167**, 212, (2005).

[80] M. Suzuki. On the Expansion Theory of Critical Exponents: General Aspects and Some Applications. *Progress of Theoretical Physics*, **50**, 393, (1973).

[81] H. G. Ballesteros, A. Cruz, L. A. Fernández, V. Martín-Mayor, J. Pech, J. J. Ruiz-Lorenzo, A. Tarancón, P. Téllez, C. L. Ullod, and C. Ungil. Critical behavior of the three-dimensional Ising spin glass. *Phys. Rev. B*, **62**, 14237, (2000).

[82] J. Rudnick, G. Gaspari, and V. Privman. Effect of Boundary Conditions on Critical Behaviour of a Finite High-Dimensional Ising Model. *Phys. Rev. B*, **32**, 7594, (1985).

[83] P. G. Watson. *Phase Transitions and Critical Phenomena Vol. 2*. Academic, London, (2011).

[84] P. H. Lundow and K. Markström. Non-vaninshing boundary effects and quasifirst-order phase transitions in high dimensional Ising models . *Nucl. Phys. B*, **845**, 120, (2011).

[85] P. H. Lundow and K. Markström. Finite Size scaling of the 5D Ising model with free boundary conditions. *Nucl. Phys. B*, **889**, 249, (2014).

[86] R. Kenna and B. Berche. *Scaling and Finite-Size Scaling above the Upper Critical Dimension, in 'Order, Disorder, and Criticality: Advanced Problems of Phase Transition Theory' Vol. 4, Yu. Holovatch (Ed.), World Scientific, Singapore*. (2015).

[87] R. Abe. Logarithmic Singularity of Specific Heat near the Transition Point in the Ising Model. *Progress of Theoretical Physics*, **37**, 6, (1967).

[88] C. Domb and D. Gaunt. Equation of state in the critical region. *Journal de Physique Colloques*, **32**, C1, (1971).

[89] M. L. Glasser, V. Privman, and L. S. Schulman. Complex-temperature-plane zeros: Scaling theory and multicritical mean-field models. *Phys. Rev. B*, **35**, 1841, (1987).

[90] C. Itzykson, R. B. Pearson, and J. B. Zuber. Distribution of zeros in Ising and gauge models. *Nucl. Phys. B*, **220**, 415, (1983).

[91] R. Kenna and C. B. Lang. Finite size scaling and the zeroes of the partition function in the ϕ^4 model. *Physics Letters B*, **264**, 396, (1991).

[92] A. Gordillo-Guerrero, R. Kenna, and J. J. Ruiz-Lorenzo. Universal Amplitude Ratios in the Ising Model in Three Dimensions. *J. Stat. Mech.*, P09019, (2011).

[93] W. H. Press, S. A. Teukolsky, W. T. Vetterling, and B. P. Flannery. *Numerical Recipes 3rd Edition: The Art of Scientific Computing*. Cambridge University Press, third edition, (2007).

[94] R. Kenna, D. A. Johnston, and W. Janke. Scaling Relations for Logarithmic Corrections. *Phys. Rev. Lett.*, **96**, 115701, (2006).

[95] R. Kenna, D. A. Johnston, and W. Janke. Self-Consistent Scaling Theory for Logarithmic-Correction Exponents. *Phys. Rev. Lett.*, **97**, 155702, (2006).

[96] R. Kenna. *Universal scaling relations for logarithmic-correction exponents, in 'Order, Disorder, and Criticality: Advanced Problems of Phase Transition Theory' Vol. 3, Yu. Holovatch (Ed.), World Scientific, Singapore*. (2013).

[97] V. Palchykov, C. von Ferber, R. Folk, Yu. Holovatch, and R. Kenna. Critical phenomena on scale-free networks: Logarithmic corrections and scaling functions. *Phys. Rev. E*, **82**, 011145, (2010).

[98] M. Mazars. Ewald methods for inverse power-law interactions in tridimensional and quasi-two dimensional systems. *arXiv:1009.1255*, (2010).

[99] R. B. Paris and D. Kaminski. Asymptotics and Mellin-Barnes Integrals. (2001).